Preparation of Nickel-Gallium based catalysts for carbon dioxide hydrogenation to methanol

Yuhan Men

Submitted in total fulfillment of the requirements of the degree of Doctor of philosophy

August 2020

Department of Chemical Engineering

The University of Melbourne

Abstract

Catalytically converting CO_2 to methanol by hydrogenation offers a method to effectively reduce the excessive CO_2 emission in the atmosphere and produces value-added chemicals simultaneously. Thus, the investigations on catalysts in methanol synthesis reaction has gained attraction in the past few years. Commercial catalysts based on Copper, Zinc, and Zirconium are popular, but increasingly, researchers are looking for other options with superior conversion and selectivity.

From prior literature, catalysts based on Nickel and Gallium, specifically a Ni_5Ga_3 bimetallic catalyst exhibits a similar CO_2 conversion and higher methanol yield compared with commercial Copper-based catalysts. However, the purities of Ni_5Ga_3 catalysts were found to be restricted during the reported synthesis process. Thus, a simpler and reproducible method to prepare highly pure Ni_5Ga_3 is desirable. In this study, we developed a method to synthesize highly pure Ni_5Ga_3 catalyst from hydrotalcite-like compounds (HTlc) precursors for CO_2 hydrogenation to methanol. A series of Ni-Ga HTlc precursor was synthesized in the temperature range between 90 °C and 150 °C. The results indicated the HTlc phase in the nickel-gallium precipitant became better crystallized and the structure became more stable as the synthesis reaction temperature increased. Bimetallic alloy Ni_5Ga_3 was obtained by reducing the as-prepared HTlc precursors in a hydrogen atmosphere. X-ray absorption spectroscopy (XAS) investigation confirmed that a stable and complete HTlc precursor structure assisted in the synthesis of a steady and perfectly structured Ni_5Ga_3 alloy, where the bond distance of Ni-Ga and cell volume increased with temperature. Ni-Ga HTlc precursor prepared at a hydrothermal temperature of 110 °C resulted in the formation of bimetallic alloy, Ni_5Ga_3, which demonstrated characteristics such as smaller crystal size and stable structure under optimized conditions. The enhanced performance was demonstrated by an endurance test with a constant CO_2 conversion and 100% methanol selectivity at 200 °C, and the turnover frequency reached 0.27 s^{-1}.

Metal oxide promoters are well known to enhance catalytic properties, thus, a modification by incorporating promoters, such as Mg, Zn and Zr, was investigated. A new series of Ni-Ga-X HTlc precursors (X represented Mg, Zn and Zr) were

prepared by a similar synthesis procedure, followed by a H_2 reduction process. The results revealed that the main Ni-Ga phase transformed from Ni_5Ga_3 to Ni_3Ga when promoters were incorporated in the Ni-Ga catalytic system, due to an unstable HTlc structure as additional elements were incorporated in the parent precursor. Mg and Zr were present as metal oxides, while $ZnGa_2O_4$ structure was present in Zn-promoted Ni-Ga catalysts. The BET surface area was measured for all prepared Ni-Ga-X catalysts, and the surface area exhibited a sharp increase after the promoter modifications. Among all samples, the Ni-Ga-Zr revealed the highest BET surface area. TEM-mapping measurements, for Ni-Ga-Zr catalyst, showed Ni-Ga assembly as a core, while Zr surrounded the core, which isolated and separated Ni-Ga catalysts. Thus, the average particle sizes of Ni-Ga-Zr catalysts were considerably decreased compared with other samples, resulting in a relatively large surface area. However, the promotion effect was not obvious in other samples, because Mg could not be completely precipitated in the catalysts and $ZnGa_2O_4$ was formed instead. Furthermore, ZrO_2 also facilitated the reduction of Ni-Ga-Zr HTlc precursor due to an enhanced electron transfer.

Additionally, incorporation of promoters generated additional strong basic sites in the catalytic system, as demonstrated by CO_2-TPD measurement. The catalytic properties were evaluated, and a maximum methanol yield (3.8%) was obtained over a Zr-modified Ni_3Ga catalyst at 300 °C, 30 bar, which exhibited a similar reactivity of commercial Cu-based catalysts.

The Ni-Ga-Zr catalysts were subsequently mixed with a commercial high-temperature CO_2 adsorbent (MG50). The Ni-Ga-Zr (NGZr) and MG50 were well-mixed, as revealed from SEM images, and the Ni_3Ga phase did not change when MG50 was introduced in the Ni-Ga-Zr catalytic system. A series of mixed samples, with different ratios of MG50 and NGZr, was prepared. The corresponding CO_2 conversion exhibited a mild decrease as the amount of Ni-Ga-Zr decreased due to loss of active sites, however, the methanol space-time yield was greatly improved as MG50 increased, which suggested that the catalytic property was considerably promoted in the presence of MG50. The highest space-time yield was observed in 25%NGZr/MG50 mixture, with 123.5 $g_{meth} \cdot g_{cat}^{-1} \cdot h^{-1}$ at 300 °C. The promotion was ascribed to enhanced CO_2 adsorption on MG50 adsorbent, resulting in higher CO_2

concentration adjacent to NGZr active sites, contributing to a higher reaction rate and CO_2 conversion.

Despite the great improvement in methanol space-time yield in NGZr/MG50, the overall CO_2 conversion was lower than that of Cu-based catalysts under moderate temperatures, such as 200 °C - 250 °C. Thus, the NGZr catalysts were subsequently modified by optimizing the Zr amount in the NGZr catalytic system. The TEM-mapping revealed that once the ZrO_2 concentration increased above 15%, ZrO_2 experienced a severe agglomeration between the Ni-Ga particles instead of surrounding them. Consequently, the interactions between Ni_3Ga and ZrO_2 was not further increased as Zr content increased from 15% to 25%. The batches of NGZr catalysts were tested for catalytic performance, respectively. The Ni_3Ga catalysts with 15% Zr content exhibited a higher CO_2 conversion under the entire reaction temperature range when compared to Cu-based catalysts, which indicated that the Ni-Ga-Zr (15%) catalyst area promising candidate for future catalytical CO_2 conversion to methanol.

Declaration

This is to certify that:

1) this thesis comprises only my original work towards Ph.D., except the publications indicated in the Preface,

2) the thesis is fewer than 100,000 words in length.

Yuhan Men

August 2020

Preface

Aspects of this thesis have been published elsewhere as follows:

Journal Publications

Men Y, Fang X, Gu Q, et al. Synthesis of Ni_5Ga_3 catalyst by Hydrotalcite-like compound (HTlc) precursors for CO_2 hydrogenation to methanol. ***Appl Catal B Environ***. 2020;275(May):119067.

Acknowledgments

Firstly, to my supervisor, Prof. Paul A. Webley, thank you for your kind support and instruction during my study. I appreciated discussion with you all the time, and I can still remember you persuading me not to give up when I was frustrated and offered ideas and suggestions. I would not have achieved it without your help and support. Thank you for giving me this opportunity to be your student and work in your research group.

To my co-supervisors, Dr. Penny Xiao and Dr. Ranjeet Singh, thank you for all your help and accompany during my study. Thank you, Penny, for all the discussions and paper revising, and thank you, Ranjeet, for all your material testing and methodology discussions.

To Dr. Qinfen Gu, I appreciated discussion with you for experimental setup, synchrotron data measurement and data processing. Thank you so much for giving me a chance to work with you.

Consequently, we acknowledge the use of the Monash centre of electron microscopy (MCEM), Monash X-ray platform (MXP), and XAS, PD beamline (Australian Synchrotron, ANSTO) for providing SEM, PPXRD, and XAS technological support, respectively. We also thank the Materials Characterisation and Fabrication Platform (MCFP) teams in the University of Melbourne, the Victorian Node of the Australian National Fabrication Facility (ANFF), and Melbourne Advanced Microscopy Facility at Bio21. This work was supported by the Australian Research Council (ARC).

Thank you to Leslie Gamel and Michael Zammit in physics technical workshop, for all the discussions and equipment repairing and chatting.

Thank you to Alex Duan, for your XPS support and data processing discussions.

Thank you to the Department of Chemical Engineering and Dr. Kevin Li, for giving me a chance to be a tutor and demonstrator for HM and PED. This allowed me to learn teaching and communication skills and gave me an opportunity to meet many friends.

Thank you to my colleges and friends, Dr. Xin Fang, Dr. Fan Wu, Dr. Frank Wu, Dr. Qinghu Zhao, Dr. Guoping Hu and Dr. David Danaci. I could not finish my study without your help and kindness. I appreciated all the time spending with you and wish you all a bright future.

Thank you to my family, Mum, Dad and Grandma. It is your love that gives me the strength to move on.

I want to thank my husband, Lefu Tao, for his unconditional love and support. I am so lucky to have you in my life, and I would not have the courage to face difficulties and frustration during my study and life without you.

List of Content

Chapter 1 Introduction

Fossil fuels have been widely used for the past few centuries and are still a major contributor to the modern energy system. The massive use of fossil fuels leads to a large amount of CO_2 emissions. CO_2 contributes two-thirds of greenhouse gases and it is predicted that 9.7 Gt CO_2 emission per year is expected by 2050[1]. The increasing amount of CO_2 contributes to global warming and other environmental issues, accordingly, efforts have been made in recent years to control the CO_2 emissions. Several strategies and technologies have been applied in recent years to tackle environmental issues, namely energy efficiency improvement, renewable energy, CO_2 capture and storage, and CO_2 utilisation. However, since fossil fuels remain to be a major resource for energy in the past and foreseeable future, it would be difficult to eliminate CO_2 emission by strategies such as renewable energy and energy efficiency improvement alone. CO_2 is a ubiquitous, cheap, and nontoxic C1 feedstock, thus CO_2 utilization to produce value-added chemicals offers one option to not only tackle the problem of global warming, but also a potential source of renewable energy.

Methanol synthesis from CO_2 reduction, utilization of the captured CO_2 from power plants is industrially feasible and economical. However, CO_2 is a linear molecule, where the central carbon atom is linked to two oxygen atoms with double bonds, contributing to high thermodynamic stability. The splitting of the C=O bond requires high energy, which increases the difficulty in CO_2 utilization. For example, extreme reaction conditions such as elevated pressures and temperatures are required for methanol production. Hence, in the past few decades, the development of a suitable catalyst has been attracting wide interest because it could greatly improve the overall reaction kinetics, and thus enhance the methanol yield.

The aim of this study is to develop and optimize a novel Ni-Ga catalyst for methanol synthesis.

Specifically, the thesis outline is as follows,

-Chapter 2

In the literature review, the catalytic system for methanol synthesis will be briefly introduced, including catalytic preparation methods, active metal sites for methanol synthesis and reaction mechanisms.

-Chapter 3

Discussion and summary of some experimental methodology and materials.

-Chapter 4

A ‘HTlc as precursor’ method was developed, to synthesize highly pure Ni_5Ga_3, and the relationship between parent precursor and reduced catalysts will be discussed accordingly.

-Chapter 5

The precursor was further modified by other additives, such as Mg, Zn and Zr. The catalytic performance was investigated for as-prepared catalysts.

-Chapter 6

The catalyst, with the best catalytic properties in Chapter 5, was subsequently modified by a high-temperature CO_2 adsorbent, followed by investigations of catalytic performance.

-Chapter 7

The optimized recipe for catalysts was studied, by preparing a series of catalysts with different compositions of elements.

-Chapter 8

Conclusions and future work were discussed in this section.

Chapter 2 Literature Review

Catalytically converting CO_2 to valuable fuels or chemical raw materials is highly desirable because CO_2 acts as an almost zero cost feedstock[2]. Traditionally, CO_2 utilization is limited to urea, salicylic acid and polycarbonate synthesis[3]. However, the usage of CO_2 is far from the target goal to reduce CO_2 emissions. Consequently, more CO_2 utilization routes have been investigated during the past few decades, to synthesize products with greater economic value, such as methane, formic acid and methanol.

Hydrogenation is one of the effective ways to convert CO_2 to other valuable chemicals, however, traditional H_2 production mainly depends on fossil fuels, which could produce additional CO_2 emission. Green H_2 production, such as water electrolysis, coupling with CO_2 hydrogenation, contributes to an ideal route for value-added chemical production and CO_2 emission control, simultaneously.

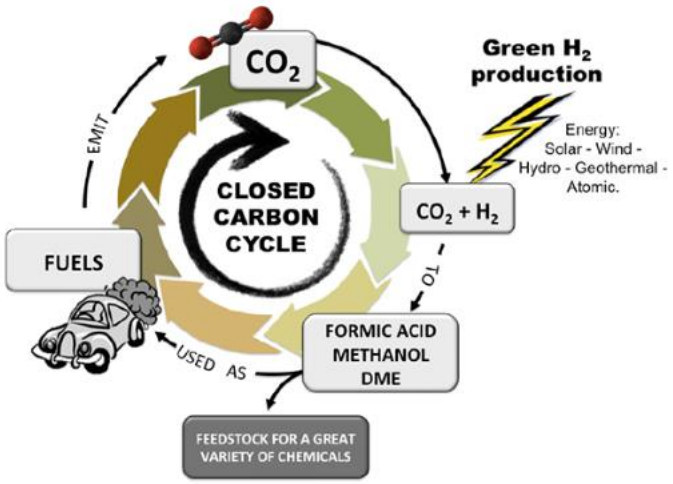

Fig. 1 CO_2 hydrogenation to value-added chemicals[4]

2.1 CO_2 hydrogenation to methane

Methane is the major component of natural gas, and it has been widely used as an alternative fuel for energy plants, replacing traditional fossil fuel to reduce air pollution. CO_2 hydrogenation to produce methane is known as the Sabatier reaction, and can be seen from Equation (1). The hydrogen needed in the reaction could be generated in multiple ways, such as water electrolysis or biomass gasification etc[5], thus, it offers an efficient method to produce methane as a renewable feedstock from the use or renewable H_2.

$$CO_2 + 4H_2 \leftrightarrow CH_4 + 2H_2O \qquad \Delta G = -114\ kJ/mol \tag{1}$$

CO_2 methanation is thermodynamically favourable at low temperatures because it is highly exothermic. However, the kinetics are restricted due to the high stability of CO_2 molecule. Normally catalytic hydrogenation activities will be promoted above 200 °C depending on different catalysts systems and conditions.

Nickel-based catalysts have been widely investigated for CO_2 methanation because of their low cost and high catalytic performance[6]. Additionally, supported nickel catalysts have been widely investigated for methanation of CO_2. Al_2O_3 was one of the most common supports as it has moderate surface area and porous structure. Daroughegi et al.[7] prepared Ni/Al_2O_3 catalysts, and the results showed that the well-separated nickel results in 74% CO_2 conversion and 99% CH_4 selectivity at 350 °C. The enhanced activity from the strong metal-support interaction (SMSI) between nickel and alumina inspired the investigations for other metal oxides as supports. Muroyama et al.[8] investigated CO_2 methanation via nickel supported on different metal oxide carriers, such as La_2O_3, ZrO_2, CeO_2, Sm_2O_3, Y_2O_3. The results revealed that Y_2O_3 significantly promoted the reaction activity, with the highest CH_4 yield of 80% at 300 °C. The promotion effect was ascribed to the moderate basic sites in Y_2O_3. To increase the surface area of the carrier, Rahmani et al[9] synthesized mesoporous Al_2O_3 as support, and roughly 80% CO_2 conversion was achieved at 350 °C.

Apart from nickel-based catalysts, noble metals, such as palladium and cobalt, presented a higher reaction activity and methane purity. CO_2 methanation over mesoporous Co/SiO_2 was studied for the effect of different calcination temperature, and the result revealed that the precursor, calcinated at 100 °C exhibited the highest CO_2 reaction rate, up to 3.29 x 10^{-5} mol/g_{cat}/s at 360 °C[10]. Zhou et al. investigated the effect of mesoporous silica structure (KIT-6) as support on CO_2 methanation performance. The high dispersion of Co on KIT-6 exhibited a CO_2 conversion of 48.9% and 100% methane selectivity at 280 °C. The enhanced catalytic activity could be attributed to the highly ordered mesoporous structure and large surface area[11].

Over the past decades, considerable efforts were devoted to study the mechanism for CO_2 methanation. However, the reaction pathways are still in debate. Presently

there were two major agreed pathways: (1) CO as intermediate, followed by CO hydrogenation and (2) direct CO_2 hydrogenation to methane without CO as intermediate[12,6]. For example, CO was detected as the intermediate in Ru catalyzed CO_2 methanation, and the reaction pathway, investigated by DRIFT revealed that CO was produced from Reverse Water-Gas Shift (rWGS), and then was further hydrogenated to methane[13]. Similar results were observed with Ni/Al_2O_3 catalysts[8]. However, a different mechanism was reported by Pan et al.[14]; where, Formate was detected as an important intermediate by in-situ FTIR, instead of CO, in $Ni/Ce_{0.5}Zr_{0.5}O_2$ catalyst system, and similar intermediate was also reported in Ni/Y_2O_3[8] catalyst system.

2.2 CO_2 hydrogenation to formic acid

Formic acid is an essential raw material for various applications, such as the agriculture and textile industry. Formic acid synthesis from gaseous CO_2 and H_2 is not thermodynamically favourable, as can be seen from Equation (2),

$$CO_{2(g)} + H_{2(g)} \rightarrow CH_3O_{(l)} \quad \Delta G°=32.9 \text{ kJ/mol} \quad \Delta H°=-31.2 \text{ kJ/mol} \qquad (2)$$

However, the participation of solvent in this system could promote the forward reaction because it slightly decreases the Gibbs free energy in aqueous phase[4], as can be seen from Equation (3),

$$CO_{2(aq)} + H_{2(aq)} \rightarrow HCOOH_{(aq)} \qquad \Delta G°=-4 \text{ kJ/mol} \qquad (3)$$

Water was once considered as a solvent, but high CO_2 and H_2 pressures were necessary to drive the equilibrium. Bases were further proposed as a favourable solvent to increase the proton transfer, and thus help drive the reaction and increase the formic acid yield[15]. The mechanism of Lewis base coupling with H_2 on the gold surface was investigated by Lv et al.[16]. The dissociated hydrogen atom from H_2 and proton from NH_3 transferred to CO_2, followed by the formation of concerted hydride, as an important intermediate in the synthesis of formic acid. In this process, NH_3 enhanced the electron donation to the Au surface, and thus promotes the overall reaction. Normally, high-boiling nitrogenous bases were used in formic acid synthesis. Basic solvent increased the formic acid production, however, the separation of base and catalysts limited the application[15].

Homogenous catalysts have attracted widespread attention in the past few decades. The homogenous catalysis offered many actives and higher catalytic activity. Cationic rhodium hydride complexes $(Rh(NBD)(PMe_2Ph)_3)BF_4$ was first investigated for the mechanism for homogenous CO_2 hydrogenation to formic acid. The result revealed that the intermediate $H_2Rh(PMe_2Ph)_3(S)$ were active sites for CO_2 reduction to formic acid[17]. Despite numerous advantages in the homogenous catalytic system, catalytic deactivation was one of the major setbacks in its application. To study the preparation method and catalyst stability, bidentate phosphine ligand, 1.2-bis-(diphenylphosphino) ethane(dppe), was reported to assemble stable $RuCl_2(dppe)_2$ catalyst for CO_2 reduction to formic acid via immobilization method. Immobilization of the Ru-phosphine complex on silica support with covalently linked ligands for the synthesis of homogenous Ru catalyst, resulted in high stability and high activity, compared with simple impregnation method[18]. To further improve the reaction rate and formic acid yield, supercritical CO_2 ($scCO_2$) was considered. Jessop et al.[19] reported a highly promoted formic acid synthesis in $scCO_2$, with 4000 h^{-1} at 50 °C via $RuH_2[P(CH_3)]_4$ or $RuCl_2[P(CH_3)_3]_4$ catalytic system. The prompt H_2 diffusion, increased interaction between $scCO_2$ and H_2 and a strong stability of catalyst contributed to the enhanced catalytic performance.

2.3 CO_2 hydrogenation to methanol

Methanol is an important chemical for many facets of industry. It can be an alternative fuel for combustion engines, and it is also a common starting material for the synthesis of higher hydrocarbons. Methanol synthesis from CO_2 involves three parallel reactions, namely methanol synthesis reaction (4), Reverse Water-Gas Shift (rWGS) reaction (5) and CO_2 methanation (6)[20].

$$CO_2 + 3H_2 \rightarrow CH_3OH + H_2O \qquad \Delta H_{298K}\text{=-49.5 kJ/mol} \qquad (4)$$

$$CO_2 + H_2 \rightarrow CO + H_2O \qquad \Delta H_{298K}\text{=41.2 kJ/mol} \qquad (5)$$

$$CO_2 + 4H_2 \rightleftharpoons CH_4 + 2H_2O \qquad \Delta H_{298K}\text{=-165.0 kJ/mol} \qquad (6)$$

To achieve a high methanol yield, working closer to equilibrium would be the ideal. As a result, high pressures are necessary to drive the forward reaction and achieve high CO_2 conversion as per Le Chatelier principle, and low temperatures were also

advantageous due to the exothermic nature of the reaction. However, low temperatures results in a decrease in the reaction rate. In general, elevated temperature and pressures favoured methanol synthesis, and these reaction conditions also hinder the formation of CO generated from the rWGS reaction.

2.3.1 Non-supported/nano-metal catalysts

2.3.1.1 Cu-based catalysts

Cu-based catalysts have been investigated for the past few decades. The Imperial Chemical Industries first developed a ternary Cu-ZnO-Al_2O_3 for CO_2 direct reduction to methanol from natural gas as feedstock[4]. Based on its overwhelming catalytic performance, the researchers shifted their attention to the study of Cu-ZnO based catalytic system. One of the most exciting results indicated that the methanol yield was proportional to the metallic copper surface area in the general copper-based catalyst system[21]. Hence, a desire to develop a Cu-catalyst with better copper dispersion and higher surface area to enhance the overall methanol yield gained importance. A number of different synthetic methods, each with various impacts on the catalytic performance have been reported. **In the first section of this review**, **different preparation methods** for catalyst synthesis will be discussed.

The conventional co-precipitation method was the most commonly used for the preparation of Cu-based catalysts. A constant pH during the co-precipitation process would create a mild nucleation environment to prevent agglomeration of catalyst particles. Different components, such as copper and zinc, can be precipitated simultaneously, which could contribute to a better interaction between chemical species. Arakawa et al.[21] prepared a series of Cu-ZnO-metal oxide catalysts via a constant pH co-precipitation. Maximum methanol yield was achieved at 250 °C, whereas there was an obvious decrease over 250 °C due to thermodynamic limitations. In the co-precipitation method, removal of alkali-metal impurities was difficult by washing steps. Jun et al. further investigated the residual sodium effect on catalytic performance. Precipitated Cu-ZnO-Al_2O_3 were washed with different amounts of water to obtain a series of content of sodium cations on the surface. A sharp decrease in reaction rate was observed due to residual sodium

which was found to be detrimental to Cu, ZnO and Al_2O_3 interactions, resulting in a poor Cu dispersion[22].

Oxalate route was another precipitation technique in the coprecipitation method. Instead of changing pH in solution by addition of alkaline solution, oxalate formed complexes with ions in the precursor, such as CuC_2O_4 and ZnC_2O_4. The obtained precipitates were calcinated and reduced before use. This method did not introduce additional metal ions from the precipitant thus reducing the risk of metal alkaline residue on the catalyst surface. Ma et al. reported that the water content in metal oxalate precipitants should be controlled in the range of $0 \leq x \leq 1$ with a formula of $Cu/ZnC_2O_4.xH_2O$ to form a significantly less-ordered structure. The disorder contributed to a well-separated Cu and Zn, thus enhancing the metal-support interactions to promote the catalytic activity[23]. A further investigation under the gel-oxalate coprecipitation method suggested that the morphologies, including surface area, pore volume and particle size were promoted by using a mild calcination step[24].

The solid-state route developed a faster way to prepare catalysts. Specifically, hydrated metal salts and citric acid ligands were directly mixed, followed by physically mixing followed by calcination. In this process, the metal salts behaved as oxidants, while organic materials were used as fuels. This rather simple and solvent-free approach has attracted wide interest. Guo et al.[25] prepared Cu-ZnO-ZrO_2 (CZZ) catalysts via the solid-state method and high dispersion of Cu was achieved, and CZZ calcinated at 400 °C exhibited the highest catalytic activity with the largest copper surface area. However, Zhuang et al[26] compared different synthesis methods for the preparation of Cu/ZrO_2, namely fractional precipitation (FP), impregnation-precipitation (IP) and solid-state reaction (SR). Cu/ZrO_2 prepared from IP method showed the best performance with higher CuO dispersion and stronger interaction between metal and support, while SR exhibited the worst copper dispersion. In his work, NaOH was used for combustion instead of citric acid. These reverse results raised interest in investigations for fuels in the solid-state reaction process. Lei et al.[27] compared the influence of citric acid, oxalic acid and urea on the catalytic properties. The result suggested that citric acid was more appropriate for SR method of catalyst preparation, as it resulted in catalyst with smaller particle sizes; whereas, severe agglomeration was observed when oxalic

acid and urea were used. More investigations were conducted on fuels in SR using glycine as complexing agent as it is known to react non-violently with metal nitrates. Guo et al. reported that the chemical properties were greatly influenced by the amount of glycine. A moderate amount of glycine (50% stoichiometric amount) resulted in the highest methanol yield with large BET surface area and high dispersion of copper, whereas a detrimental effect was observed with the increasing glycine amount. In this case, glycine as fuel generates combustion heat, while fuel-rich reaction would generate a great amount of heat and gas with a long reaction time resulting in further agglomeration of copper[28].

Hydrotalcite-like compounds (HTlc) / Layered-double Hydroxide (LDH) as precursors to prepare catalysts have been widely used in copper-based catalysts. HTlc can be described with a formula of $[M_{1-x}^{2+}M_x^{3+}(OH)_2]A_{x/n}^{n-}.mH_2O$, where M^{2+} and M^{3+} represent divalent and trivalent cations, respectively, and include Mg^{2+}, Ni^{2+}, Cu^{2+}, Co^{2+} or Mn^{2+} and Al^{3+}, Cr^{3+} or Ga^{3+}. A pure phase HTlc could be obtained when the x value varies between 0.20 to 0.33. The cations are wrapped in a hydroxide octahedral framework, consisting of a positively charged layer structure. A^{n-} represents the anions stored in the gallery, which could neutralize the extra charge brought from the cations in layers.

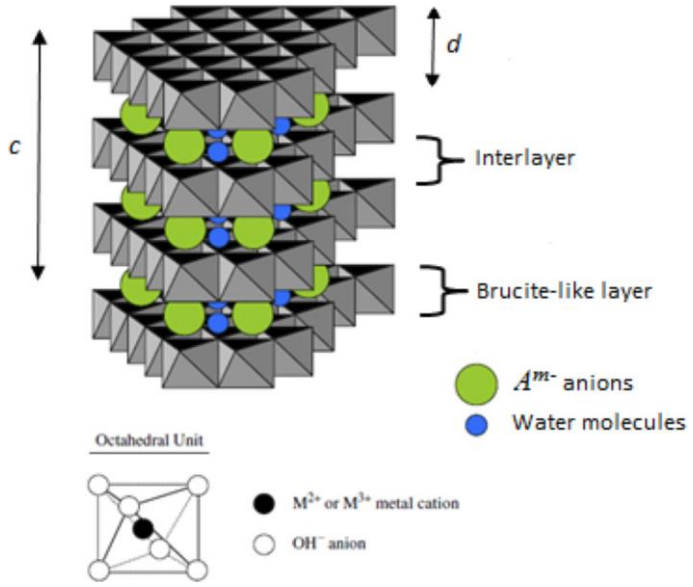

Fig. 2 The structure of hydrotalcite-like compounds (HTlc)/ Layered-double hydroxide (LDH)

The precursors can be typically synthesized by hydrothermal reaction and co-precipitation. Traditionally, sodium carbonate or other alkaline solution was mixed with metal nitrates with vigorous stirring. The solution was aged several hours under

high temperature or transferred to a Teflon-lined autoclave for hydrothermal reactions. The obtained precursors were calcinated to produce mixed metal oxides and further reduced under H_2 prior to use. The as-prepared samples possessed a high copper metallic surface area due to homogenous atomic dispersion and revealed a strong resistance to sintering. A typical Cu-ZnO-Al_2O_3 catalyst was firstly synthesized by HTlc precursor, the as-prepared sample exhibited a homogenous Cu dispersion with an average particle diameter of 10-20 nm. However, a $ZnAl_2O_4$ spinel structure was formed with a Zn:Al ratio of to 2 was used over 600 °C. The copper embedded into the spinel matrix, contributed to a lower metallic copper surface area. At elevated synthesis temperature and other Zn:Al ratio, on the other hand, an amorphous carbonate-modified ZnO-Al_2O_3 form was synthesized at the same time and copper was well segregated by the mixed metal oxides[29]. Based on this typical Cu-Zn-Al HTlc synthesis, Gao et al.[30] further partially replaced Al^{3+} with Zr^{4+}, and the HTlc yield reduced with the increasing amount of Zr in the precursor, due to a large distortion brought from Zr^{4+}. Other than elemental replacement, the pH during HTlc synthesis also played an important role. Xiao et al.[31] reported a pure phase HTlc could be prepared under the high pH over 9.0, and the resulting catalysts exhibited a higher catalytic performance.

Metal-organic framework (MOF) is a highly ordered porous material, with high surface area. The various chemical variations of the organic composition greatly enhance its high catalytic performance[32]. MOF has not been investigated as a catalyst for CO_2 reduction to methanol until recent years. Rungtaweevoranit et al.[33] reported a Cu nanocrystal catalyst, encapsulated in the Zr-based MOF structure. Specifically, copper was embedded in nanosized Zirconium oxide secondary building units that were built with a formula of $Zr_6O_4(OH)_4(BDC)_6$, BDC=1,4-benzene dicarboxylate. The catalysis performance was tested, and an overwhelming methanol TOF was observed at 175 °C, which was 8 times higher than commercial Cu-ZnO-Al_2O_3. The greatly enhanced performance was suggested by a large surface area, strong interactions with Zr oxide and Cu nanoparticles. Also, the metal oxide building units facilitated the interaction between reactants and embedded copper, and removal of generated water and methanol.

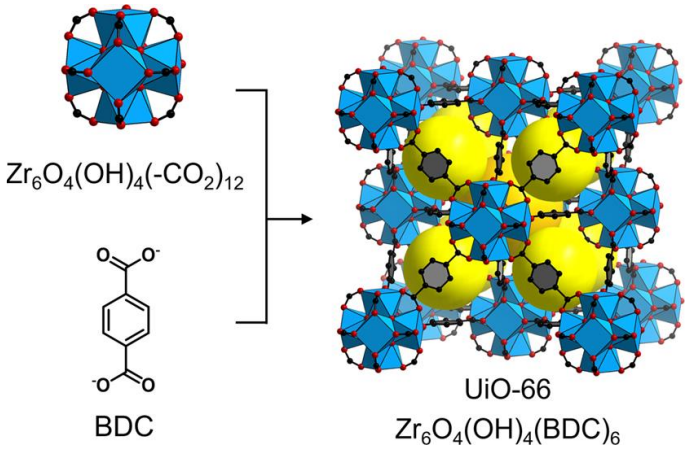

Fig. 3 Crystal Structure of UiO-66 Where Zr Oxide SBUs Are Linked with BDC To Form an Ordered Array of the SBUs, where C, black; O, red; Zr, blue polyhedra. H atoms are omitted for clarity. Yellow spheres represent the space in the framework[33].

MOF and HTlc are known as important templates for the preparation of porous materials, as a result, Zhao et al.[34] integrated HTlc and MOF to synthesize hierarchical sheet-like Cu-Zn-Al catalyst. The integrated catalyst revealed a high methanol selectivity (>90% at 200 °C) [34]. Overall, the MOF derived catalyst revealed significantly high reactivity, however, the thermal instability at high temperature limited its applications.

Copper-based catalysts are major components in the catalytic system and have been investigated for the past few decades. The studies suggested that superior catalytic performance was ascribed to the synergy effect between copper and other metal oxides. Among all the copper-based catalysts, ZnO accounted for a major component and was one of the compositions of industrial methanol synthesis catalyst. Other metal oxides, such as ZrO_2 and CeO_2, were also investigated by researchers.

In the second section, the interactions between copper and different metal oxides are compared and summarized.

1) Zinc Oxide (ZnO)

Industrial methanol synthesis consists of $Cu/ZnO/Al_2O_3$, with roughly 50-70%CuO and 20-30%ZnO[35]. Compared with Cu, ZnO is an inert component, and it alone does not show any reactivity. However, the CO_2 conversion showed a significant improvement with the introduction of ZnO into the Cu catalyst. Given that CO_2

conversion was related to the metallic copper surface area, researchers first ascribe this superior activity to a better copper dispersion in the Cu-ZnO matrix. Generally, CuO was geometrically separated by ZnO, contributing a smaller metallic copper particle size. As a result, ZnO was known as “spacer” or “stabilizer” because it diluted the active component and also hindered the sintering process[36,37]. Moreover, the intrinsic activity was also affected by other contributions. ZnO is known as a semiconductor, and the characterization facilitates the electron transfer. The XPS measurement results reported by Liao et al.[38] indicated the polar (002) face in plate-like ZnO appears to have a strong electronic transfer to Cu nanoparticles. Specifically, spilled hydrogen atoms from the Cu surface would transfer to ZnO and react with CO_2 activated on the ZnO surface. Subsequently, the electron transfer was confirmed by Operando Synchrotron PXRD and modulated-excitation infrared spectroscopy; and an elongated ZnO was preferred to enhance methanol synthesis as well as rWGS[39].

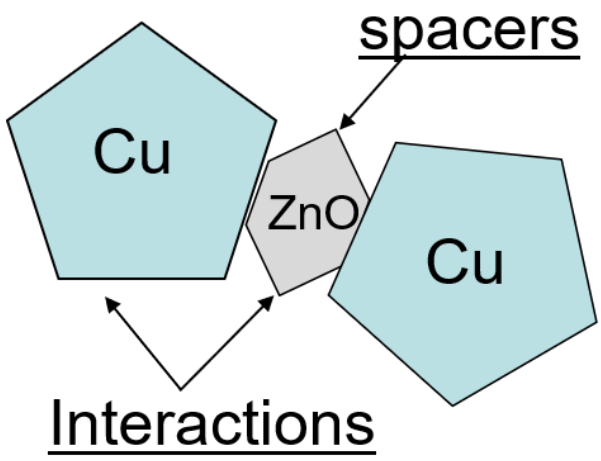

Fig. 4 Schemes of Cu-ZnO catalytic system

Significant efforts have been made to understand the nature of active sites in the Cu-ZnO system, however, it remains debatable in recent studies. Some argued Cu was the active site whereas ZnO acts as a H_2 reservoir, electronic promoter, and physical structure stabilizer, as described above. Other researchers suggest that ZnO is partially reduced and a CuZn alloy is synthesized, which promoted methanol synthesis. Behrens et al.[40] reported Zn was partially alloyed at Cu in the step. To compare the intrinsic activity via CuZn alloy with Cu-ZnO hybrid catalyst, density functional theory (DFT) calculations were conducted on Cu(111), Cu(211) and

CuZn(211) faces. The result revealed that the lowest energy barrier reaction pathway was observed on CuZn(211) face. Moreover, the intermediates were stabilized on the surface of CuZn(211), contributing to a higher reactivity for methanol synthesis. However, Grunwaldt et al. reported that the surface CuZn alloy was observed under strong reducing conditions (e.g. over 300 °C), and the formation of the alloy was reversible and was not permanently present in the Cu-ZnO system[41]. Similar results were reported by Kattel et al.[42] suggesting that Zn in CuZn alloy eventually transformed back into ZnO under normal methanol synthesis reaction conditions. The oxidation was due to the accumulation of *O species derived from CO_2 dissociation on CuZn(211) face. The result also pointed out that a steady methanol production was generated on the interface from Cu/ZnO. Based on the results, Kuld et al. reported methanol synthesis activity exhibited a strong interdependency with Zn coverage on Cu surface, supported by DFT calculations[43]. A further investigation suggested that catalytic performance on ZnO/Cu (100) exceeded that on ZnO/Cu(111), and also observed that ZnCu alloy was unstable during optimized reaction conditions[44].

2) Zirconium (ZrO_2)

ZrO_2 is one of the most widely used additives in Cu-based catalysts. ZrO_2 is known as a transition metal oxide, with moderate alkalinity and oxygen vacancy. The ZrO_2 modified catalysts exhibit a greatly improved CO_2 conversion and methanol selectivity, and thus efforts have been devoted to understanding the ZrO_2-doped catalytic system. Identically, to the function of ZnO, ZrO_2 could adsorb and activate CO_2, and accept the dissociated hydrogen atom from Cu. Zhuang et al.[26] considered that fact that ZrO_2 was a p-semiconductor, and suggested that the strong interactions between Cu and ZrO_2 possibly turns copper into an electron-deficient state. This state could improve H_2 and CO_2 adsorption capacity, which would promote methanol production. Consequently, ZrO_2 was also known as a “hydrogen reservoir”, and the H_2 donation from Cu was denoted as “hydrogen spillover” effect. Evidence was provided to prove the strong interactions between Cu and ZrO_2. Schilke et al.[45] reported an in-situ infrared measurement on Cu-Zr-Ti type catalyst. A bidentate carbonate intermediate was observed both on Cu and ZrO_2 surfaces, and methanol production was enhanced with an increasing amount of ZrO_2, far surpassing the performance via individual Cu or ZrO_2. The interaction

was also found to help separate the active component, resulting in a smaller Cu particle size and higher dispersion. Barbera et al.[46] reported an increasing BET surface area with the introduction of ZrO_2 and a lower reduction temperature due to smaller CuO particles.

ZrO_2 has different polymorphs, including monoclinic phase (m-ZrO_2), cubic phase (c-ZrO_2), and tetragonal (t-ZrO_2). It was reported that t-ZrO_2 transformed to m-ZrO_2 as the temperature increased[47], and the phase changes can affect the physical properties accordingly. Guo et al.[25] prepared Cu/ZnO/ZrO_2 (CZZ) under different calcination temperatures, and the transformation was observed over 600 °C. The result revealed that the CO_2 conversion was higher via t-ZrO_2 as support due to a higher metallic Cu dispersion. However, it was observed in CO hydrogenation to methanol by Rhodes et al. [48], that the reactivity of Cu/m-ZrO_2 was 10 times higher than Cu/t-ZrO_2. In their study, CO adsorption capacity was enhanced because of the presence of anionic vacancies on the surface of m-ZrO_2, which resulted in the exposure of Zr^{4+}. The presence of Zr cations enhanced the Bronsted acidity, contributing to CO adsorption as starting intermediate for methanol synthesis[49].

3) Additional metal oxides (CeO_2/Ga_2O_3/TiO_2)

CeO_2 as promoters in Cu-based catalysts systems are reported to have an obvious enhancement in methanol synthesis due to its high redox ability. Bonura et al. found the H_2 spillover effect was facilitated across the ceria lattice, contributing to a promoted methanol synthesis rate[50]. Senanayake et al.[51] compared the apparent activation energy for methanol synthesis reaction on Cu (111), ZnO/Cu(111) and CeO_x/Cu(111) plane, and the result revealed that cerium oxide decorated copper catalysts exhibited the lowest activation energy, leading to a conclusion that the interface of Ce and Cu played a vital role in methanol synthesis. A highly active Cu-Ce catalyst was reported to exhibit 14 times faster rate than Cu/ZnO by Graciani et al[52]. The Ce/Cu interface activated CO_2, and the abundant oxygen vacancies on the CeO_x surface promoted the reactivity. The morphologies of CeO_2 were also found to have an influence on methanol synthesis. Ouyang et al. prepared three types of CeO_2 with different nanostructures, namely nanorod, nanotubes and nanoparticles[53]. The result suggested that nanorod-type CeO_2 exhibited the highest

performance due to a strong interaction between copper and the exposure of plane (100) and (110) of CeO_2.

Fujitani et al.[54] first reported the introduction of Ga_2O_3 in the Cu-ZnO system. It was suggested that Cu/ZnO combined with Ga_2O_3 provided a higher copper surface area, which contributes to activity of the catalyst. Similar results were observed in the Cu-Ga_2O_3-ZrO_2 ternary system[55]. A careful control of Cu-Ga-Zr content resulted in well-dispersed Cu active sites, and thus maximized the metallic copper surface area. Regarding the Ga_2O_3 surface functionality during the methanol synthesis reaction, an in-situ FTIR study was conducted[56]. When Cu-Ga_2O_3 was treated with CO_2, a polydentate carbonate was detected on the Ga_2O_3 surface, which could be retained even at 450 °C. The polydentate carbonate was an intermediate when CO_2 was adsorbed to Ga_2O_3 surface, and the presence of polydentate carbonate indicated the ability of CO_2 adsorption. Thus, it was also revealed that Ga provided uniform and weak surface basicity which facilitated methanol synthesis.

TiO_2 has been widely applied in CO_2 hydrogenation to produce methanol because of its excellent electron transfer properties, low cost and high stability[57]. Nomura et al.[58] decorated Cu-ZnO with TiO_2 and found that Cu:Zn:Ti ratio of 3:3:4 was optimal; while Xiao et al.[59] came up with a different optimum ratio with only 10% TiO_2 loading in the Cu-ZnO system. Summarily, the introduction of TiO_2 enhanced Cu dispersion, and the preferred TiO_2 loading content was observed with the highest metallic copper surface area. Other than surface area, the addition of TiO_2 increased the number of basic sites, promoting the CO_2 adsorption on its surface, and thus facilitate overall methanol production[60]. Furthermore, to prove the CO_2 adsorption on TiO_2 surface, intermediates were detected by an in-situ FTIR measurement[61]. The result indicated Cu could only scarcely adsorb CO_2, while TiO_2 established a weak bonding with CO_2 and the adsorbed CO_2 species promptly converted to a formate species.

Generally, Cu-based catalysts were widely used in industry for its high stability, low cost and reasonable methanol production. However, the non-negligible CO generated from rWGS, even modified by metal oxides, increased the difficulty in product separation and thus limited its application.

2.3.1.2 Noble metals

1) Palladium (Pd)

Pd is one of the noble metals, and the derived Pd-based catalysts exhibit high stability and activity in methanol synthesis. Similar to Cu-based catalysts, the catalytic performance is greatly promoted by metal oxides. Ga_2O_3 modified Pd catalysts were investigated by Collins et al.[62], and the hydrogen spillover effect from Pd metal via SiO_2 to Ga_2O_3 was observed by in-situ FTIR. Furthermore, the shape of Ga_2O_3 was found to influence CO_2 conversion and methanol selectivity. Specifically, Ga_2O_3 nanorod and nanoplate were synthesized separately, and plate-like Ga_2O_3 revealed a higher CO_2 conversion and methanol selectivity (17.33% and 51.62%, respectively). The promoted reactivity was due to an enhanced electron transfer between the (002) plane on Ga_2O_3 and Pd surface because of a strong SMSI[63]. A ternary Pd-Zn-Al was investigated, and the best result was observed in Pd-ZnO with 3.93 wt% Al content. ZnO exhibited a similar CO_2 activation and adsorption with Cu-based catalysts, and the decoration with Al, further enhanced its adsorption ability. However, a $ZnAl_2O_4$ spinel structure was formed with an excess amount of Al, which in contrast hinders methanol production[64]. A significantly enhanced Pd-ZnO catalyst, with a 200% increase of CO_2 conversion, was reported by Wu et al.[65] under a novel light irradiation modified fixed bed reactor. It was suggested that a localized surface plasmon resonance contributed to the promoted reactivity. In addition, In_2O_3 modified Pd catalysts were also found to be highly active for methanol synthesis, with over 20% CO_2 conversion and 70% methanol selectivity. Rui and co-workers prepared Pd-In_2O_3 hybrid catalyst via a thermal treatment method[66]. Highly dispersed Pd on In_2O_3 exposed highly active (111) plane, which could adsorb and dissociate H_2 into atomic H, followed by a hydrogen transfer to In_2O_3. The creation of oxygen vacancy by hydrogen transfer significantly promoted methanol production. The results also indicated that Pd-In_2O_3 interface, rather than Pd-In bimetallic surface, was highly active for methanol synthesis.

2) Gold (Au)

Gold is a precious metal and has been widely used in catalysis. Even though bulk Au is catalytical inactive, the metal oxides modified with Au have been observed to be highly active for methanol formation from CO_2. Different metal oxides, including

ZrO_2, ZnO, CeO_2 and TiO_2 decorated Au catalysts were investigated by Wu et al[67]. A fine Au particle size was obtained (1.6 nm) on Au/ZrO_2, and a strong interaction between Au and ZrO_2 contributed to an outstanding TOF (around 20 h^{-1}). The functionality of CeO_x/TiO_2 was further investigated by Yang et al.[68] Au nanoclusters were well-separated on CeO_x and TiO_2, and CO_2 was greatly activated by an electronic polarization near the Au-CeO_x/TiO_2 interface. DFT calculations further revealed that Ce-Ti mixed oxides can decrease the energy barrier of the methanol synthesis reaction, leading to a low-pressure CO_2 hydrogenation with high methanol selectivity.

2.3.1.3 Bimetallic catalysts

Bimetallic catalysts have a strong synergistic effect on promoting the methanol synthesis reaction, consequently, more investigations were carried out to understand the chemistry on a bimetallic interface for methanol formation.

The Ni-Ga catalytic system was first reported by Studt et al[69]. The DFT calculations indicated that the intrinsic activity for CO_2 reduction over Ni_3Ga and Ni_5Ga_3 was close to that of conventional Cu-based catalysts, as can be seen from Fig. 5.

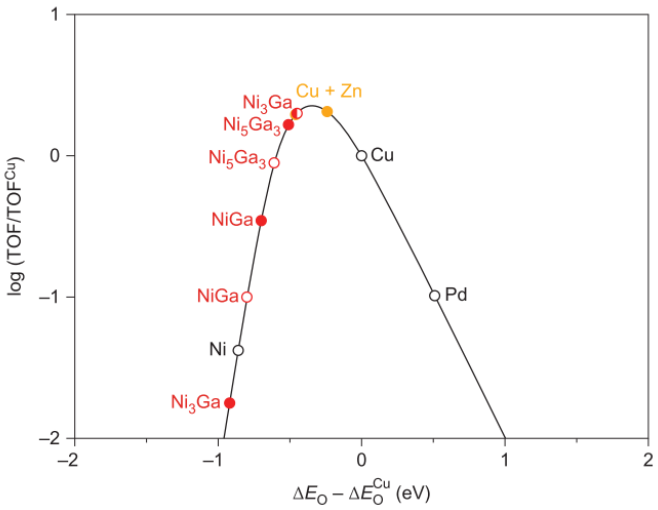

Fig. 5 Theoretical activity volcano for CO2 hydrogenation to methanol[69]

To test the activity on different Ni-Ga catalysts, the methanol synthesis reaction was compared over a series of SiO_2 supported Ni-Ga bimetallic catalysts, namely

$NiGa/SiO_2$, Ni_3Ga/SiO_2 and Ni_5Ga_3/SiO_2. The result indicated that Ni_5Ga_3 was highly active and selective to methanol synthesis, while Ni_3Ga exhibited a low methanol selectivity, with most of the CO_2 converted to methane. Compared with Cu-based catalysts, Ni_5Ga_3 revealed a comparable methanol formation activity under ambient pressure. The active site in Ni_5Ga_3 was investigated, and it was reported that Ni-rich Ni_5Ga_3 active site was poisoned by CO (by-product) during the reaction. Thus, the methanol synthesis was in turn promoted and a high methanol selectivity was observed. Based on this result, Gallo et al.[70] found the fact that an amorphous Ga_2O_3 shell was formed around Ni_5Ga_3 nanoparticles when the fresh catalyst was exposed to air, and the shell could only be reduced over 600 °C. Interestingly, however, the amorphous Ga_2O_3 shell was found to facilitate the methanol synthesis. Later, Ahmad and co-workers[71] attempted to understand the impact of different catalyst preparation methods on the overall catalytic performance. The highest methanol formation rate was observed over a Ni-Ga catalyst prepared from an incipient wetness impregnation method (IWI), while Ni_5Ga_3 via co-condensation-evaporation method (CE) revealed a rather poor reactivity. The promoted activity was attributed to a high surface area and better metal dispersion with smaller particle sizes. In addition, it was worth mentioning that Ni_5Ga_3 purity was also affected by different methods. Although, impurities (Ni_3Ga) were observed in all three methods, no obvious Ni_5Ga_3 phase was detected via samples prepared from CE method, which possibly resulted in a poor catalytic property. The SiO_2 supported Ni_5Ga_3 was further modified by a micro fibrous-structured $Ni_5Ga_3/SiO_2/Al_2O_3$/Al-fibre. This new support provided a crucial outcome for reducing Ni_5Ga_3 nanoparticle sizes, and it could stabilize bimetallic catalytic with a longer lifetime (over 75 hours)[72]. Promoters, such as Au, Co, and Cu were introduced in the Ni-Ga system, and the highest TOF for CO_2 hydrogenation was observed in the Au-Ni-Ga catalyst, almost 4-times higher than Ni_5Ga_3[73] alone. Unlike the previous study, Au-Ni-Ga exhibited a typical Ni_5Ga_3 XRD pattern, whereas Cu-Ni-Ga and Co-Ni-Ga showed the formation of Ni_3Ga. However, the post-experiment XRD result showed that all samples exhibited a pure Ni_3Ga phase, indicating a phase change during the reaction and the Ni_3Ga was the active site with the presence of promoters.

The combination of **Pd and Cu** was reported to be highly reactive for methanol synthesis. Pd-Cu/SiO_2 catalyst was first reported by Jiang et al.[74], and the highest methanol formation rate was observed when Pd/(Pd+Cu) was 0.34, which was two times higher than individual Pd or Cu monometallic catalyst. Moreover, the coexistence of the Pd-Cu and $PdCu_3$ alloy played a crucial role in methanol synthesis promotion. The promotion effect was further confirmed by theoretical calculations, indicating that the bimetallic interface facilitated H_2 and CO_2 adsorption[75]. Different Pd-Cu phases, such as Pd_3Cu_6 and Pd_6Cu_3, were further compared with Cu catalysts for the catalytic mechanism by DFT calculations[76]. The result indicated that the overall methanol selectivity was greatly promoted by inhibiting CO and CH_4 on Pd_3Cu_6(111) and Pd_6Cu_3(111) surfaces, because of the adsorption ability and interactions between intermediates and the active sites were tuned with the addition of Pd on Cu surface. Other Pd-based bimetallic catalysts, such as PdIn[77], PdCu, PdGa and PdZn were reported as potential candidates for methanol production. For example, Ojelade et al.[78] prepared a PdZn/CeO_2 catalyst via sol-gel method, and the optimized PdZn catalyst (Pd: Zn=1) exhibited a 100% methanol selectivity with 8% CO_2 conversion at 180 °C. The high methanol selectivity and mild reaction conditions were attributed to the formation of PdZn bimetallic alloy. A long lifetime Pd_2Ga/SiO_2 catalyst, was reported by Fiordaliso and co-workers, and it was reactive under ambient pressure, with 1.6 times higher reactivity compared with Cu-ZnO-Al_2O_3 catalyst[79]. The Pd-Ga bimetallic alloy, however, was found to be unstable when exposed to air[80]. PdIn intermetallic nanoparticles were reported to exhibit a 70% higher reaction rate compared with conventional Cu-ZnO-Al_2O_3 catalysts, and an elevated methanol selectivity (over 80%)[81].

2.3.2 Supported metal catalysts

Supports are favourable due to a large surface area, high thermal stability and some can even provide tunable pore sizes to facilitate the formation of catalyst particles[82].

The impregnation method is one of the most widely used methods to prepare metal-supported catalysts. Among them, the incipient wetness impregnation method (IWI) is well known for its fast and simple preparation process. Generally, a metal precursor containing catalytically active component is prepared by dissolving the

required metal nitrates in water. The precursor is then added dropwise to the support, and the volume of solution equals that of the support pore volume[83]. Modifications were made to IWI by introducing citric acid in the solution, coupling with the active component to obtain a uniform catalyst dispersion[82]. For supported metal catalysts, the impregnation method is quite simple and easy, however, poor stability due to sintering at high temperatures is observed. Modifications were carried out to increase its lifetime. For example, Wang et al.[84] prepared Cu-SiO_2 nanocatalyst via an ammonia-evaporation method. Specifically, aqueous ammonia solution was added to a metal precursor to form a complex solution, silica gel was subsequently added to the above solution, followed by a heating step to evaporate NH_3 and produce a highly active, well-dispersed catalyst with a long-lifetime.

Wisely selecting supports from a variety of possible candidates is one of the important steps in catalyst preparation. Mesoporous materials with an ordered porous structure, and moderate pore size can significantly enhance catalyst dispersion and improve the diffusion of reactants and products, contributing to higher catalytic performance. In addition, nano-structured materials, such as carbon nanotubes, also have advantages such as high surface area and excellent adsorption ability of H_2. Normally, inert supports are desirable due to their high chemical and thermal stability. As a result, silica and carbon are widely utilized as an effective material for supported metal catalysts. Previously, metal oxides such as ZnO and ZrO_2, introduced as promoters in the catalytic matrix, could also be denoted as supports, however, the electron transfer promotion and chemical interactions attracted more interest. Therefore, we will discuss the interactions between supports and active sites and exclude promoting effect between metal oxides and active sites.

1.3.2.1 Silicon dioxide (SiO_2)

Porous silica was commonly selected as a support for its high mechanical stability and large surface area and greatly enhanced the catalytic properties by stabilizing active components and preventing against sintering.

Porous silica is available with different dimension and pore structures. SBA-15 and MCM-41 are 2-dimensional mesoporous silica with long channels arranged hexagonally. These two materials have almost the same composition, while the

former contains micropores in the walls. KIT-6 is another mesoporous silica, with a 3-dimensional gyroid cubic structure[82]. Koizumi et al.[83] prepared MCM-41 and SBA-15 supported Pd catalysts by incipient wetness impregnation method. The result indicated methanol production rate was proportional to the average pore diameter of support. Pd-MCM-41catalyst exhibited the highest methanol formation rate with a large average pore diameter and an accordingly high Pd dispersion. Koh and co-workers[82] compared Cu deposited on different morphological mesoporous silica, namely SBA-15, MCF and KIT-6. The smallest Cu particle size was observed in Cu-Zn-Mn/KIT-6, and the reason was ascribed to a short pore channel in KIT-6, contributing to a better separation of Cu particles and avoiding the loss of mesopore volume such as in SBA-15. In addition, the high effective diffusivity in Cu-Zn-Mn/KIT-6 resulted in promoting reactant molecule transfer towards the active sites and a faster removal of products, leading to an enhanced reaction performance. The morphology of SBA-15 was also found to influence the activity of Cu-ZnO catalyst for CO_2 reduction to methanol, and fibre-shaped SBA-15 supported catalyst exhibited a higher Cu dispersion (29%) compared with the spherical-like SBA-15, contributing a higher CO_2 conversion (13.96%) and methanol selectivity (91.32%)[85].

1.3.2.2 Carbon

Carbon as a widely used support exhibits several advantages, for example, it provides high metal dispersion and it facilitates the reduction of the metal precursor. Sawdust was the first resource of activated carbon (AC), reported by Sakata et al.[86], and the derived AC showed a moderate surface area (roughly 200 m^2/g). However, the microporous structure in AC could not help confining particles within the pores and the mass transfer was inhibited due to a small pore size.

Nanocarbon material later drew increasing attention, especially carbon nanotube (CNT), as a novel material to prepare supported catalysts. Multiwall CNT possessed a graphitized tube-wall, demonstrating a high electrical conductivity and high surface area. It was worth mentioning that it also exhibited a great hydrogen adsorption ability. These characteristics contributed to novel catalyst support or promoter[87]. Liang et al.[87] prepared a multiwall CNT supported Pd-ZnO catalyst, and an increasing amount of catalytically active Pd species were reduced by CNT support. Moreover, the hydrogen adsorption ability contributed to a higher

concentration of surface H atom species, greatly improving the rate of surface hydrogenation reactions. Similar results were reported by Dong and co-workers[88] via a CNT-promoted Cu-ZnO-Al_2O_3. It was worth mentioning that the reversible hydrogen adsorption on CNT was feasible up to 573K, suggesting that methanol synthesis would be promoted under the reaction conditions due to an enhanced spillover effect between Cu and ZnO[88,89]. In addition, the nitrogen-decorated CNT supported Cu-ZrO_2 was investigated for methanol synthesis properties. Bao et al.[90] compared different nitrogen sources of CNT, and the results indicated pyridinic nitrogen resulted in strong CO_2 adsorption, contributing to a highly promoted methanol synthesis catalyst with a highly uniform Cu dispersion.

The AC and CNT were found to facilitate the overall catalytic properties; however, the specific area was still low (i.e., less than 200 m^2/g)[91]. Recently, graphene has attracted wide interests because of its high surface area (i.e., over 2000 m^2/g) and extraordinary thermal and chemical stability. Witoon et al.[92] reported a 1 wt% Cu-ZnO-ZrO_2/graphene oxide catalysts which revealed a higher catalytic performance compared with graphene-free Cu-ZnO-ZrO_2 catalysts. They suggested that the graphene was acting as bridges, transferring the dissociated hydrogen and intermediates to ZnO and ZrO_2, for further hydrogenation.

1.3.2.3 Layered double hydroxides (LDH)

LDH is an anionic clay, which has been introduced in previous sections, as a template for catalyst preparation. Generally, LDH has a porous structure and a double-layer gallery, where CO_2 and H_2O can be stored as carbonates and hydroxides. Hence, LDH is also considered as a great candidate for CO_2 and H_2O adsorption, especially at high temperatures. The LDH derived oxides, derived from thermal treatment of LDH, also exhibits high CO_2 adsorption. Leon et al.[93] investigated the sorption mechanisms for adsorption irreversibility. The results suggested the CO_2 adsorption on strong basic sites was irreversible due to the formation of unidentate CO_2 adsorbent species. However, highly reversible adsorption was found on weaker basic sites. This property attributes to a fact that the catalysts supported by LDH/LDH-derived metal oxides could promote catalytic performance.

Xin et al.[94] prepared a Cu-ZnO-ZrO_2 catalyst supported on Mg-Al LDH via a co-precipitation method. The as-prepared catalysts exhibited uniformly dispersed metal nanoparticles, which was closely attached to the surface of LDH. In addition, high CO_2 adsorption on LDH contributes to an increasing CO_2 concentration near the active sites, which promoted the methanol synthesis reaction.

2.3.3 Reaction mechanism

The reaction mechanism has been investigated in the past few years; however, the results are still an area of debate. Two main reaction mechanisms have been proposed, namely a formate pathway and a rWGS pathway, as can be seen from Fig. 6. In the formate pathway, CO_2 is adsorbed and hydrogenated to formate (HCOO*), followed by a stepwise hydrogenation to dioxomethylene (H_2COO*) and formaldehyde (H_2CO*). In the other proposed pathway, CO_2 is firstly transformed into hydrocarboxyl (HOCO*), and CO is generated from HOCO* via rWGS reaction, which is further hydrogenated to formyl (HCO*) and H_2CO*. Methanol is produced via key intermediates, formaldehyde (H_2CO*) and methoxy (H_3CO*) from both possible reaction pathways.

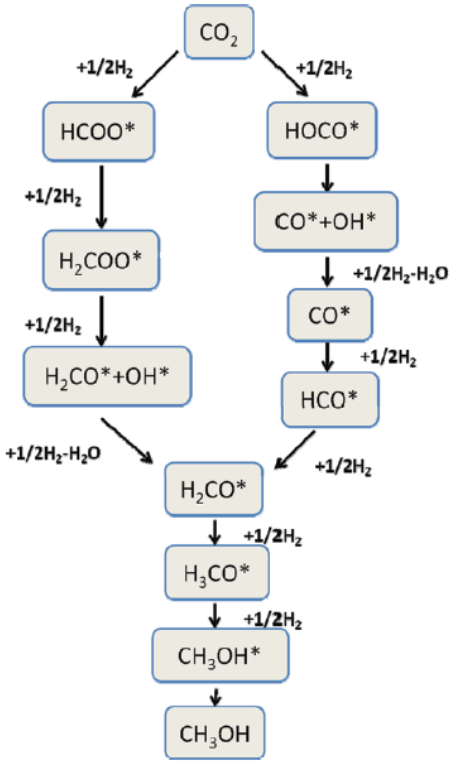

Fig. 6 Reaction network scheme of the formate pathway and the rWGS pathway[95]

The active sites coupling with metal oxides were found to be highly active for methanol production, and a great number of research has been conducted to study the mechanism via active site/ metal oxide interfaces. Cu-ZrO_2 interface was one of the most widely investigated fields, and the formate pathway was mostly supported by many researchers. Hong and co-workers simulate[96] and calculate the mechanism over the (212) plane on Cu/ZrO_2 by Monte Carlo simulations. The results showed over 90% CO_2 was converted to methanol via a formate pathway, and CO was generated either by little amount of CO_2 hydrogenated via rWGS or by decomposition of H_3CO* produced via the formate pathway. Similar DFT calculations were reported by Larmier et al.[97] CO_2 exhibited the lowest free energy when adsorbed on the Cu/ZrO_2 interface, followed by the ZrO_2 surface, and it hardly adsorbed on the Cu surface. Free energy of key intermediates from both pathways, namely COOH* and HCOO*, were further calculated accordingly. The lowest free energy was observed in HCOO*, indicating the overall reaction will preferably follow the formate pathway. The calculation was further evaluated by in situ IR and NMR measurement, which reported that H/D exchanged formate species participated in the methanol formation. A similar result was observed in the La-promoted Cu-Zn-Al catalyst, suggesting both methanol and CO were produced from surface formate species based on the DRIFT result[98]. Atakan et al.[99] suggested that methanol was synthesized via a formate pathway, and dimethyl ether was directly formed from H_3CO* over a Cu-Zr-SBA-15 catalyst. In addition, Chen et al.[2] investigated the crucial role of Cu-LaO_x via in-situ DRIFTS studies, and the results revealed that HCOO* and H_3CO* were detected, suggesting the formate pathway was preferable rather than rWGS route. Pd/Ga_2O_3 catalyst was reported to follow a formate pathway as well. However, Ga_2O_3, in the case of the Pd/Ga_2O_3 interface, was found to be highly active for methanol synthesis, and the Pd-Ga bimetallic particles dissociated and spilled over hydrogen atom to Ga_2O_3 surface[79].

Others supported the rWGS reaction pathway and some fundamental study was reported in recent years. DFT calculations were used to understand the reaction mechanism on a stepped Ni_5Ga_3(111) and a Ni_5Ga_3(211) surface[100,101]. The results indicated that the dissociative adsorption of H_2 on Ni_5Ga_3 (221) surface was almost with no barrier, and this contributed to the promoted reaction rate of methanol synthesis. On stepped Ni_5Ga_3 (111) surface, the energy barrier was lower than

Ni_5Ga_3 (211) surface, and the reactivity on stepped (111) surface was even more active than the stepped Cu (211) surface. It was also suggested that the rWGS reaction pathway was agreed to be the most favourable route for its comparatively low energy barrier. Zhao et al.[102] tried to explore all possible pathways on the Cu(111) by DFT calculation, and the result showed methanol synthesis via formate pathway was not possible due to a high free energy barrier for HCOO* and H_2COO*. As a result, the rWGS was found feasible for methanol synthesis, and water was also considered indispensable on clean Cu(111) surface at low temperature. Tao and co-workers agreed that the rWGS pathway was preferred for methanol synthesis where CO_2 was hydrogenated to HOCO free radical, followed by further hydrogenation to methanol with an enthalpy energy of -35.39 kJ/mol[103]. A highly active Cu/CeO_2, with 14 times higher catalytic performance compared to Cu/ZnO was also reported to follow the rWGS pathway for methanol synthesis. The reaction route was investigated by APXPS measurement, and the only species observed was $HCOO^-$. However, when DFT calculations were further carried out, the results indicated $HCOO^-$ was too stable to convert to methanol with a high activation energy barrier. The absence of HCO*, H_2CO* and H_3CO* in the rWGS pathway was because of a low residence time under reaction conditions[52]. Yang et al.[95] investigated the reaction route over different catalyst planes by a DFT calculation and Kinetic Monte Carlo simulations. The report indicated the reaction pathway varied depending on different catalyst compositions. Generally, the formate pathway was preferred in methanol production, however, doping some active metals, such as Pd, Rh, Pt and Ni, can help stabilize intermediate like CO* and HCO*, which then promote the methanol synthesis via rWGS pathway.

Chapter 3 Methodologies and Characterisation

3.1 Reagents and materials

3.1.1 Reagents

The chemicals used in this study are listed in Table 1. The reagents were used without further purifications.

Table 1 Reagents used in this study

Reagents	Formula	Purity	Manufacturer
Nickel nitrate hexahydrate	$Ni(NO_3)_2{\cdot}6H_2O$	98.5%	Sigma Aldrich
Gallium nitrate hydrate	$Ga(NO_3)_3{\cdot}9H_2O$	99.99%	Changsha Easchem Co., Limited
Magnesium nitrate hexahydrate	$Mg(NO_3)_2 \cdot 6H_2O$	98.0%	Sigma Aldrich
Zinc nitrate hexahydrate	$Zn(NO_3)_2 \cdot 6H_2O$	98.0%	Sigma Aldrich
Zirconium oxynitrate hydrate	$ZrO(NO_3)_2 \cdot xH_2O$	99.0%	Sigma Aldrich
Urea (powder)	NH_2CONH_2	99.0%	Sigma Aldrich
De-ionized water	H_2O	N.A.	Lab supply

3.1.2 Materials

Pural MG50 is a commercial hydrotalcite-like compound, produced by the Sasol company. It has a typical layered structure, with carbonates and hydroxides stored between the layers. The elemental composition included 50% (weight) MgO and 50% Al_2O_3. The activated hydrotalcite exhibited a specific surface area of 200 m^2/g. 13X beads were procured from UOP.

The commercial Cu-based methanol synthesis catalyst is produced by the Alfa Aesar company. The elemental composition is 63.5% (weight) CuO, 24.7% ZnO and 10.1% Al_2O_3, determined by manufacturers.

3.2 Characterisation

3.2.1 Structural and morphology characterization

1) X-Ray Diffraction (XRD)

The phase purity information of samples was collected by lab powder X-ray diffraction (PXRD) on a Phillips Analytical PW1140/90 X-ray diffractometer with a Cu Kα radiation (wavelength 1.404λ; 2θ from 5 to 90°). Phase identification, particle size and crystal lattice parameters of samples were fitted and analyzed by TOPAS 5 software (Bruker). The broadening of peaks in PXRD was influenced by both size and lattice strain. As a result, the Voigt-function model was used to obtain correct particle size and to remove the effect of lattice strain[104].

The in-situ synchrotron H_2-PXRD was conducted in the Powder Diffraction beamline at Australian Nuclear Science and Technology Organisation (ANSTO). The samples were packed in a 0.7 mm quartz capillary. Prior to the experiment, the capillary was vacuumed in-situ, and then required H_2 was introduced into the capillary. The sample was heated from 30 °C to 700 °C with a ramping rate of 5 °C/min. The XRD pattern was collected every 50 °C, and the temperature was kept constant for each point for 60s. A Mythen-II detector was used for data collection with an X-ray wavelength of 0.7733 Å for all samples.

2) Microscopy (SEM, HIM and HRTEM)

The surface morphologies of the samples were examined by a high-resolution scanning electron microscope with energy dispersive X-ray spectrometry (SEM-EDS, JSM-7001F, JEOL), and Helium-ion beam microscopy [(HIM) (Carl Zeiss, Orion Nanofab, Peabody MA, USA)].

The structural features, such as fringes, and elemental distributions were analysed by the High-Resolution Transmission Electron Microscopy (HRTEM) on a Philips CM20 and FEI Tecnai F20. The samples were finely crushed, dispersed into 10 mL ethanol, sonicated for 5 minutes, before loading on the Cu grid.

3) Inductively Coupled Plasma spectrometry (ICP)

The analysis of the composition of samples was carried out by an induced plasma spectrometry (ICP Varian 720-ES). To prepare the standard Mg^{2+} concentration curve, $Mg(NO_3)$ was dissolved in distillate water , and achieved a series of Mg^{2+} concentration, ranging from 0 to 0.5 mmol/L. Prior to the measurement, the samples were dissolved in HNO_3, and diluted until desirable.

4) Thermogravimetric Analysis (TGA)

The thermal stability of the samples was measured by a thermogravimetric analyzer (TGA, Mettler Toledo). The fresh samples were dried at 100 °C overnight prior to the measurements. The tests were performed within the temperature range of 30 °C to 750 °C with a heating rate of 2 °C min^{-1} under a constant N_2 flow of 30 mL min^{-1}.

The TGA-CO_2 stability test was carried out under similar conditions. The fresh samples were dried overnight at 100 °C prior to measurements. The CO_2 stability tests were performed within the temperature range of 30 °C to 800 °C with a heating rate of 2 °C min^{-1} under a constant CO_2 flow of 40 mL min^{-1}.

5) N_2 adsorption-desorption measurement

The specific surface area of samples was determined by a N_2 adsorption-desorption measurement, at -196 °C in a liquid nitrogen environment (Micromeritics 3-flex instrument, USA). The pre-treatment included degassing the samples to 0.0133 Pa at 300 °C for 3 hours. The specific surface area and pore size distribution were calculated with Brunauer-Emmett-Teller (BET) and Horvath-Kawazoe (H-K) models, respectively.

6) X-ray absorption spectroscopy (XAS)

The local structural information, including electron state and crystal structure of the samples, was obtained by X-ray absorption spectroscopy (XAS) experiments at XAS beamline, Australian Synchrotron (ANSTO). A fluorescence mode was used for the detection of Gallium k-edge by a multi-element solid state Ge fluorescence detector in a cryostat at -263 °C. The obtained data were processed and analyzed with the Demeter software package[105]. The parameters describing the structural information were obtained by fitting the measured data to a theoretical path model generated by FEFF6 in R-space for the first coordination shells, including coordination number (*CN*), amplitude factor (S_0^2), bond distance (*R*), Debye-Waller factor (σ^2), and inner potential shift (ΔE_0).

7) X-ray photoelectron spectra (XPS)

X-ray photoelectron spectra (XPS) of the catalysts were measured on a Thermo Scientific K-alpha X-ray photoelectron spectrometer system equipped with an Al K-alpha source. The binding energy was referenced to the adventitious C 1s peak at

284.6 eV, and the corresponding binding energies of Ni 2p and Ga 3d were corrected, respectively.

3.2.2 Reducibility and adsorption characterization

1) Temperature Programmed Reduction (TPR)

The reducibility of the materials was determined by conducting the temperature-programmed reduction (TPR) on BEL-Cat (Bel Japan Inc.). The sample was treated at 300 °C for 1 hour in a Helium atmosphere and gradually cooled to room temperature. The TPR measurement consisted of the reduction of the catalyst with a 5% H_2/Ar mixture gas at a flowrate of 30 mL min^{-1}, with a temperature range from 30 °C to 850 °C at a ramping rate of 2 °C. The amount of H_2 consumption was monitored by a thermal conductivity detector (TCD) during the entire measurement.

2) Temperature Programmed Desorption TPD-CO_2

The basicity of the samples was evaluated by means of temperature-programmed desorption (TPD) of CO_2. The outlet gases were analysed by a TCD detector. Initially, the samples were reduced in-situ at 700 °C under 5% H_2/Ar mixed gas for 6 hours, and then cooled down to room temperature. The surface of the samples was then saturated with CO_2 (5% in He) for 1 hour at 60 °C. The excess adsorbed CO_2 was purged with He for 1 hour at 60 °C, followed by cooling to room temperature. Finally, the TPD of CO_2 was measured in He gas flow with a heating rate of 2 °C min^{-1} up to 700 °C.

3) CO_2 adsorption isotherm

High-temperature CO_2 adsorption was measured by a BELSORP instrument (Model BELSORP-max, BEL Co., Ltd.). All samples were degassed for 6 hours at 400 °C prior to the experiment. The isotherms were measured at 200 °C, 250 °C and 300 °C.

3.3 Catalytic performance evaluation

The activity of the catalysts for the CO_2 hydrogenation reaction was measured in a fixed bed micro reactor, as shown in Fig. 7. The reactor was equipped with three feed gas pipelines, including pure N_2 for flushing the entire system, pure H_2 to

reduce the catalysts, and a gas mixture with 75%H_2 balanced with CO_2 as a reactant for methanol synthesis. The catalysts samples (1 g, 40-60 mesh), diluted by the same amount of quartz sand, were placed into the centre of the reactor column. The reactor was covered by a 3-stage heater, and a temperature controller was placed in the centre of the catalysts to maintain the specific temperature during the entire reaction. Prior to the reaction, pure N_2 was purged for at least one hour to remove the impurities, such as oxygen and residue products. The H_2/CO_2 was then introduced into the reactor, the flowrate of which was controlled constantly by a mass flow controller, and the reactor was heated to the required temperatures for methanol synthesis reaction. The pressure was increased stepwise to the desired pressure (30 bar) and kept constant during the reaction. The exhaust gas was collected and measured by a gas chromatography (GC, 7890B, Agilent Technologies) with a thermal conductivity detector (TCD) and flame ionization detector (FID), respectively, and the residue was cooled by a cold trap.

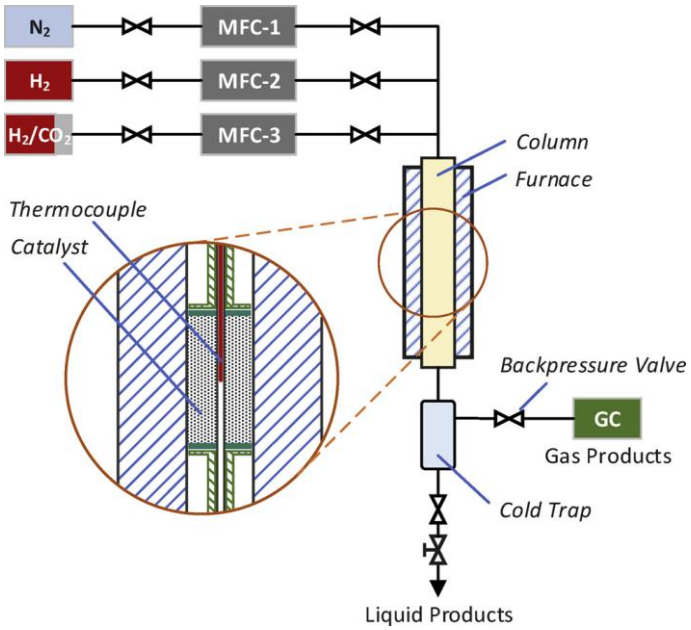

Fig. 7 Micro-reactor structure for methanol synthesis[94]

The methanol selectivity (S_{MeOH}), methanol yield (Y_{MeOH}) and methanol space-time yield (STY_{MEOH}) were defined as,

$$S_{MeOH} = \left[1 - \frac{F_{out} \times (f_{CO} + f_{CH_4})}{F_{in} \times f_{co_{2_{in}}} - F_{out} \times f_{CO_2}}\right] \times 100\% \quad (7)$$

$$\mathrm{Y_{MeOH}} = (1 - \frac{F_{out} \times f_{co_2}}{F_{in} \times f_{co_2{}_{in}}}) \times S_{MeOH} \times 100\% \quad (8)$$

$$STY_{MeOH} = \frac{F_{in} \times f_{CO_2{}_{in}} - F_{out} \times f_{CO_2}}{22.4 \times g_{cat}} \times Y_{MeOH} \times M_{MeOH} \quad (9)$$

Where, F_{in} is the inlet H_2/CO_2 mixed gas molar flowrate, f_{co2in} is the CO_2 molar fraction in the feed gas, and f_{CO2}, f_{CO} and f_{CH4} are the molar percentage of CO_2, CO and CH_4, respectively, in the exhaust gas, which was calculated based on GC measurement results. In addition, g_{cat} is the mass of catalyst, and M_{MeOH} is the molar weight of methanol. In the exit gas, CO, CH_4 and CH_3OH are the only detected carbon-based products in GC measurements, and thus the carbon-balance was calculated by considering CO_2 and the three products described above.

Chapter 4 Synthesis of Ni_5Ga_3 catalyst by Hydrotalcite-like compound (HTlc) precursors for CO_2 hydrogenation to methanol

4.1 Introduction

As discussed in Chapter 2, the Ni-Ga catalytic system exhibited a high methanol synthesis activity. Among all three Ni-Ga phases, Ni_5Ga_3 was reported to reveal a comparable CO_2 conversion and high methanol selectivity with Ni_3Ga and NiGa. However, synthesis of highly pure Ni_5Ga_3 was found to be very difficult. For example, Ni_5Ga_3 prepared from incipient wetness impregnation method and co-precipitation method resulted in some purities, such as Ni_3Ga, revealed from PXRD patterns. Hence, preparation of pure Ni_5Ga_3 was investigated in this section via a HTlc precursor as a template. In this chapter, we discuss a preparation method of Ni_5Ga_3 bimetallic catalyst via Ni-Ga HTlc precursors, and its corresponding catalytic performance for CO_2 hydrogenation to methanol. The structural and morphological impact of synthesis temperature on HTlc precursor and the derived Ni_5Ga_3 catalysts were characterized by a powder X-ray diffraction (PXRD), thermal gravimetric analysis (TG), scanning electron microscopy (SEM) and X-ray absorption spectroscopy (XAS). The relationship between the structure of the HTlc precursor and the property of the derived Ni_5Ga_3 bimetallic catalyst was investigated accordingly. The optimized hydrothermal temperature for HTlc precursor was determined, based on the catalytic properties of CO_2 reduction to methanol via as-prepared Ni_5Ga_3 catalysts prepared under different temperature.

4.2 Methodologies

4.2.1 Catalyst synthesis

4.2.1.1 Ni-Ga HTlc precursor synthesis

The Ni-Ga HTlc precursor was prepared by a hydrothermal synthesis via urea hydrolysis method. All the chemicals were used without further purification. Typically, $Ni(NO_3)_2{\cdot}6H_2O$ and $Ga(NO_3)_3{\cdot}9H_2O$ were dissolved in 50 mL distilled water in a molar percentage ratio of 65% to 35% with a total cationic concentration of 0.5 mol/L. Urea with the same ratio of nitrates was then dissolved in the aqueous solution with vigorous stirring. Different samples of the as-prepared mixed solution were sealed in a hydrothermal reactor (Parr reactor model 4748) at 90°C, 110 °C,

130°C and 150°C to investigate the effect of synthesis temperature. The product was maintained at reaction temperatures for another 16 hours, and then centrifuged and washed at least 4 times, with deionized water, and dried at 100 °C overnight. The precursors were named as x-HTlc, where x indicated the corresponding urea hydrolysis synthesis temperature.

4.2.1.2 Ni_5Ga_3 bimetallic catalyst synthesis by reduction of HTlc precursors

The dried cake x-HTlc produced above was collected, crushed and sieved with a 40-60 mesh. The meshed HTlc precursors were further reduced in a sealed tube furnace, flowing a mixed gas containing 5% H_2 balanced with Ar, at a flow rate of 40 mL/min, at 700 °C with a ramping rate of 5 °C/min, and then maintained at 700 °C for another 6 hours. The corresponding reduced Ni-Ga bimetallic alloy was denoted as x-Ni_5Ga_3. The reduced catalysts were immediately transferred to a fixed bed reactor to avoid any surface oxidation of the bimetallic catalyst.

4.2.1.3 Ni-Ga bimetallic catalyst synthesis by impregnation method

To compare the Ni_5Ga_3 formation and purities between different preparation methods, as well as to understand the ease with which the Ni_5Ga_3 phase could be synthesized, the Ni-Ga bimetallic alloys were also synthesized by a conventional impregnation method. Specifically, nickel and gallium nitrates (Ni:Ga molar ratio varied from 58:42 to 65:35) were mixed in 50 mL distilled water with an overall cationic concentration of 0.5 mol/L, which was similar to the synthesis of HTlc precursor described above. The solution was then evaporated, dried overnight at 100 °C and then reduced by 5% H_2 in Ar at 700 °C for 6 hours, as described earlier in section 3.2.1.2. The obtain the as-prepared Ni-Ga bimetallic samples were denoted as i-Y%-NiGa (Y refers to nickel molar percentage).

4.3 Results and Discussion

4.3.1 Effects of hydrothermal temperature on the structural properties of HTlc precursors

4.3.1.1 Crystal structure analysis of HTlc precursors with PXRD patterns

The PXRD patterns of x-HTlc precursors synthesized at different temperatures are shown in Fig. 8. As can be seen in Fig. 8, the reflections for (00l) lattice plane, like

(003), (006) and (009) at low angles between 10° to 35°, were sharp and symmetric. The peak shape indicated the formation of a typical layer structure in the HTlc precursor. The peaks located at a higher 2θ angle above 35°, exhibited a relatively asymmetric and broad shape corresponding to the lattice planes (012), (015) and (018). However, the (012) plane overlapped with (009) plane, resulting in a small shoulder in the original (009) peak area. The (110) plane, which described the plate-like layer horizontally, was also overlapped by (113) plane. As can be seen in the patterns, the intensity of these peaks increased as hydrothermal temperature increased, suggesting an increasingly perfect and stable structure of HTlc precursor synthesized at elevated temperature. However, the 90 °C-HTlc exhibited relatively weak and unclear peaks, indicating the formation of HTlc was incomplete. The results suggested that hydrothermal temperature greater than 90 °C was appropriate for Ni-Ga HTlc precursor synthesis.

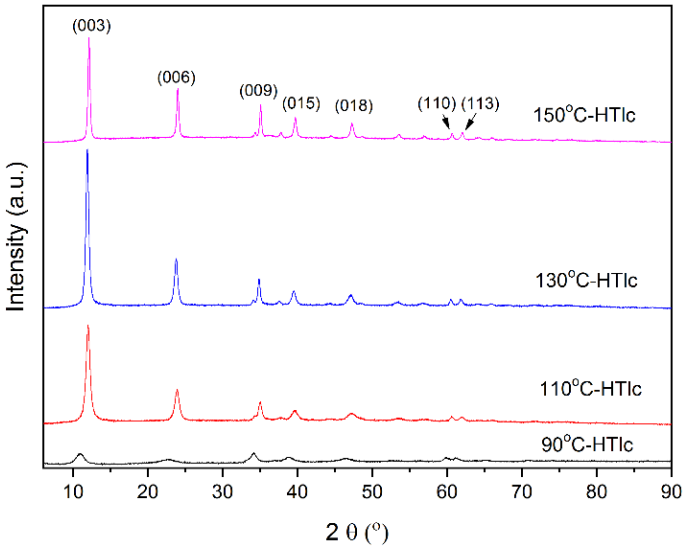

Fig. 8 PXRD patterns of x-HTlc precursors prepared at a hydrothermal reaction temperature between 90 °C-150 °C

The crystal structure of the HTlc precursor belonged to R3m space group, with a rhombohedral unit cell. As can be seen from Fig. 9, The nickel and gallium atom were wrapped by hydroxide radical and consisted of an octahedral basic unit, which constructed a layer structure in a-b plane. To describe the crystal structure of HTlc precursor, lattice parameters *a* and c, represented an average distance between cations on the layers, such as Ni^{2+} and Ga^{3+}, and three times of the thickness of interlayer distance, respectively, was calculated based on the equation, $a=2\,d(110)$ and $c= 3*(d(003)+d(006)*2)/2$[106]. The corresponding cell volume of the HTlc

precursors was then calculated according to: $V=(a^2c)\sin 60°$[107], as shown in Table 2. The results demonstrated that the cell volume, as well as both lattice parameters a and c, decreased slightly as the hydrothermal temperature in HTlc synthesis increased.

The growth of the crystallite size of HTlc precursors was depicted from two directions, namely [003] and [110] direction, respectively, and the Scherrer Equation was used to calculate the average crystallite size according to different directions, $d=K\lambda/\beta\cos\theta$, where K is the shape factor, λ is the X-ray wavelength, β is line broadening at half the maximum intensity.

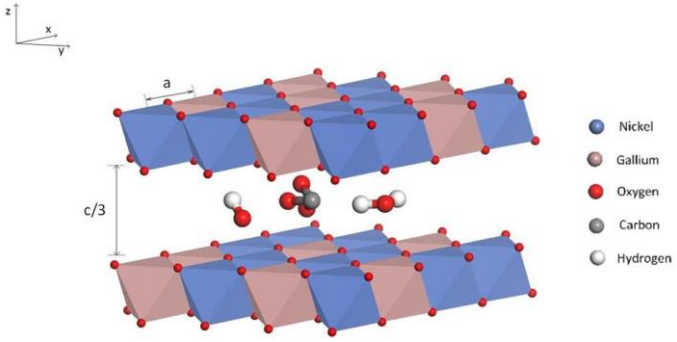

Fig. 9 Crystal structure of Ni-Ga type HTlc

Table 2 Lattice parameters of x-HTlc precursors synthesized under different temperatures.

Samples	a(Å)	c(Å)	Unit cell volume(Å)
90 °C-HTlc	3.09±0.08	23.94±0.18	197.96
110 °C-HTlc	3.06±0.08	22.35±0.18	181.24
130 °C-HTlc	3.06±0.08	22.35±0.18	181.24
150 °C-HTlc	3.05±0.08	22.04±0.18	177.56

The size from [003] direction described the growth of the thickness of interlayer distance while that in [110] direction related to the growth of the layer horizontally. The reason was ascribed to the fact that HTlc was a plate-like shape, with lateral average size exceeding the longitudinal size, and thus the particle size would be inaccurate if it was described as a sphere with one average diameter. As can be seen in Fig. 10, both the crystallite sizes in the [003] and [110] directions were enlarged at elevated hydrothermal synthesis temperatures. The growth of HTlc crystallite size derived from PXRD calculation is consistent with the previous report,

that an elevated synthesis temperature contributed to the accelerating growth of HTlc[24].

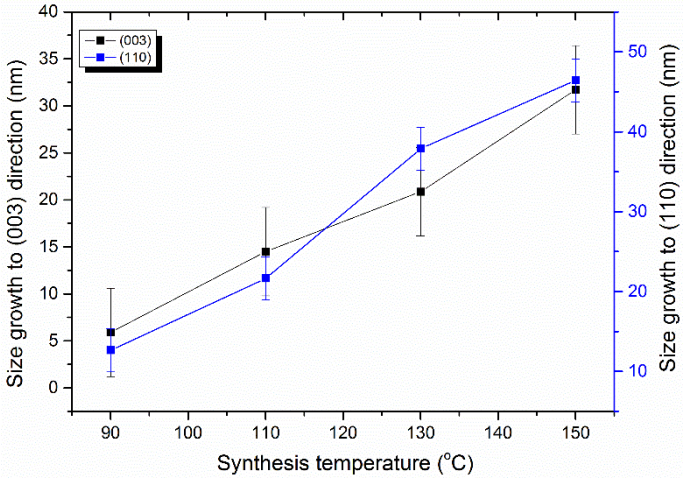

Fig. 10 Crystallite size of HTlc precursor in [003] and [110] directions

4.3.1.2 Morphologies of HTlc precursors

HTlc samples prepared by the hydrothermal method presented plate-like structures, as can be seen from Fig. 11, instead of the “sand rose” morphologies prepared by conventional co-precipitation method[108]. The controlled urea hydrolysis method provided a mild pH change during the hydrothermal reaction, contributing to a slow and uniform nucleation formation process, and thus it could produce a relatively “diluted” and well-separated disk-like particles, avoiding severe agglomerations compared with conventional co-precipitation method. It was also observed that complete plate-like shapes and well-defined edges appeared with the increasing temperature of the hydrothermal reaction, suggesting a complete HTlc structure at elevated synthesis temperature.

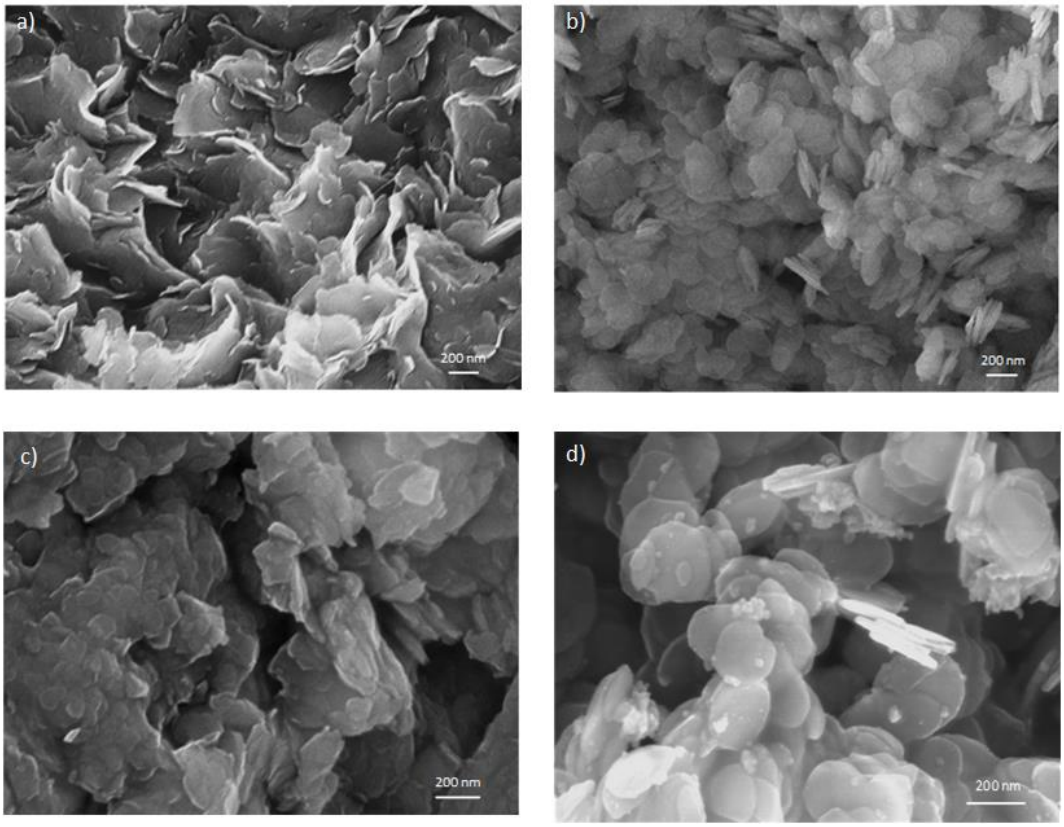

Fig. 11 SEM images of a) 90 ºC-HTlc precursor, b) 110 ºC-HTlc precursor, c) 130 ºC-HTlc precursor, d) 150 ºC-HTlc precursor

To procure more detailed morphology information, an HIM image of 110 ºC-HTlc was captured and is, shown in Fig. 12. The thickness along the interlayers in the macroscale was around 12-16 nm, which was in accordance with the calculations shown in Fig. 10. However, the thickness was observed to be around 40 nm, which was formed by overlapping or stacking of many HTlc single layers.

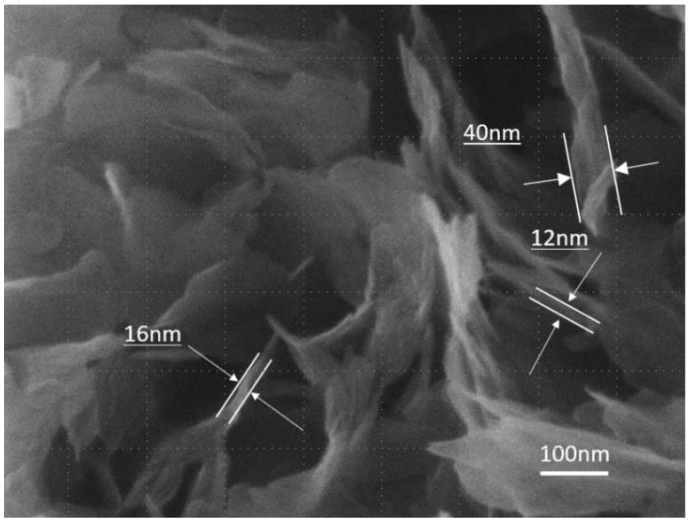

Fig. 12 HIM of 110 °C-HTlc

4.3.1.3 Thermal stability of HTlc precursors

The TG patterns of the x-HTlc precursors are shown in Fig. 13. Generally, two steps of weight loss were observed (except 90°C-HTlc sample), and the strength of the peaks in derivative thermogravimetry (DTG) curves increased as the hydrothermal reaction temperature increased. The first weight loss step was attributed to the desorption of the physically adsorbed water stored in HTlc interlayers. The dehydroxylation and decarbonation, occurred simultaneously at higher temperature contributed to the second weight loss peak in DTG curve due to a higher binding energy compared with physically adsorbed water[109]. The HTlc structure was completely decomposed over 500 °C because no further weight loss was observed at elevated temperature.

The calculated weight loss percentages and the corresponding temperatures due to water removal, dehydroxylation and decarbonization in DTG curves are shown in Table 3. As mentioned earlier, two weight loss steps were observed in the DTG curve for samples 110°C-HTlc, 130°C-HTlc and 150°C-HTlc. Specifically, the first step appeared between 157 °C and 200 °C while the second major loss peak was located between 287 °C and 301 °C. In summary, both peaks shifted to a higher temperature as hydrothermal temperature increased, suggesting an increase in stability at elevated temperature. In contrast to other samples, 90°C-HTlc exhibited only one peak at 300 °C, surprisingly the peak around 100 °C, due to the desorption of physically adsorbed water, was missing. As discussed earlier, HTlc precursor was poorly crystallized and exhibited instability at low hydrothermal temperature, accordingly the “first” weight loss peak of 90°C-HTlc shifted to a lower temperature, potentially lower than 100 °C. The pre-treatment of all samples involved heating all the materials at 100 °C, possibly at this stage the physically adsorbed water was already removed, contributing to the absence of the first peak of 90°C-HTlc in DTG curves.

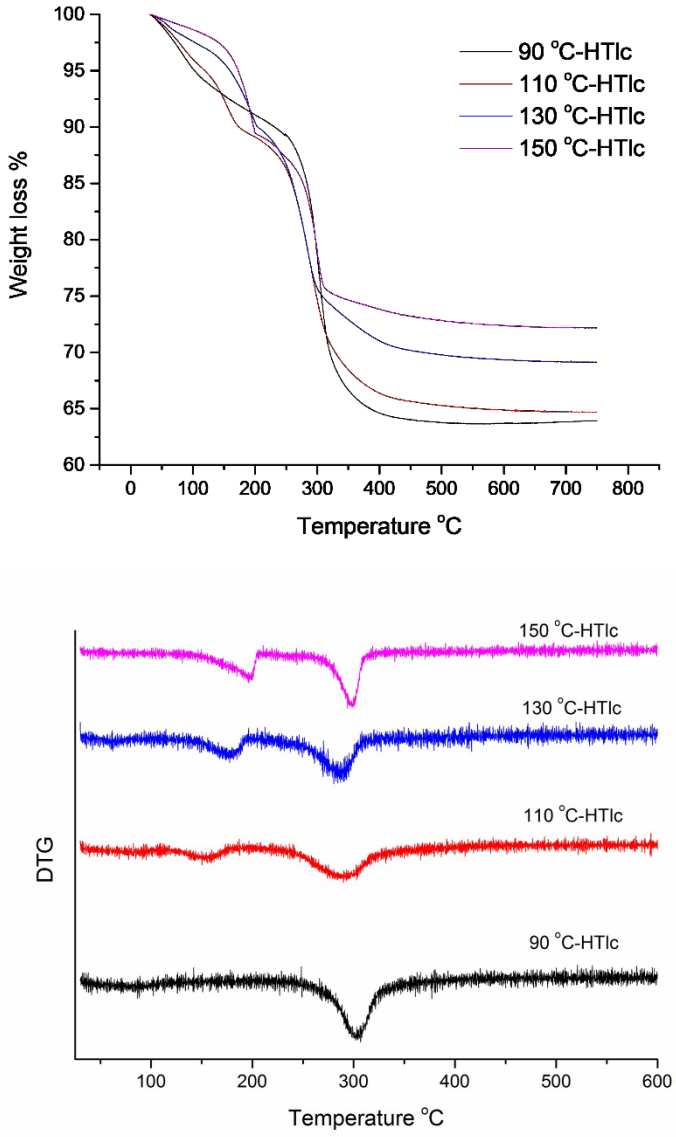

Fig. 13 TG and DTG curve for x-HTlc precursors

Table 3 Weight loss of water/carbonates and hydroxides of HTlc precursors

Sample	Weight loss% (first/second step)	DTG temperature peaks °C (first/second step)
90 °C-HTlc precursor	~/24.7	~/305
110 °C-HTlc precursor	10.4/20.9	158/287
130 °C-HTlc precursor	10.6/24.9	179/287
150 °C-HTlc precursor	11.8/25.4	200/301

4.3.1.4 Surface characterization of HTlc precursors

The specific area, pore volume and pore size of HTlc precursors were summarized in Table 4. BET surface area remained almost constant in all the samples. The pre-treatment, included calcination for removal of the interlayer anions, creating vacancy and pores in the calcinated precursor, contributing to a moderate surface area generated from the layered structure.

Table 4 Surface area of x-HTlc Precursors

Sample	BET surface area (m^2/g)	Pore volume (cm^3/g)
90 °C-HTlc	176.3	0.14
110 °C-HTlc	174.4	0.17
130 °C-HTlc	174.6	0.32
150 °C-HTlc	173.4	0.24

A typical mesoporous structure of HTlc was revealed from a hysteresis loop in N_2 adsorption-desorption isotherm. The mesoporous pores were generated from the pre-treatment, due to the removal of CO_2 and H_2O previously formed as carbonates and hydroxides stored between the interlayers. And the pore volume increased as the hydrothermal temperature increased, as shown in Table 4. Additionally, all the samples showed a uniform micropore size distribution as shown in Fig. 14, calculated by H-K model[110], with pores size ranging between 3 Å to 5 Å. The micropores corresponded to those from the typical octahedral unit in the double-layered structure.

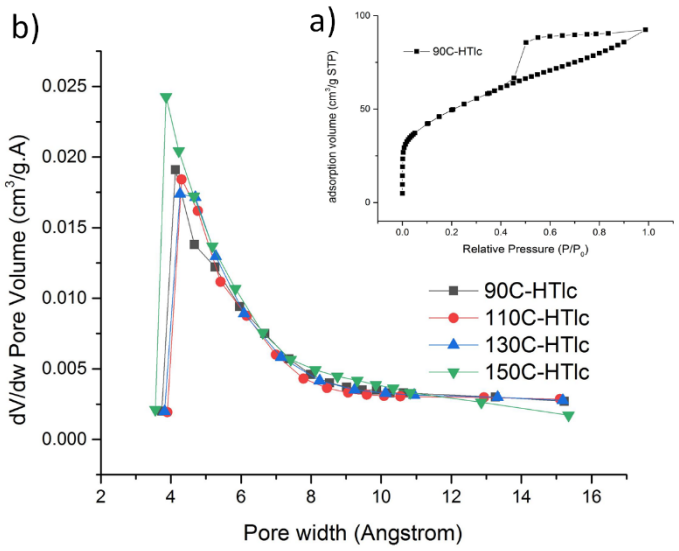

Fig. 14 a) N_2 adsorption-desorption isotherms, b) pore distributions for x-HTlc precursors

4.3.2 Textural and structural properties for as-prepared Ni_5Ga_3 catalysts

4.3.2.1 PXRD patterns and structural analysis of Ni_5Ga_3

As can be seen from Fig. 15, all samples exhibited clear and strong reflections, positioned at 2θ = 43.2°, 48.4°, 54.5°, 72.5°, 75.2° and 86.5°, which corresponded to the Ni_5Ga_3 crystal planes (221), (002), (040), (402), (440) and (223) respectively[111]. The impurities, such as Ni_3Ga could be not be observed in the PXRD patterns, indicating that an ultra-pure Ni_5Ga_3 was synthesized by this method. A typical Ni_5Ga_3 structure belongs to a Cmmm space group, with an orthorhombic unit cell, hence, lattice parameters a, b, and c were used to depict the three-dimensional crystal structure. The as-calculated lattice parameters a, b and c, and the particle size as well as lattice strain, based on the PXRD data, are summarized in Table 5. The result revealed that the crystal expanded in the x and z-axis directions, while contracted along y-axis direction, as the hydrothermal synthesis temperature for HTlc precursor increased. Correspondingly the unit cell volume exhibited an increasing trend with an increase in hydrothermal temperature. The particle size was calculated accordingly, and the smallest particle size was observed in 110 °C-Ni_5Ga_3, and the particle size increased as the precursor crystallized size increased, resulting in the largest particle size in 150 °C-Ni_5Ga_3 sample.

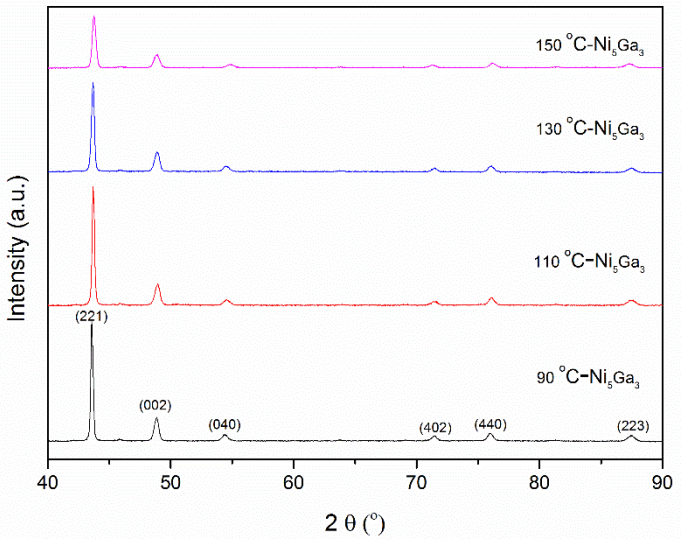

Fig. 15 PXRD patterns of as-prepared x-Ni_5Ga_3 catalysts

Table 5 Information of crystal structure for Ni_5Ga_3 prepared from different reaction temperatures

	a (Å)	b (Å)	c (Å)	Unit Cell volume (Å^3)	Crystallized size (nm)
90 °C- Ni_5Ga_3	7.500	6.761	3.732	189.240	173.0±8.7
110 °C- Ni_5Ga_3	7.478	6.784	3.721	188.769	171.1±8.7
130 °C- Ni_5Ga_3	7.503	6.758	3.734	189.334	199.2±8.7
150 °C- Ni_5Ga_3	7.528	6.735	3.744	189.825	208.9±8.7
Ni_5Ga_3 in ref[112]	7.530	6.720	3.770	190.768	-

4.3.2.2 Morphologies of Ni_5Ga_3 samples

The morphologies of as-prepared Ni_5Ga_3 catalysts were shown in Fig. 16(a-d). As shown, the typical layered structure disappeared, with acute agglomeration of catalyst particles, which was attributed to a high temperature (700 °C) in the reduction process. The particle size of 110 °C-Ni_5Ga_3 sample was estimated by HIM, and the result indicated that the particle size was around 200 nm, which was in accordance with the particle size calculation based on the PXRD pattern. Interestingly, the individual particle of 110 °C-Ni_5Ga_3 sample in HIM images maintained the disk-like shape, inherited from parent HTlc precursor, as shown in Fig. 17(a). The elemental distribution was investigated for all the samples by TEM-mapping Fig. 18 (a-d), and it was clearly observed that the nickel and gallium were uniformly dispersed within catalysts, despite of severe agglomeration due to the high-temperature treatment resulting in larger grain size of Ni_5Ga_3 as well as low

specific surface area due to the destruction of layered structure. And the BET surface area for all as-prepared catalysts were under 10 m^2/g, as can be seen in Table 8.

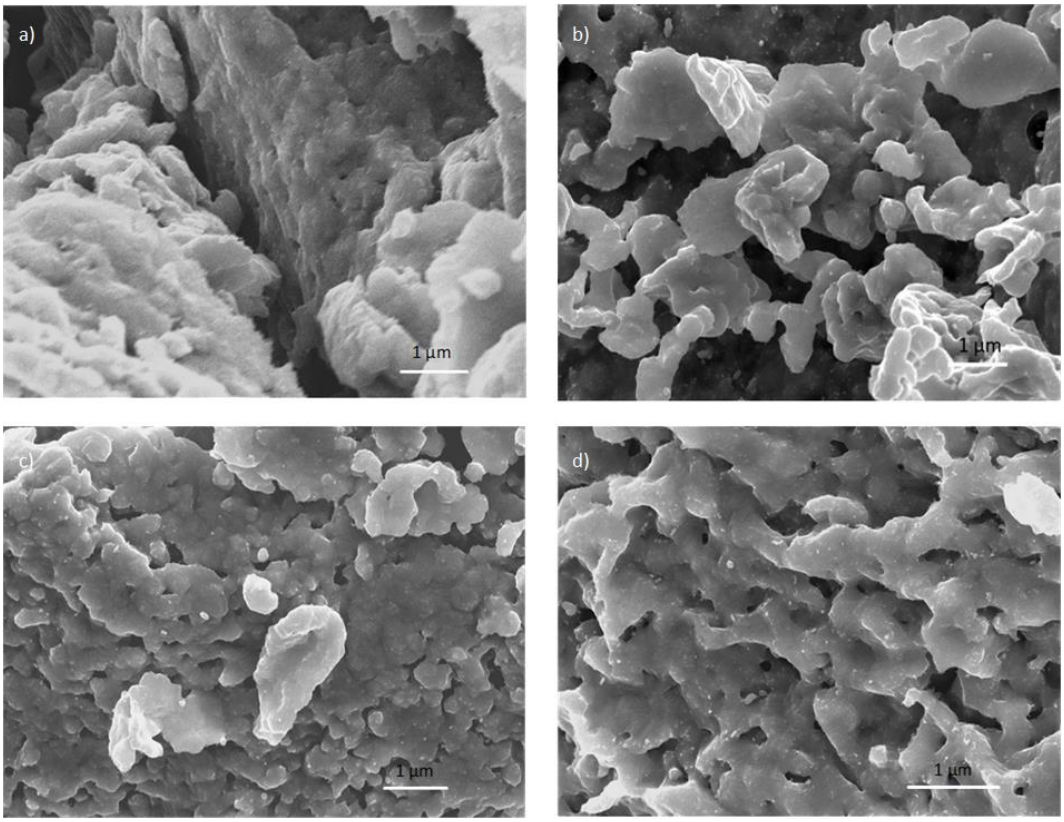

Fig. 16 SEM images of x-Ni_5Ga_3

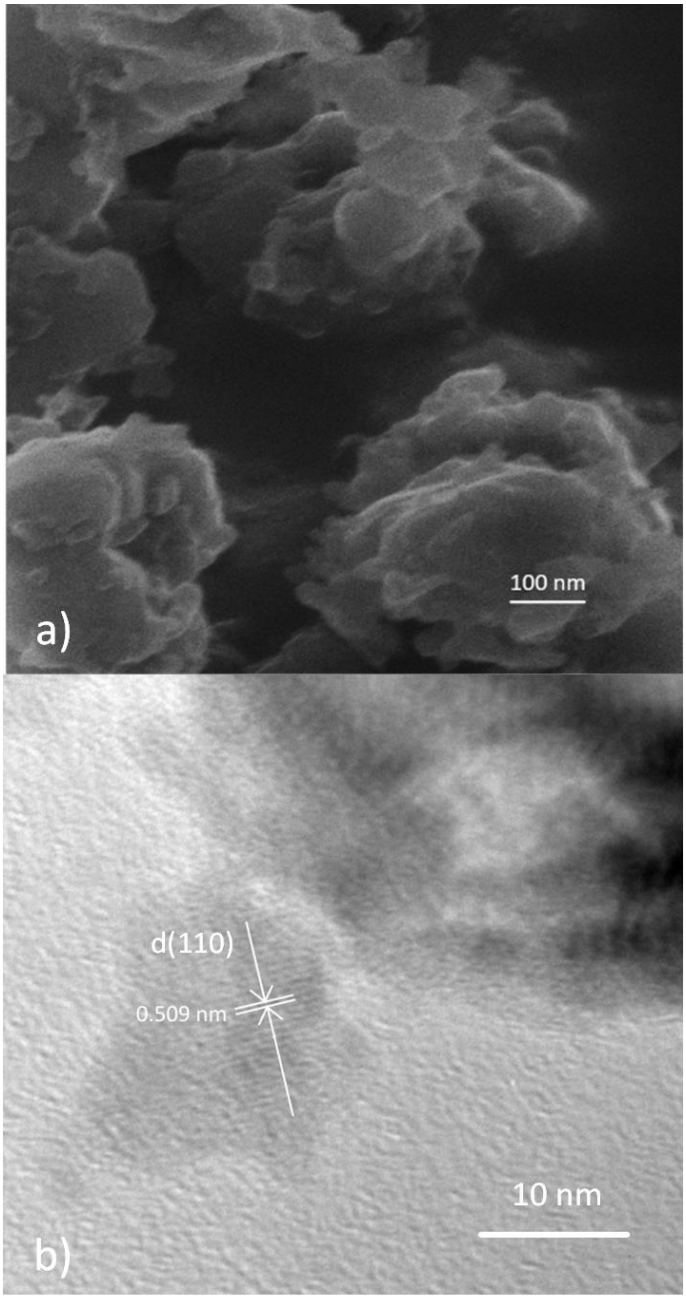

Fig. 17 a) HIM and b) HRTEM images of 110 °C-Ni_5Ga_3 sample

The lattice fringes of 110 °C-Ni_5Ga_3 samples were clearly observed with a d spacing of 0.509 nm, which corresponded to the spacing of (110) surface in Ni_5Ga_3 crystal unit, as can be seen in Fig. 17(b).

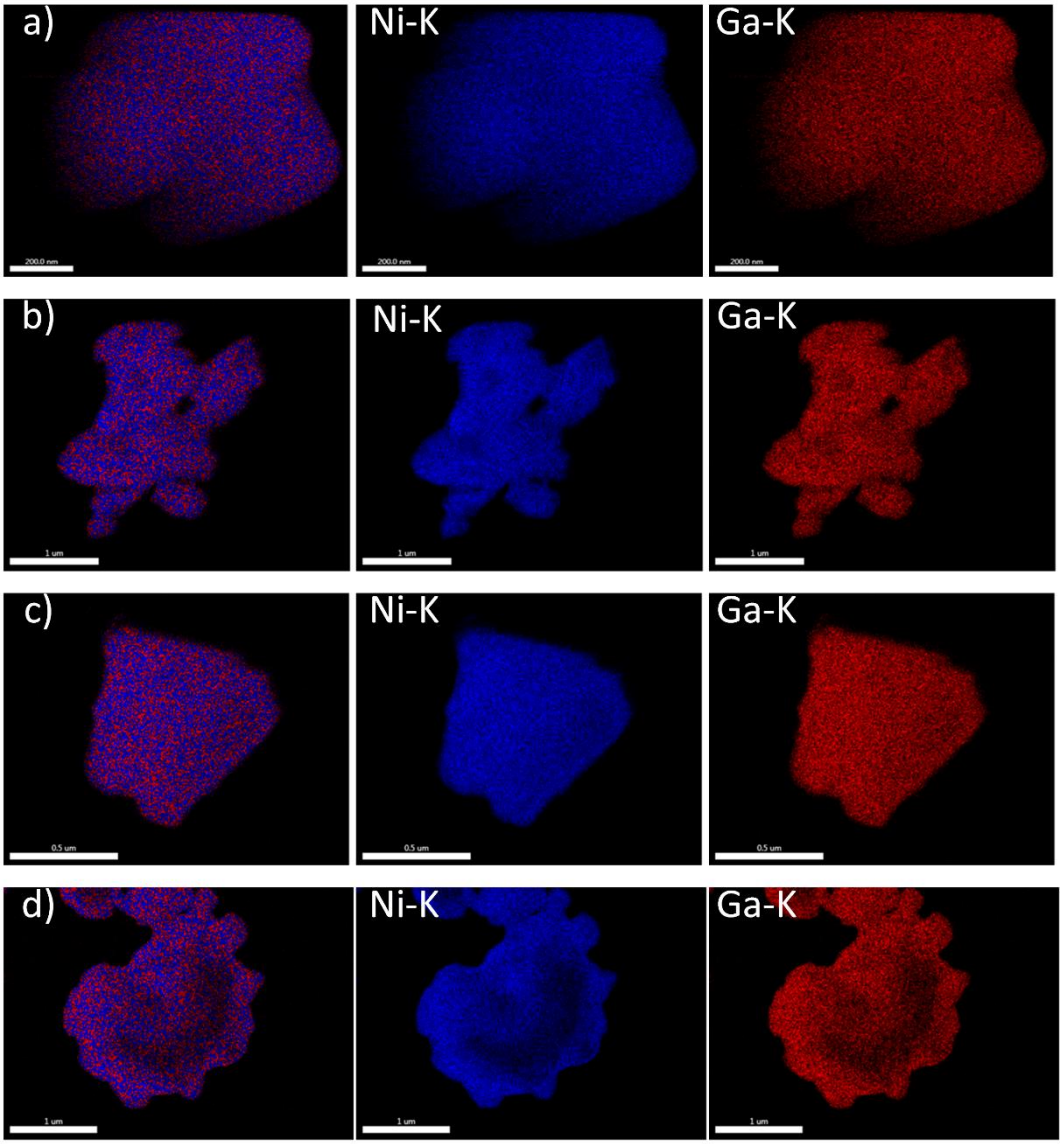

Fig. 18 Elemental distribution of a) 90 °C-HTlc precursor, b) 110 °C-HTlc precursor, c) 130 °C-HTlc precursor, d) 150 °C-HTlc precursor

4.3.2.3 Local structure of Ni_5Ga_3

The electron state and structural information for all catalysts were obtained by XAS and are shown in Fig. 19. It could be clearly observed that 90 °C-Ni_5Ga_3 exhibited a totally different oscillating trend in Ga K-edge in X-ray absorption near edge structure (XANES) and fine structure in the extended X-ray absorption fine structure (EXAFS) spectra, compared with other three samples and is in accordance with reference material (Ga_2O_3) with the adsorption edge. The Fourier transform spectra plot (Fig. 20) in R space revealed that 90 °C-Ni_5Ga_3 sample consisted of a mixture of Ga oxides and Ga-Ni alloy, suggesting that the Ga element in the sample was

partially oxidized. Considering that all the samples were prepared under similar conditions before the experiment, 90 °C-Ni_5Ga_3 was more easily oxidized compared with other samples, indicating an instability of Ni_5Ga_3 crystal prepared at lower hydrothermal temperature. Hence, the impact of HTlc precursor on Ni_5Ga_3 catalysts was discussed based on 110 °C-Ni_5Ga_3, 130 °C- Ni_5Ga_3 and 150 °C- Ni_5Ga_3 because of its stable HTlc precursor and Ni_5Ga_3 crystal structure.

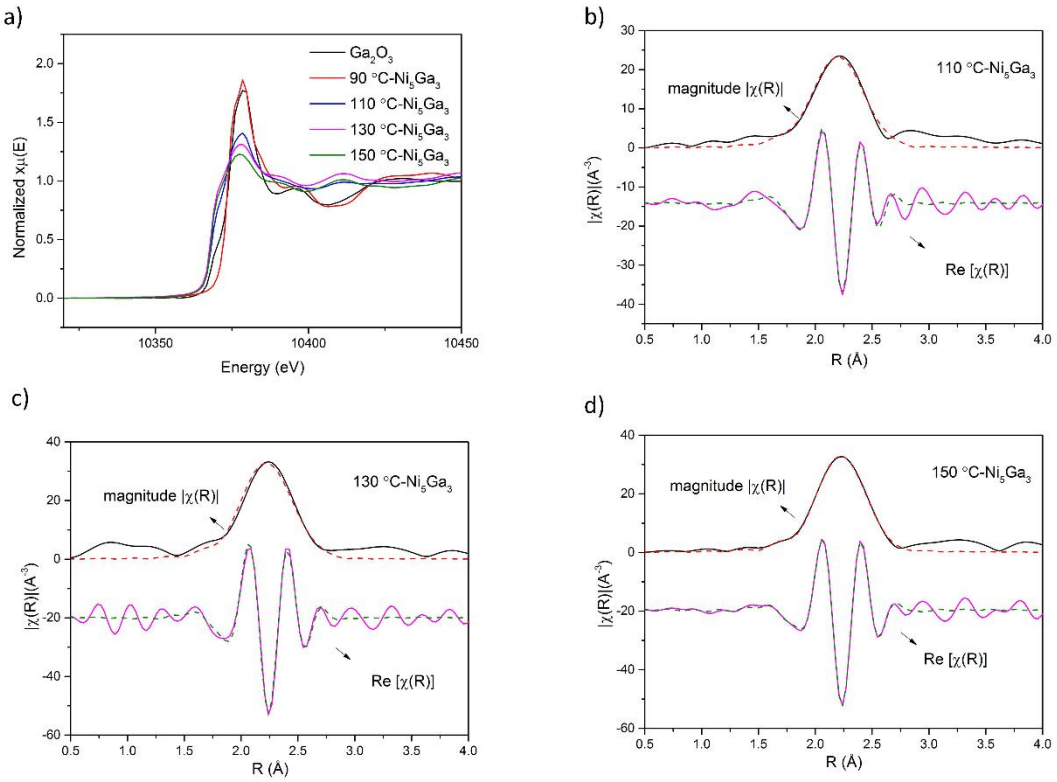

Fig. 19 a) Ga K-edge EXFAS spectra of x-Ni5Ga3 and b) Fourier transform (k2-weighted, Δk=4-14 Å-1) plotting in R space of 110 °C-Ni5Ga3, c) 130 °C- Ni5Ga3, d) 150 °C- Ni5Ga3 (solid line - experimental curve and dash line - fitting curve.

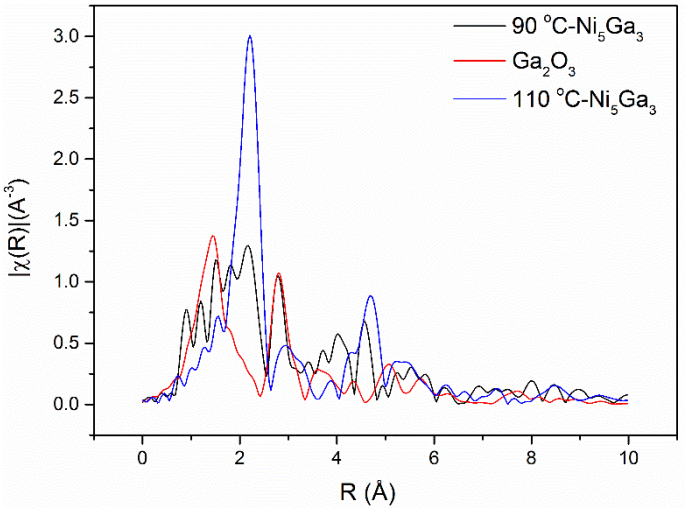

Fig. 20 Fourier transforms plotting in R space of 90 °C-Ni_5Ga_3 and 110 °C-Ni_5Ga_3

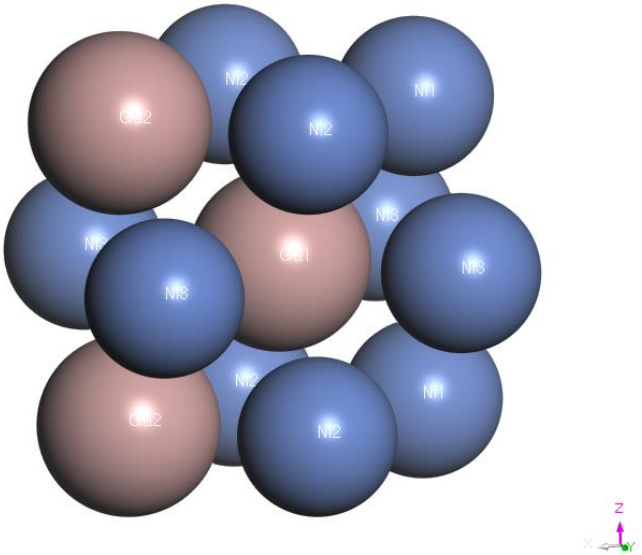

Fig. 21 Frist coordination shell around center gallium, with 12 nickel atoms surrounded (bule-Nickel, red-Gallium)

The corresponding Fourier transforms plotting in R space for the EXAFS region were fitted within the first coordination shell and subsequently plotted in Fig. 21. One centre gallium atom (Ga_1) was surrounded by 12 nickel atoms with three nickel types and 2 gallium atoms, namely Ni_1, Ni_2, Ni_3 and Ga_2, respectively. The fitting simulated different reflection pathways between nickel and gallium atoms (dash line), and it was in agreement with the experimental curve (solid line) in Fig. 19 (b-d) within 1 Å and 2.8 Å. The bond distance was listed in Table 6, and the shortest bond distance (e.g. Ni-Ga and Ga-Ga bond) was observed in 110°C-Ni_5Ga_3, and the bond distance increased with an increasing HTlc precursor synthesis

temperature. These results corresponded to the PXRD calculation that 110°C-Ni_5Ga_3 exhibited a smaller cell volume.

The Debye-Waller factor (σ^2), which described the thermal disorder generated from bond vibrations[113], was calculated and summarized in Table 6. A decreasing σ^2 was observed as hydrothermal temperature for HTlc precursor synthesis increased, indicating that 150°C-Ni_5Ga_3 exhibited a higher stability. In addition, the Debye-Waller factor was fairly small, indicating that all reduced samples were well crystallized[114].

Summarily, 110ºC-Ni_5Ga_3 was expected to exhibit a higher catalytic performance for CO_2 hydrogenation to methanol due to the smallest grain size and a relatively Ni_5Ga_3 crystal stability.

Table 6 Structural parameters in EXAFS for x-Ni_5Ga_3

	Bond type	110 °C-Ni_5Ga_3	130 °C-Ni_5Ga_3	150 °C-Ni_5Ga_3
R (Å)	Ga_1-Ni_1	2.521	2.532	2.537
	Ga_1-Ni_2	2.520	2.527	2.526
	Ga_1-Ni_3	2.430	2.437	2.458
	Ga_1-Ga_2	2.789	2.814	2.816
σ^2 (10^{-3} Å^2)		3.71	2.62	0.99

4.3.3 The reducibility of the catalysts

The reducibility of the as-prepared samples was investigated by TPR measurements (Fig 22). 90 °C-HTlc sample exhibited four strong and major peaks within the entire temperature range. Since nickel was more easily reduced compared with gallium, the first two peaks located at lower temperatures (e.g. below 550 °C) represented the reduction of nickel oxides, while the other two peaks, over 600 °C, were attributed to the step-wide reduction of gallium oxides[115]. The first nickel oxide reduction peak was denoted as Ni_1, which represented the reduction of isolated or bulk NiO, while the other one, denoted as Ni_2, was attributed to the reduction of NiO interacted with surrounding metal oxides (NiO and Ga_2O_3), which required a higher reduction temperature due to a higher binding energy[116]. However, it could be observed that Ni_1 peak experienced a sharp decrease in the other three samples, demonstrating an increase in nickel oxide interaction with other metals. The result indicated 90 °C-HTlc exhibited an incomplete HTlc precursor structure

with a poor interaction between NiO and other metal oxides, while a stable HTlc structure was observed at elevated hydrothermal temperature.

The step-reduction of Ga_2O_3 was facilitated by the metallic nickel, as a result, the peak overlapped with Ni_2 was the reduction of Ga_2O_3 which interacted neighbouring NiO. Furthermore, the reduction temperature of Ga_1 in 110 °C-HTlc, 130 °C-HTlc and 150 °C-HTlc was lower than that of 90 °C-HTlc due to a closer interaction in HTlc precursor, facilitating reduction of Ga alloyed with Ni, resulting in a more complete HTlc structure at high hydrothermal temperature. However, the Ga_1 and Ga_2 shifted to a higher reduction temperature in the case of 110 °C-150 °C-HTlc samples, suggesting that the reduction of gallium is constrained in the HTlc precursor framework, and too strong interaction in HTlc structure would hinder the reduction of Ga_2O_3.

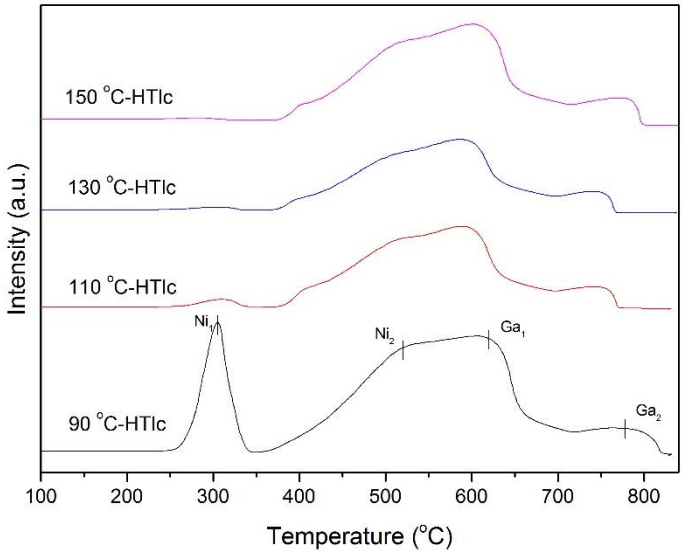

Fig. 22 TPR patterns for x-HTlc precursors

4.3.4 Proposed pathways for Ni_5Ga_3 formation from its HTlc precursor

As discussed earlier we can conclude that a stable and complete HTlc structure can be synthesized at elevated hydrothermal reaction temperatures. The stable HTlc possessed a “compacter” structure, where the Ni and Ga interacted closely. The bonds between Ni^{2+}/Ga^{3+} and Ni^{2+}/Ni^{2+} were then broken, and the corresponding reduced Ni_5Ga_3 was crystallized from the parent HTlc precursor via a high-temperature H_2 reduction, and the new reconstructed Ni-Ga bond length gradually increased with the precursor hydrothermal temperature, as proved by EXAFS analysis. However, since 90°C-Ni_5Ga_3 sample was derived from incomplete

HTlc precursor, it was found to be unstable and could be oxidized easily. Thus, it can be concluded that a stable HTlc structure assisted in stabilizing and constructing the bond between Ni and Ga. However, the grain size of as-prepared Ni_5Ga_3 also increased with a larger HTlc precursor particle size and the high-temperature reduction further accelerating the agglomeration, which resulted in a negative effect on the catalytic performance.

The formation pathway of Ni_5Ga_3 from the HTlc precursor is proposed in Fig. 23. The parent HTlc precursor was first synthesized, followed by the removal of interlayer water and anions (carbonates and hydroxides) during the H_2 reduction process, leading to the stacking of layers. H_2 was introduced into the HTlc system, and then the closely spaced nickel and gallium oxides were reduced slowly, subsequently, the Ni-Ga bond in HTlc precursor was destroyed, rearranged and reconstructed to form Ni-Ga bond in Ni_5Ga_3 crystal structure. A stable HTlc structure with a closer interaction between nickel and gallium were proposed to facilitate the formation of Ni_5Ga_3 bimetallic catalysts.

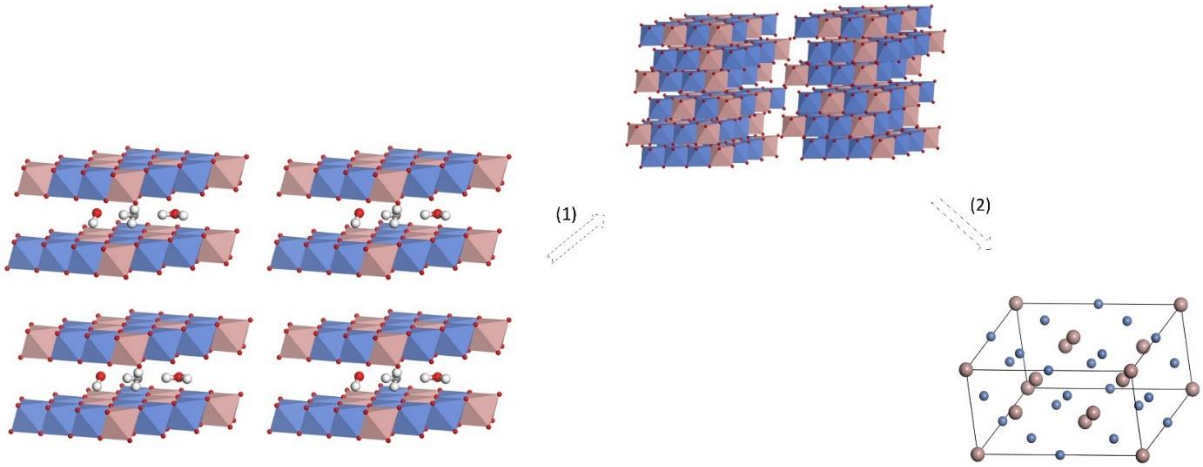

Fig. 23 The proposed pathway for Ni_5Ga_3 prepared from HTlc structure: (1) layers adjacent to each other; (2) assembly a template for Ni_5Ga_3

To further understand the impact of HTlc precursor on the formation of Ni_5Ga_3 bimetallic catalyst, Ni-Ga alloy prepared by the conventional impregnation method was investigated. The obtained PXRD patterns of the samples were shown in Fig. 24. The peaks, located at 2θ=43.6°, 50.8° and 74.8° corresponded to Ni_3Ga (111), (200) and (220) planes, while diffraction patterns of Ni_5Ga_3 were mentioned in section 4.3.1.1 with six typical reflection peaks. The result indicated that Ni_5Ga_3 could only be synthesized at 65% nickel content and Ni_3Ga appeared to be a major

Ni-Ga alloy product below 65% nickel content. However, it was observed that Ni_5Ga_3 could be synthesized within a wide range, such as 50 %: 50 % to 65 %: 35 % nickel to gallium atomic ratio via HTlc as precursor method.

The HTlc precursor belonged to R3m space group, which acted as a three-dimensional template for the synthesis of Ni-Ga alloy, resulting in synthesis of Ni_5Ga_3, with Cmmm space group, and a larger cell volume as well as complex orthodromic structure. On the contrary, Ni_3Ga with a simple cubic crystal structure (Pm-3m space group) could be easily synthesized via impregnation method.

The results suggested that highly pure Ni_5Ga_3 could be preferentially synthesized by HTlc precursor instead of Ni_3Ga.

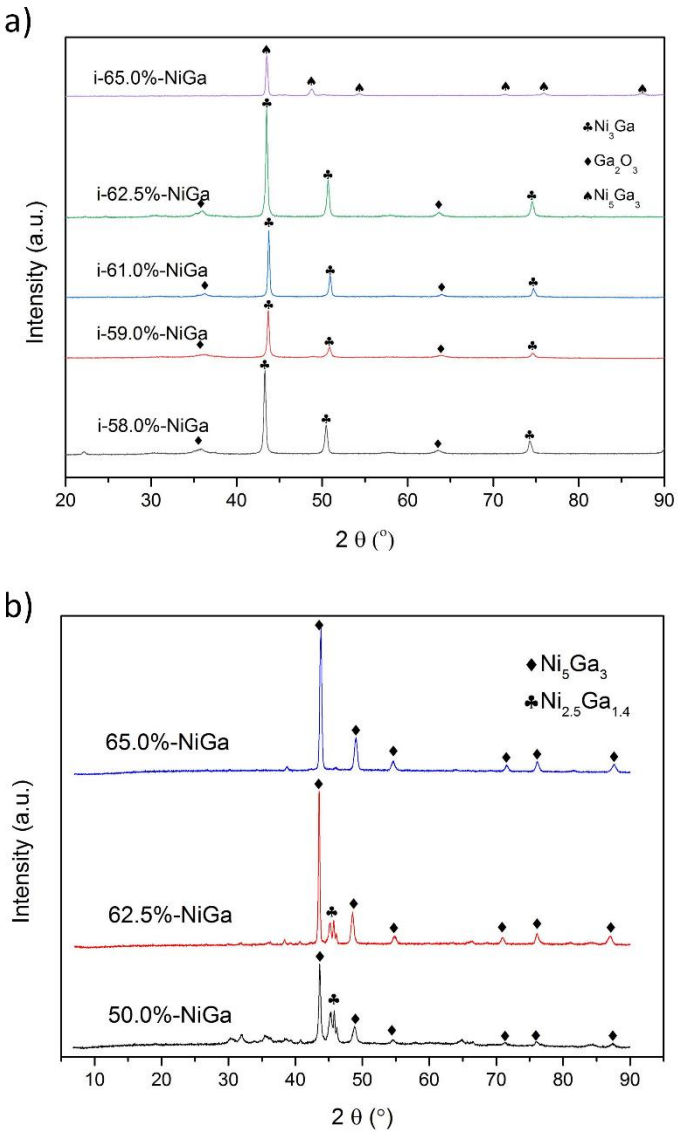

Fig. 24 Ni-Ga alloy prepared via a) impregnation method and b) HTlc precursor

4.3.5 Catalytic performance

To investigate catalytic characteristics of the bimetallic alloys prepared from a stable HTlc precursor structure, the prepared 110 °C-Ni_5Ga_3, 130 °C-Ni_5Ga_3 and 150 °C-Ni_5Ga_3 samples were tested for CO_2 hydrogenation to methanol in the temperature range between 200 and 300°C at 3.0 MPa with a space velocity of 373.3 mL g^{-1} h^{-1}. The CO_2 conversion correlated to the crystal size of Ni_5Ga_3 as shown in Fig. 25(a). The highest CO_2 conversion was observed in 110°C-Ni_5Ga_3, due to a relatively smaller particle size, which surpassed other samples within the entire temperature range (Fig 25(b). The catalytic performance decreased as the crystallized size increased. This result further emphasized that the grain size of highly pure Ni_5Ga_3 played a crucial role in reactivity for methanol synthesis. Due to the low CO_2 conversion, it is important to compare the catalytic properties between samples with different grain size rather than compare with commercial Cu-based catalysts. The methanol selectivity reached 100% methanol selectivity at 200 °C without the detection of CH_4 and CO in the products. As the temperature increased to 250 °C, rWGS competed with methanol synthesis reaction, and CO was the major by-product with traces of CH_4. Methanol selectivity further decreased to around 70% at 300 °C because CO_2 methanation participated in the reactions. The rWGS was thermodynamically favoured at elevated temperature due to the nature of endothermic reaction, and thus the methanol selectivity was gradually decreased with the increase of reaction temperature[117]. However, the parallel reactions, including methanol synthesis, rWGS, and CO_2 methanation contributed to a promoted CO_2 conversion. Overall high methanol selectivity was observed in the entire temperature range studied, compared with the conventional Cu-based catalyst, as can be seen from Table 7. Furthermore, the turnover frequency (TOF) was calculated accordingly, as shown in Table 8. The active sites were calculated from the measured BET surface area and consider one Ni_5Ga_3 crystal lattice as a basic active site. The result revealed that an enhanced TOF was observed, with a highest TOF of 0.57 s^{-1} at 200 °C in case of 150 °C-Ni_5Ga_3 sample.

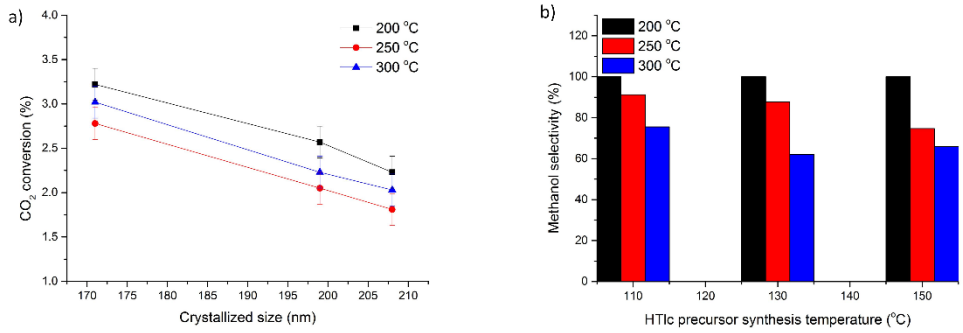

Fig. 25 a) CO_2 conversion in terms of crystallized size and b) methanol selectivity of 110 °C-Ni_5Ga_3, 130 °C-Ni_5Ga_3 and 150 °C-Ni_5Ga_3 catalysts synthesized (P=3.0 MPa, weight hourly space velocity =373.3 mL g^{-1} h^{-1})

Table 7 Catalytic performance of copper-based catalysts in reference

Catalysts	Reaction conditions			Catalytic Performance	
	Temperature (K)/ Pressure (Mpa)	Feed H_2/CO_2 ratio	Space velocity	CO_2 conversion (%)	Methanol Selectivity (%)
Cu-ZnO-ZrO_2[46]	473/3.0	3	4400 ($mLg^{-1}h^{-1}$)	6.2	66.9
Cu-Ga_2O_3--ZrO_2[118]	523/3.0	3.4	20000 (h^{-1})	1.3	74
Cu-ZrO_2[119]	553/3.0	3	7200 ($mLg^{-1}h^{-1}$)	12	32
Cu-ZnO[120]	523/3.0	3	18000 (mL $g^{-1}h^{-1}$)	2.3	100
Cu-Zn-Ga[121]	543/3.0	3	3000 (h^{-1})	15.9	29.7
Cu-Al[122]	523/2.9	5	100 ($mLmin^{-1}$)	N/A	54.91

The stability of 110 °C-Ni_5Ga_3 was tested by a time-on-stream (TOS) experiment. The CO_2 conversion remained almost constant for 160 hours, and no by-products such as CH_4 and CO were detected during the entire measurement, as can be seen in Fig. 26. The highly stable catalytic performance suggested that the catalyst resisted to deactivation and maintained a high stability under the reaction condition.

Table 8 BET surface area and turnover frequency (TOF) of 110 °C-Ni_5Ga_3, 130 °C-Ni_5Ga_3, and 150 °C-Ni_5Ga_3

Sample	BET surface area (m^2/g)	TOF (s^{-1})		
		200 °C	250 °C	300 °C
110 °C-Ni_5Ga_3	7.88	0.27	0.22	0.19
130 °C-Ni_5Ga_3	5.36	0.32	0.22	0.17
150 °C-Ni_5Ga_3	2.60	0.57	0.35	0.34

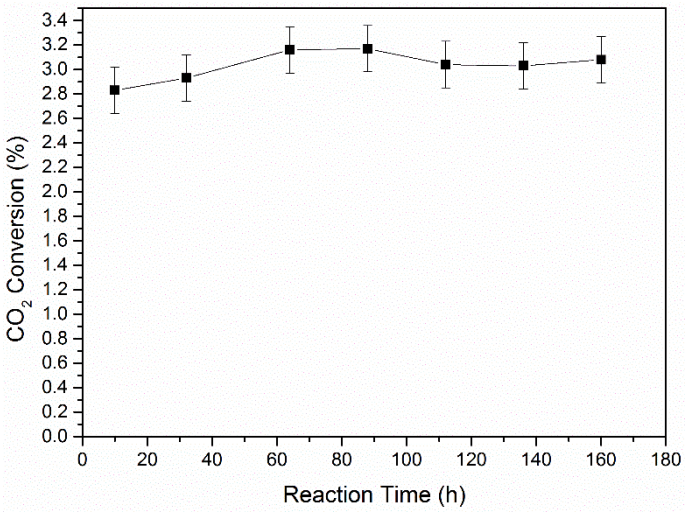

Fig. 26 Time-on-stream experiment for 110 °C-Ni_5Ga_3 under 200 °C, 30 bar

4.4 Conclusions

In this section, a highly pure Ni_5Ga_3 was synthesized via a Ni-Ga type HTlc precursor, and the precursor was found to play a vital role in the formation of Ni_5Ga_3.

Specifically, HTlc precursors with a nickel atomic percentage of 65 % balanced with gallium were prepared by a hydrothermal method between 90 °C and 150 °C, and the structure as well as stability of the as-prepared precipitate were determined with PXRD and thermogravimetric measurements, respectively. The HTlc precursor could not be synthesized at a temperature lower than 90 °C, and it was observed that the HTlc precursors were better crystallized and the structure became more stable and complete at elevated synthesis temperature (such as 150 °C). The particle size also expanded in both horizontal [110] and vertical [003] directions with the increasing hydrothermal temperature. The corresponding Ni_5Ga_3 catalysts were reduced by H_2 under 700 °C. The bond distance between Ni-Ga was measured by XAS, and the thus-obtained Ni_5Ga_3 unit cell tended to expand, and the crystal structure was perfectly constructed with an increasing precursor hydrothermal temperature. Ni_5Ga_3 was preferentially synthesized via HTlc precursor than the traditional impregnation method, as can be seen from the reduced Ni-Ga alloy PXRD, leading to a conclusion that three dimensional HTlc precursor template favoured the synthesis of highly pure Ni_5Ga_3. The catalytic performance was

measured for CO_2 hydrogenation to methanol. Sample 110 °C-Ni_5Ga_3 exhibited the highest CO_2 conversion, 100% methanol selectivity, and a TOF of 0.27 s^{-1} at 200 °C, 30 bar. A smallest crystal cell, grain size and relatively stable Ni_5Ga_3 structure contributed to an enhanced catalytic performance. Furthermore, time on stream studies revealed a high catalytic stability for 160 hours.

This Chapter was published as '**Men Y**, Fang X, Gu Q, et al. Synthesis of Ni_5Ga_3 catalyst by Hydrotalcite-like compound (HTlc) precursors for CO_2 hydrogenation to methanol. ***Appl Catal B Environ***. 2020;275(May):119067'.

Chapter 5 Influence of promoters (Mg, Zn and Zr) on Ni-Ga catalysts via hydrotalcite-like compounds (HTlc) precursors for CO_2 hydrogenation to methanol

5.1 Introduction

In the previous chapter, highly pure Ni_5Ga_3 was synthesized by a HTlc precursor. A highly stable HTlc precursor structure stabilized and facilitated the formation of Ni_5Ga_3. However, the large particle sizes derived from HTlc had a negative effect on the catalytic performance for CO_2 reduction to methanol because it exposed fewer active sites for effective catalysis. Thus, the key point was to decrease the particle size of the as-prepared Ni-Ga metal alloy by modification. Previous research reported that the introduction of some metal oxide, such as ZnO and ZrO_2, would enhance the overall catalytic performance, as discussed in Chapter 2. MgO was also considered as an effective promoter because the addition of Mg in Cu-based catalysts enhanced the formation of smaller particle sizes and a higher concentration of basic sites[123]. The metal oxide promoters could physically act as spacers between the active sites, and the strong interactions between active sites and promoters, such as the spillover effect, could greatly enhance the CO_2 conversion as well as methanol selectivity. As discussed before, the hydrothermal reaction facilitates the formation of uniformly dispersed particles, which will enhance the interactions of Ni-Ga alloy and promoters. Therefore, urea hydrolysis hydrothermal reaction was advantageous to prepare HTlc precursors.

In this study, metal oxide promoters, such as Mg, Zn and Zr, were introduced into the HTlc precursor. The PXRD measurement was initially carried out to investigate the as-prepared Ni-Ga-X (X= Mg, Zn and Zr) HTlc precursor and corresponding reduced Ni-Ga-X catalysts. The characterization could help point out if the Ni-Ga alloy phase was affected by the promoters. In addition, SEM-EDS, TEM, TG, H_2-TPR, CO_2-TPD and XPS techniques were employed to further examine structure and morphology of the synthesized Ni-Ga-X. The reducibility was investigated by synchrotron in-situ PXRD under H_2 gas flow. The catalytic properties were evaluated in a micro-reactor for the methanol synthesis reaction.

5.2 Methodologies

5.2.1 Catalysts preparation

HTlc precursors consisted of nickel, gallium and promoter (eg. magnesium, zinc or zirconium) and were prepared by a urea hydrothermal method. The as-prepared HTlc precursor was denoted as NGX-HTlc (X=Mg, Zn and Zr, respectively). To synthesize NGMg-HTlc as an example, $Ni(NO_3)_2.6H_2O$ (Sigma Aldrich), $Ga(NO_3)_3.9H_2O$ (Changsha Easchem Co., Limited), and $Mg(NO_3)_2.6H_2O$ (Sigma Aldrich) were dissolved in 100 ml distilled water with vigorous stirring. The Ni:Ga:Mg ratio in the solution equalled 61.8%:33.2%:5%, with an overall cationic concentration of 0.3 mol/L. Urea (Sigma Aldrich) was further added into the solution, and the amount of urea was equivalent to number of nitrates in the solution. The chemicals mentioned above were used without further purification. The as-prepared solution was well-mixed and subsequently transferred to a hydrothermal autoclave (Parr autoclave model 4843), kept at 110 °C for 4 hours with a stirring speed of 127 rpm. The precipitate was cooled down to room temperature, centrifuged and washed by de-ionized water three times, and dried at 90 °C overnight. NGZn-HTlc and NGZr-HTlc were prepared accordingly, with a Ni: Ga: Zn(Zr) ratio of 61.8%:33.2%:5%. NG-HTlc was synthesized by a similar procedure, with a Ni:Ga ratio of 65%:35%.

The dried cake of NGX-HTlc was collected, crushed and sieved (40-60 mesh size), and subsequently reduced in a sealed tube furnace by a 5% H_2/Ar mixed gas with a flowrate of 40 mL/min, kept at 700 °C for 6 hours, as described earlier in Chapter 3 section 3.2.1.2. The reduced Ni-Ga-X catalysts were denoted as NGX-redu. The reduced catalysts were immediately transferred to the micro-reactor before surface oxidation occurred.

5.3 Results and discussion

5.3.1 Textural and structural properties of the prepared materials

5.3.1.1 PXRD patterns and structural analysis of precursors and catalysts

The PXRD patterns of NGX-HTlc are shown in Fig. 27. The reflections of (00l) crystal structure, like (003), (006) and (009) at a low angle between 10° to 35° can be clearly observed. The symmetric peak indicated the formation of a typical layered structure in the as-prepared HTlc precursor. However, the signal to noise

ratio from NGX-HTlc samples was lower than that from x-HTlc precursors, indicating a lower degree of crystallisation compared to the as-prepared samples. Consequently, the (110) and (113) plane could hardly be distinguished due to poor crystallinity. Furthermore, the intensity of all peaks in NGZr-HTlc sample was lower compared to that in other samples. The reason was firstly ascribed to the formation of a smaller crystallite size in NGZr-HTlc sample, and secondly, to a larger distortion in the double layers, as Ga^{3+} is partially replaced by Zr^{4+} in the HTlc framework. The intensity of peaks in NGZn-HTlc and NGMg-HTlc exhibited a similar intensity to NG-HTlc, indicating the introduction of Zn and Mg into HTlc framework did not greatly influence the crystallite size and HTlc crystallinity.

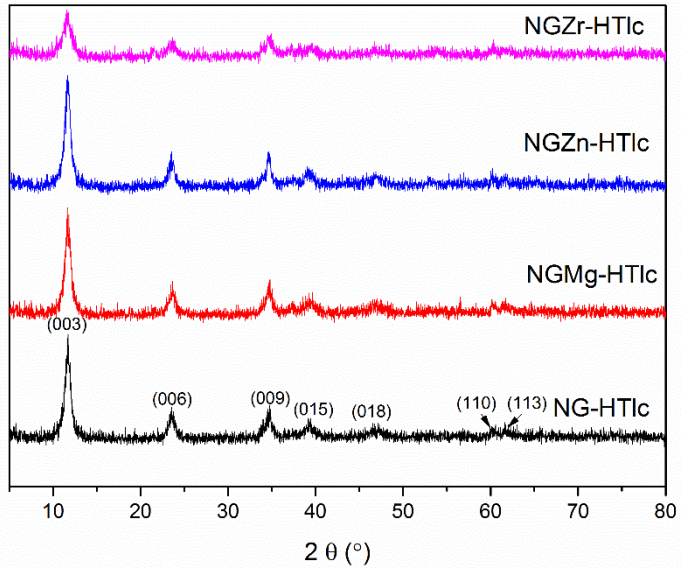

Fig. 27 PXRD patterns of NGX-HTlc precursor (X=Mg, Zn, Zr)

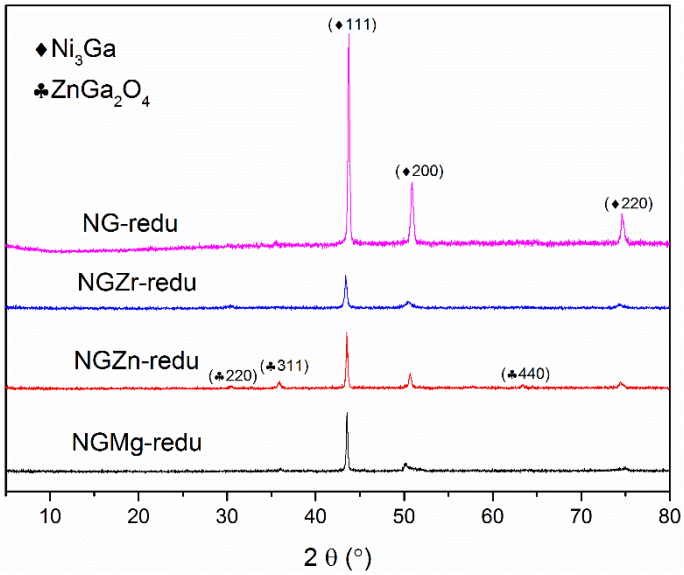

Fig. 28 PXRD patterns of NGX-redu (X=Mg, Zn, Zr)

The PXRD patterns of corresponding reduced Ni-Ga-X samples are shown in Fig. 28. It can be observed clearly that the layered structure has been destroyed, since the corresponding reflections, such as (003), (006) and (009), disappeared in the PXRD patterns of the reduced samples. The three main peaks located at a 2θ angle of 43.6°, 50.8° and 74.8° were matched to (111), (200) and (220) planes of the cubic intermetallic Ni_3Ga[124], respectively. The formation of Ni_3Ga instead of Ni_5Ga_3 from NGX-HTlc precursor was ascribed to an incomplete and unstable HTlc precursor due to the introduction of promoters, as well to the decreased hydrothermal reaction time from 16 hours to 4 hours (Chapter 4). The peak intensity in NG-redu (no promoter) sample was highest compared with other reduced samples, indicating that the introduction of promoters reduced the Ni-Ga alloy crystallite size. The smallest crystallite size was observed in NGZr-redu sample, which resulted from the decreased size of NGZr-HTlc precursor. It was also worth mentioning that an impurity appeared in the NGZn-redu sample, with (220), (311) and (440) plane corresponding to $ZnGa_2O_4$ spinel structure, while PXRD patterns of the other samples did not reveal apparent impurity peaks after the modification with Mg or Zr.

5.3.1.2 Surface analysis of precursors and catalysts

The BET surface area was measured for both NGX-HTlc and NGX-redu catalysts, as can be seen from Table 9. Generally, the BET surface area of reduced catalysts depended on the corresponding HTlc precursor. For example, the NGZr-HTlc precursor with the highest surface area resulted in NGZr-redu catalyst with the highest specific area, further confirming the fact that the precursor played a vital role in the formation of the corresponding reduced catalyst. Also, it could be observed that the reduced sample exhibited 10 times lower BET surface area as compared with their parent HTlc precursor. The reason was ascribed to an agglomeration due to the high-temperature reduction. The N_2 adsorption-desorption isotherms for all precursor samples are presented in Fig. 29, and the pore volume was calculated based on the BJH model. In summary, the introduction of promoters in Ni-Ga-X system resulted in a slight change in pore volume because the Ni atom was partially replaced by additional elements (X). The pore volume in NGZn-HTlc was largest, followed by NG-HTlc and NGMg-HTlc, respectively. The change in pore volume was ascribed to the fact that the incorporation of additional element with a larger ionic radius contributed to a smaller pore volume (r_{Zn2+}=0.74

Å; r_{Ni2+}=0.69 Å; r_{Mg2+}=0.65 Å). It was also worth reporting that NGZr-HTlc exhibited the largest pore volume, which was due to a distorted and poorly crystallized layered structure.

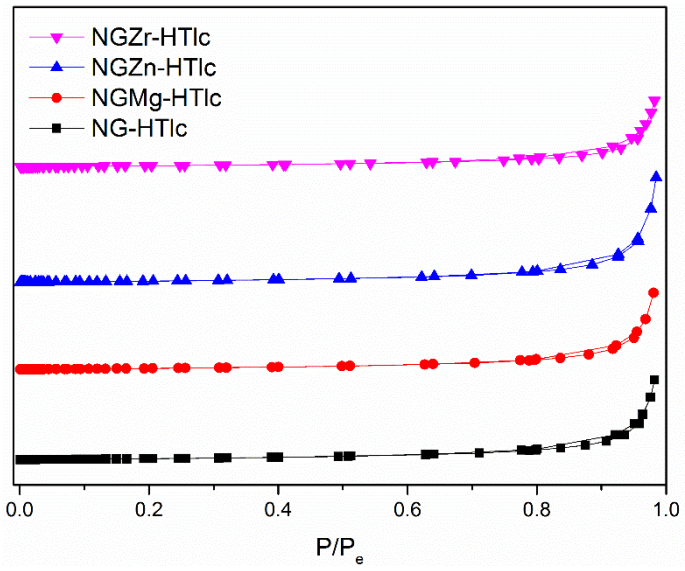

Fig. 29 N_2 adsorption-desorption isotherms for NGX-HTlc samples

Table 9 BET surface area of NGX-HTlc precursors and NGX-redu catalysts

Samples	BET (m^2/g)/Vp (cm^3/g)	
	HTlc precursor	Reduced sample
NG	194.4/0.217	6.8/-
NGMg	197.8/0.204	13.1/-
NGZn	191.0/0.176	10.2/-
NGZr	215.5/0.271	22.5/-

5.3.1.3 Thermal stability of precursors

The thermal stability of NGX-HTlc precursor was investigated by thermal decomposition. Basically, all samples exhibited a similar weight loss step (Fig 30). The first weight loss peak, located between 100 °C and 200 °C was ascribed to the removal of physically adsorbed water between the interlayers, followed by a simultaneous weight loss of carbonates and hydroxides as the temperature increased to around 300 °C. The weight loss could barely be observed as

temperature increased above 500 °C, suggesting that the typical layered structure was completely decomposed to metal oxides at elevated temperature.

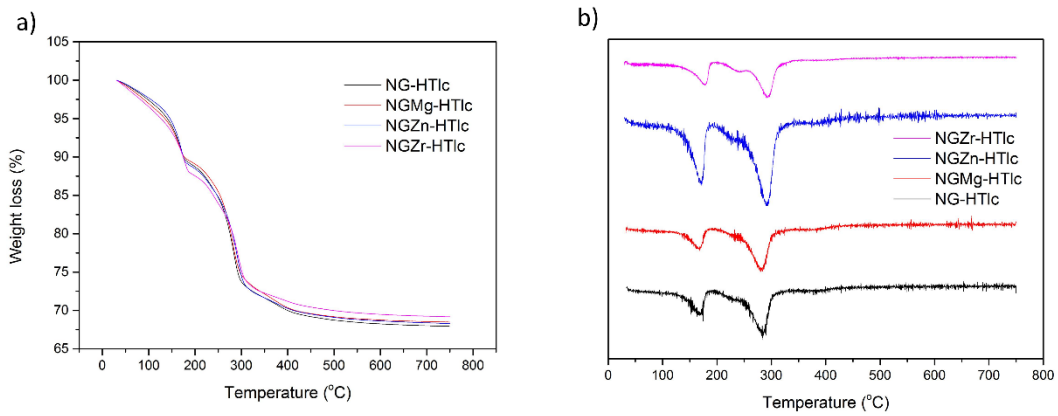

Fig. 30 Weight loss with temperature for NGX-HTlc precursors by (a) TGA and (b) DTG curves

5.3.1.4 Morphologies of precursors and catalysts

The SEM images of NGX-HTlc precursors are shown in Fig. 31 (a), (c) and (e). As can be observed from the images, these exhibited an agglomerated layer-morphology. Even though a homogenous urea hydrothermal method was employed to synthesize the HTlc precursor, a monodispersed plate-like morphology did not appear, as was reported earlier in Chapter 4 during the preparation of HTlc precursor for Ni_5Ga_3 formation. The reason was ascribed to shorter hydrothermal reaction time, which, specifically, decreased from 16 hours to 4 hours. In addition, it could also be observed from the images that the NGZr-HTlc was poorly crystallized, with a vague edge and a smaller particle size, compared with other samples, suggesting an obvious decrease in grain size especially after the introduction of Zr^{4+} in as-prepared HTlc precursor.

The SEM images of corresponding reduced catalysts were reported in Fig. 31 (b), (d) and (f). It could be clearly observed that the thin layers were completed decomposed into a cracked plate-like structure. Agglomeration was observed in all reduced samples, which was ascribed to a high-temperature reduction. Such morphology resulted in a decreased BET surface area as well as non-porosity in reduced samples. Furthermore, similar results could be obtained in Chapter 4, that

an incomplete HTlc precursor structure, such as NGZr-HTlc, with limited size growth, contributed to a decrease of grain size. As a result, NGZr-redu exhibited the smallest grain size among all the reduced catalysts. More detailed images by HRTEM described the morphology of NGZr-redu sample as shown in Fig. 32, and the average particle size was observed to be around 25 nm.

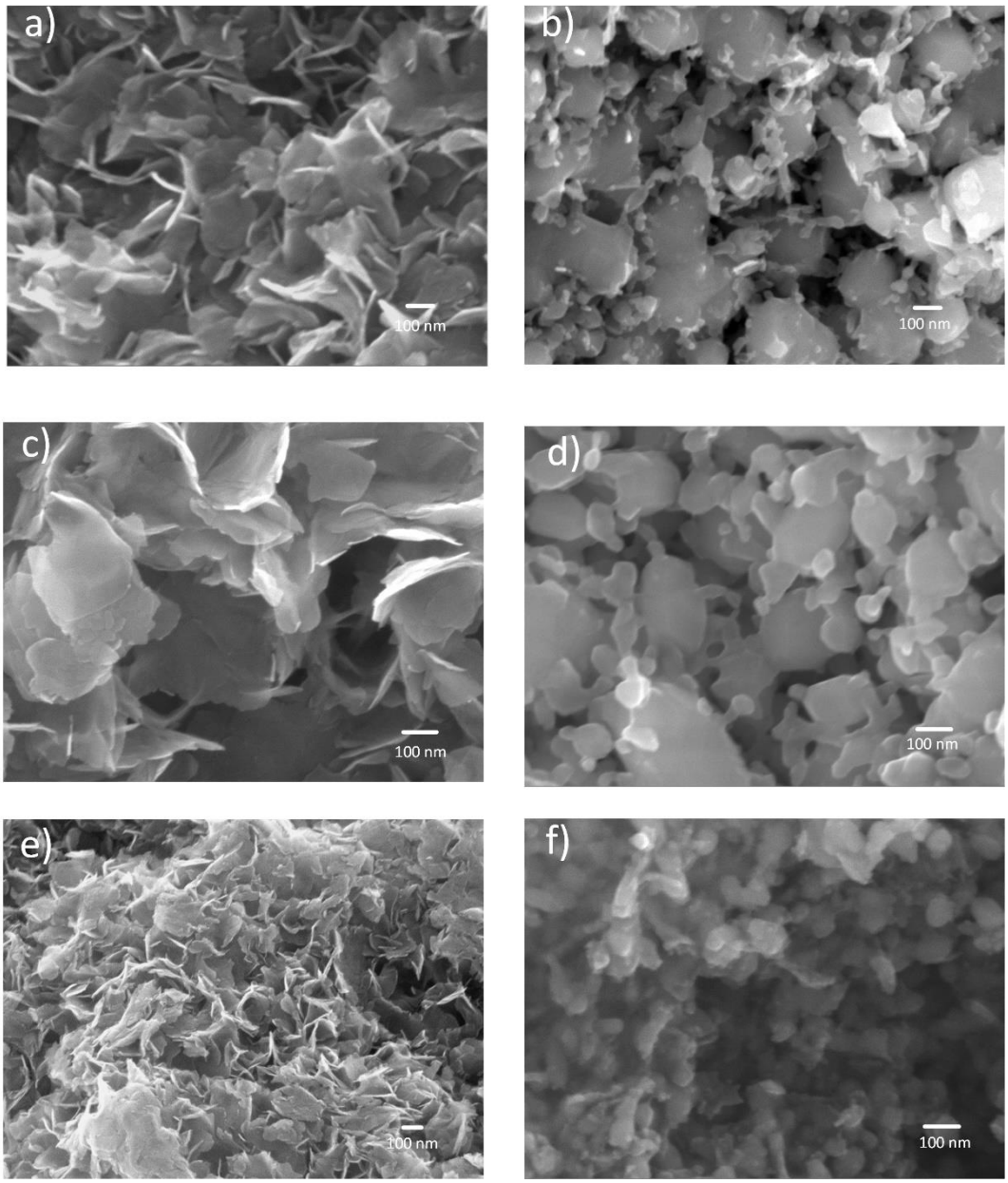

Fig. 31 SEM of a) NGMg-HTlc; b) NGMg-redu; c) NGZn-HTlc; d) NGZn-redu; e) NGZr-HTlc and f) NGZr-redu samples

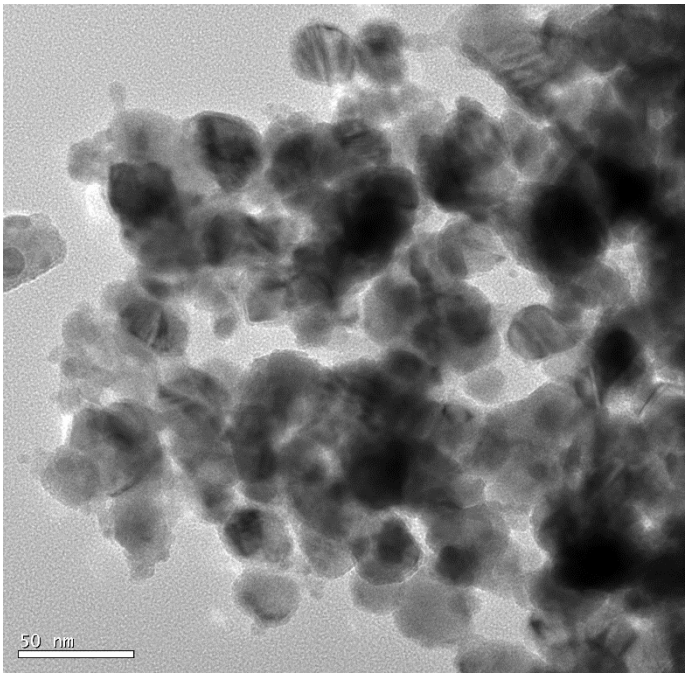

Fig. 32 TEM image of NGZr-redu sample

5.3.1.5 Elemental analysis of the corresponding catalysts

The elemental composition of NGX-HTlc precursors was first measured by SEM-EDS, and the results are summarized in Table 10. The measured elemental composition was roughly in accordance with the reagents input molar ratio for NGZn-HTlc and NGZr-HTlc. However, the magnesium concentration was below the detection limit, and thus only nickel and gallium could be detected in NGMg-HTlc, which indicated that $Mg(NO_3)_2$ was not fully precipitated into the HTlc precursor framework during the urea hydrothermal synthesis. Typically Mg^{2+} precipitates at approximate pH of 9.5[125], which was higher than that of Zn^{2+} and Zr^{4+}, which began to be precipitate at around 5[126] and 4[127], respectively. However, the pH equalled to around 7.5, measured after the urea hydrothermal reaction, which was lower than the precipitation pH range for Mg^{2+}. The residual Mg^{2+} amount was further detected by the ICP technique, and it accounted for about 0.5 wt%.

Table 10 Chemical composition in NGX-HTlc

Sample	At%(Ni: Ga:X)
NGZn-HTlc	60.7:32.8:6.5
NGZr-HTlc	60.1:33.9:5.9
NGMg-HTlc	60.3:35.8

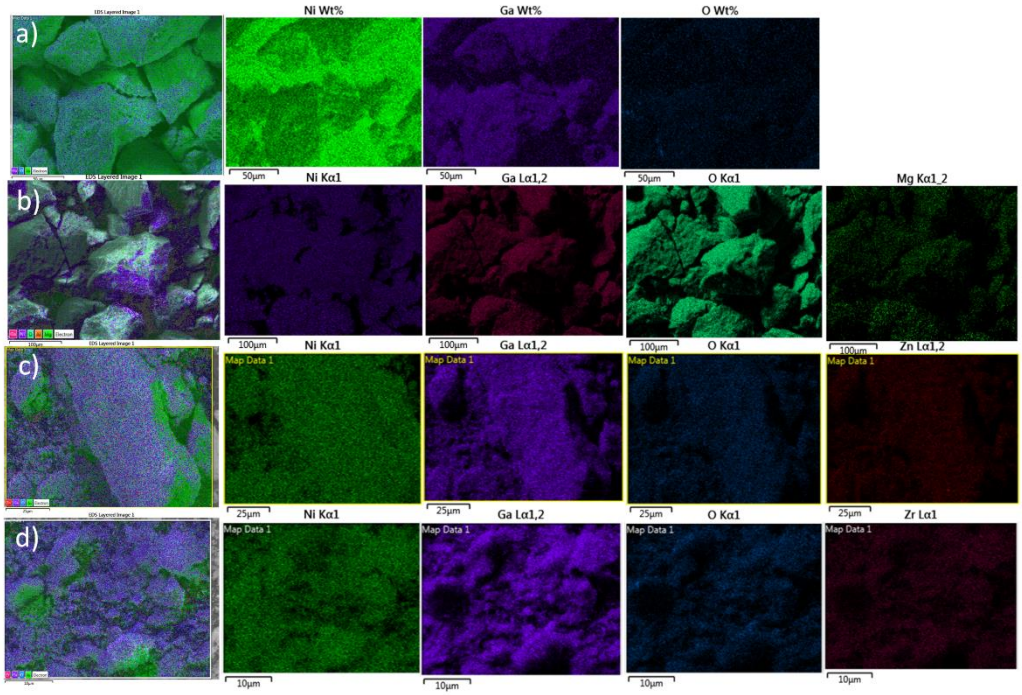

Fig. 33 SEM-mapping of the samples: a) NG-redu, b)NGMg-redu, c)NGZn-redu and d) NGZr-redu

The elemental distribution of NGX-redu catalysts was measured by SEM-EDS mapping, and are displayed in Fig. 33. Firstly, it could be observed that oxygen is present in all samples, indicating an incomplete reduction despite a high temperature. However, the oxygen concentration in NG-redu was lower than that in NGX-redu samples. The reason could be ascribed to the fact that promoters existed as metal oxides, which brought oxygen in the catalytic system. The oxygen was mostly bonded to gallium, indicating that some gallium was more difficult to be reduced, and partial gallium oxides existed as an amorphous form presented in the corresponding samples. Additionally, the oxygen was bonded closely to the

promoters, further suggesting that the Mg, Zn and Zr presented as metal oxides were uniformly dispersed in reduced catalysts. A strong interaction between the active component (Ni-Ga alloy) and promoters would possibly contribute to an enhanced catalytic performance.

A detailed elemental distribution study for NGZr-redu sample was investigated by HRTEM-mapping scan, shown in Fig. 34. The elemental distribution of Ni, Ga exhibited a considerably uniform dispersion around the catalyst particle, whereas Zr appeared mostly on the edge of the particle plate. If the TEM-mapping of NGZr-redu was compared with the Ni_5Ga_3 mapping prepared from 110 °C-HTlc in Section 4.3.2.2, it could be revealed that the introduction of Zr considerably decreased the average particle size of the reduced sample. This was ascribed to a distortion in as-prepared HTlc precursor due to incorporation of Zr, and thus the catalyst particles were segregated and isolated, contributing to the formation of smaller particles during the reduction process.

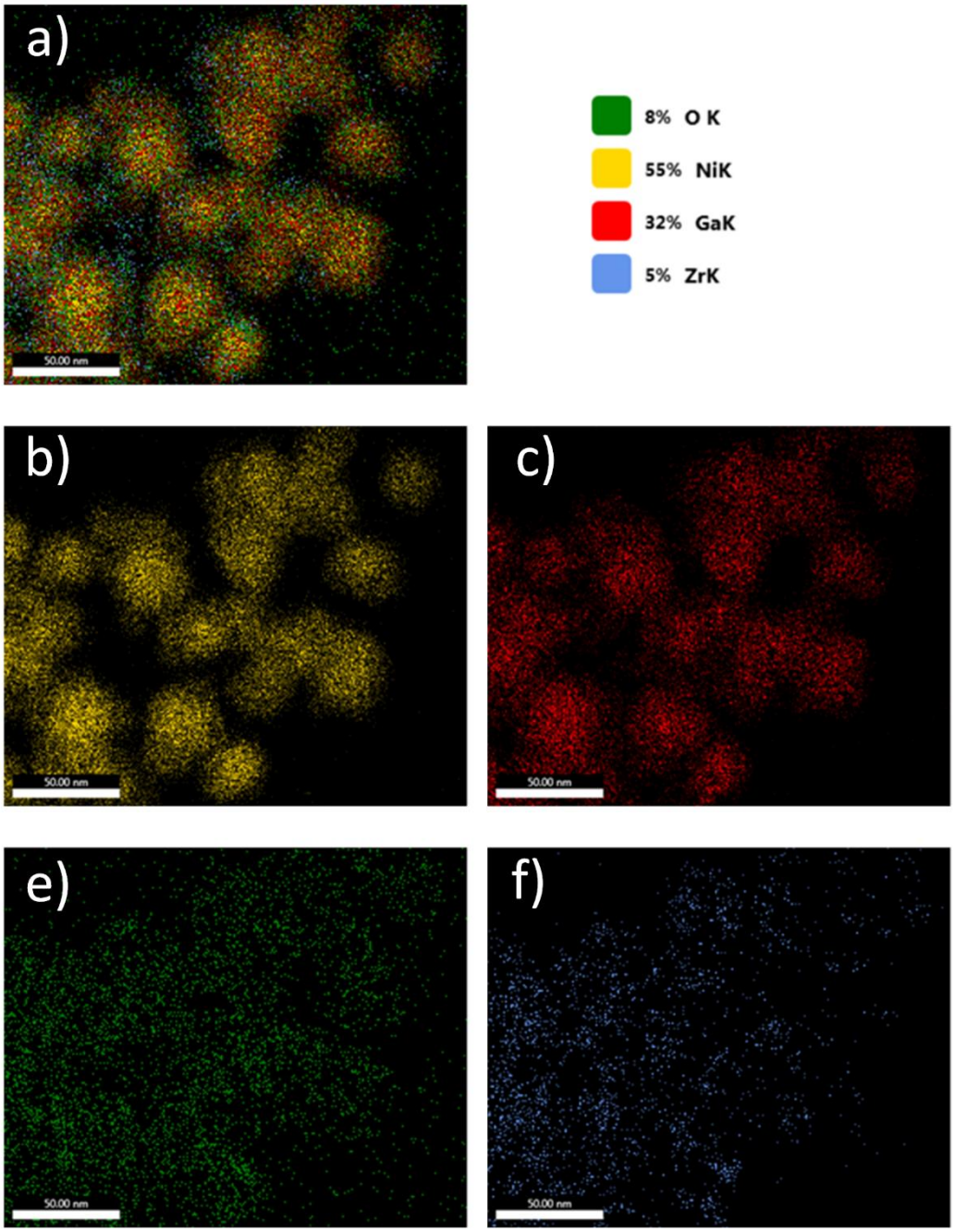

Fig. 34 TEM-Mapping of a) overall overlapping elemental distribution, b) elemental maps of O, 3) Ni, 4) Ga and 5) Zr for NGZr-redu sample in STEM images

5.3.2 The reducibility of NGX-HTlc precursors

The reducibility of NGX-HTlc precursor was shown in Fig. 35. Four major reduction peaks were observed in TPR profiles for all samples. The first peak located below 300 °C represented the reduction of isolated nickel oxides since bulk NiO was more easily reduced from HTlc structure without interaction with other elements, which was denoted as Ni_1 peak. As can be observed, the NGMg-HTlc exhibited a similar

Ni_1 peak profile with reference to NG-HTlc material, since a small amount Mg had a limited influence on the overall H_2 reduction pattern. The Ni_1 peak area decreased in NGZn-HTlc because of an increased interaction between nickel and other elemental oxides, such as $ZnGa_2O_4$ and Ga_2O_3, in HTlc precursor during H_2 reduction. The Ni_1 peak area was further decreased in NGZr-HTlc, indicating that the interaction between Ni and Zr was the strongest. As discussed earlier, ZrO_2 acts as a spacer and “apron” to help segregate the nickel-gallium alloy, where Ni and Zr interacted closely, and thus decreased the amount of isolated NiO in NGZr-HTlc.

The second reduction peak was assigned to the reduction of other nickel oxides, such as NiO interacted with promoters, and was denoted as Ni_2. Since the reduction of Ga_2O_3 was facilitated by the metallic nickel, the last two peaks belonged to the step reduction of Ga_2O_3. Ga_1 represented the Ga_2O_3 located near metallic nickel, while Ga_2 appeared above 700 °C represented a strong interaction between Ga_2O_3 and promoters or other remaining metal oxides. Additionally, Ga_2 peak appeared to have a tail, in all NGX-HTlc samples, suggesting a heterogeneous distribution of Ga_2O_3. This may be because the introduction of additional elements increased the possibilities for Ga_2O_3 to interact with multiple species. Furthermore, the Ga_2 in NGZn-HTlc shifted to a higher temperature compared with other samples. The reason was that Ga trapped in the $ZnGa_2O_4$ spinel structure was more difficult to reduce, resulting in an increased reduction temperature. It was worth mentioning that the Ni_2, Ga_1 and Ga_2 peaks shifted to a lower temperature in case of NGZr-HTlc. The incorporation of ZrO_2 in general could facilitate the reducibility of the nickel and gallium oxides. And it could also be proposed that the ZrO_2 enhanced the separation (acted as spacer) of Ni-Ga bimetallic alloy, and thus contributed to an easier reduction of NGZr-HTlc sample. There were no obvious reduction peaks for promoters, and thus the promoters (Mg, Zn and Zr) were all in oxidation state.

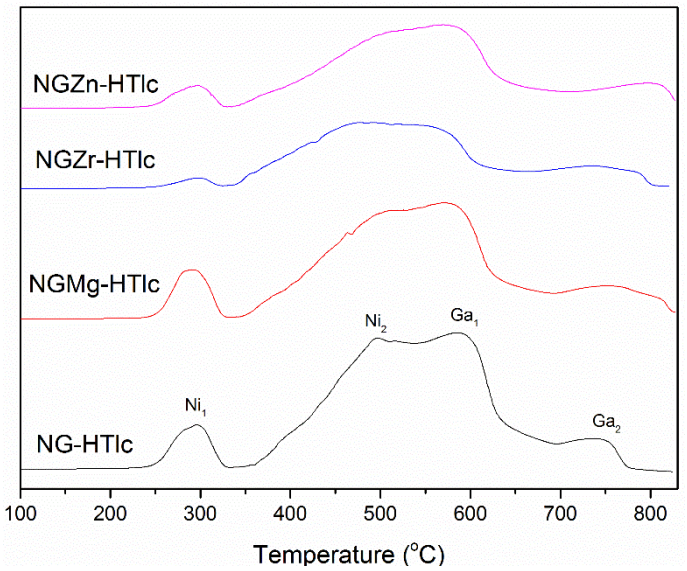

Fig. 35 TPR curve of NGX-HTlc precursor

An in-situ synchrotron PXRD H_2 reduction measurement on NGZr-HTlc was carried out to investigate the reduction step and the formation process of Ni_3Ga bimetallic alloy. Initially, the HTlc structure did not exhibit obvious change below the reduction temperature of 200 °C. The (003) plane, located at around 2θ =6.0°, representing the layered structure, exhibited a sharp decrease when the NGZr-HTlc was reduced over 200 °C, and it completely disappeared at 400 °C, indicating that the HTlc structure was decomposed and re-construct during the synthesis of Ni-Ga bimetallic catalysts. The NiO was formed simultaneously with the decomposition of HTlc structure, with the appearance of NiO (111) and (220) plane, located at 2θ = 18.1° and 35.0°. The NiO was slowly reduced to metallic nickel above 300 °C, with a major PXRD reflection positioned at 2θ=30°, and the Ga_2O_3 was subsequently alloyed with bimetallic nickel to form Ni_3Ga at 550 °C, with a characteristic peak located at 2θ=24.6° representing Ni_3Ga (200) plane.

Summarily, the reduction process started with the decomposition of HTlc structure to NiO and Ga_2O_3. The NiO was firstly reduced to metallic nickel above 200 °C, which then facilitated the reduction of Ga. The Ni_3Ga was slowly synthesized above 550 °C, and a considerably sharp and clear PXRD pattern representing the Ni_3Ga phase appeared.

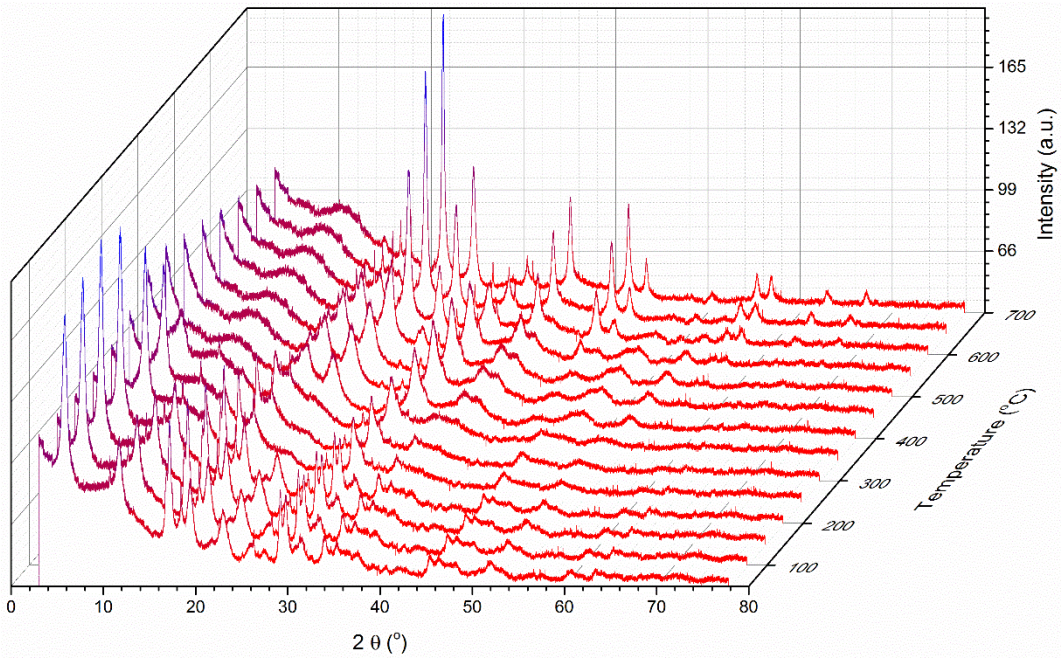

Fig. 36 In-situ synchrotron PXRD H_2 reduction profile

5.3.3 CO_2 adsorption properties of NGX-redu catalysts

The surface basicity is important for CO_2 hydrogenation reactions because CO_2 is expected to be adsorbed and activated around the basic sites. Here, the CO_2-TPD profile for NGX-redu catalysts is shown in Fig. 37. In the NG-redu reference sample, three major CO_2 desorption peaks were observed, which are denoted as α, β and γ, respectively. The α peak, located below 100 °C, represented a weak basic site wherein CO_2 attached linearly with a metal atom to form O=C=O-M (M represented metal atom). The β and γ corresponds to medium basic sites with a bridge-bonded adsorptive form, which enhanced the CO_2 desorption difficulty and thus increased the CO_2 desorption temperature. The β and γ desorption peaks were assigned to two types of metal-oxygen pairs, which are Ga-O and Ni-O[128], respectively. Another desorption peak (σ) located at higher temperatures was observed in NGMg-redu and NGZr-redu samples. The σ peak suggested a strong basic site generated by the metal oxide promoters. Considering that the alkaline MgO exhibits stronger basicity compared with ZrO_2, the σ peak in NGMg-redu TPD profile was at lower temperature than that in NGZr-redu TPD curve because the CO_2 was strongly attached to a highly alkaline metal oxide. The σ peak did not appear in the NGZn-redu TPD profile, however, a strong γ appeared at a relatively low temperature

around 350 °C, corresponding to medium basic site, attributed to the formation of $ZnGa_2O_4$, which was similar to the reported CO_2-TPD curve of $ZnAl_2O_4$[129].

The NGZr-redu samples were exposed to the CO_2 environment and heated from room temperature up to 300 °C. The corresponding structural information was collected by in-situ synchrotron PXRD measurement. The results showed no obvious change during the process, suggesting a good chemical and thermal stability of as-prepared catalysts under reaction conditions.

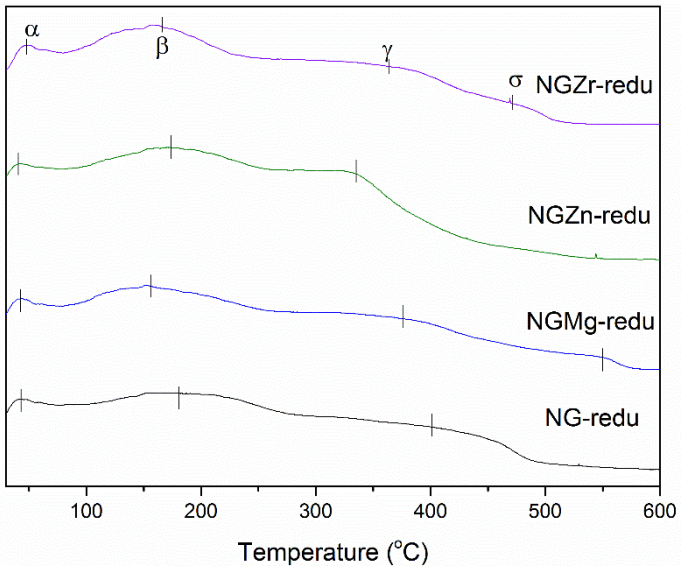

Fig. 37 CO_2-TPD profiles of NGX-redu samples

5.3.4 Surface properties of the catalysts

The electron states of the as-prepared NGX-redu catalysts were investigated by XPS analysis, and the XPS curves were fitted accordingly. As can be seen in Fig. 38(a-d), two states of gallium were observed. The photoelectron component at around 18 eV, which was close to the value of gallium in the metallic state ($Ga_{(0)}$) in literature, belonged to the gallium element in Ni-Ga alloy, while the one located near 21 eV was due to the gallium in oxidation state ($Ga_{(3+)}$), which overlapped with O (2s) peaks. Thus, the gallium was not completely reduced from the parent HTlc precursor, and most of the surface gallium remained in an oxidation state. A split of O(2s) was observed in NGMg-redu samples, located between $Ga_{(3+)}$ and O (2s), and the additional O(2s) peak was due to a surface contamination when the sample

was exposed to air during the XPS measurement. The molar ratio of $Ga_{(0)}$ and $Ga_{(3+)}$ was calculated and summarized in Table 11. An increased amount of reduced gallium was found when the promoters were incorporated into the HTlc framework, compared with the reference NG-redu catalyst. As was discussed in the literature[130], a better interaction between active sites and promoters would facilitate the electron transfer, and thus reduced gallium was more easily generated on the surface, resulting in a higher amount of gallium in the metallic state. It was clearly observed that the NGZr-redu possessed the highest amount of $Ga_{(0)}$ compared with other samples, suggesting that the ZrO_2 interacted closely with Ni-Ga bimetallic alloy. And an enhanced reducibility from ZrO_2 could also contribute to facilitating the reduction of gallium, as was discussed in the TPR result.

Nickel was found to be more easily reduced, and a higher amount of metallic nickel ($Ni_{(0)}$) was detected, compared with that of $Ga_{(0)}$, as was summarized in Table 11. Despite an easier reduction, the existence of nickel native oxide ($Ni_{(2+)}$) suggested an incomplete reduction of all NGX-redu samples (Fig 39). Similar results were observed in Ni 2p XPS measurement, that an enhanced Ni-promoter interaction enhanced NiO reduction in all NGX-redu samples with the introduction of promoters in HTlc framework. The presence of ZrO_2 in NGZr-redu sample contributed to a better dispersion of Ni-Ga alloy, which subsequently could lead to an easier reduction.

Table 11 Surface composition of NGX-redu catalysts

Sample	Ni 2p metal alloy/ Ni 2p native oxides	Ga 3d metal alloy/ Ga 3d native oxides
NG-redu	16.6:83.4	5.6:94.4
NGMg-redu	28.3:71.5	7.2:92.5
NGZn-redu	24.1:75.9	13.6:86.4
NGZr-redu	46.1:53.9	22.5:77.5

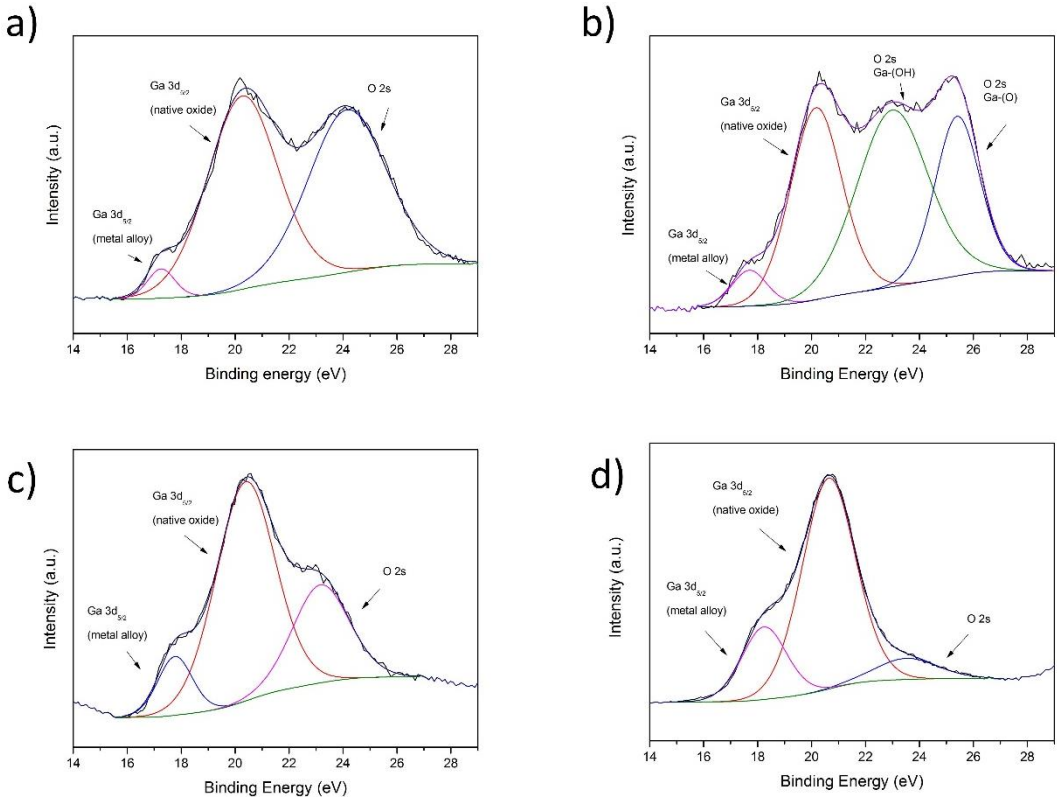

Fig. 38 XPS spectra of Ga(3d) of the prepared catalysts: a) NG-redu; b) NGMg-redu; c) NGZn-redu; d) NGZr-redu

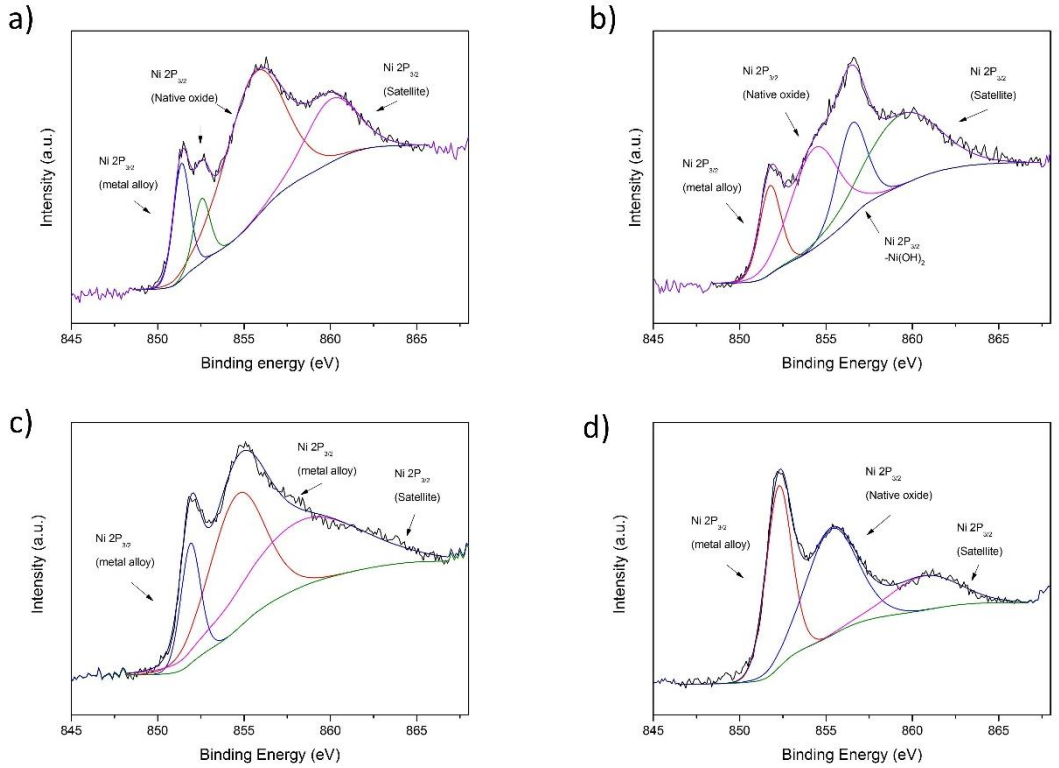

Fig. 39 XPS spectra of Ni(2p) of the prepared catalysts: a) NG-redu; b) NGMg-redu; c) NGZn-redu; d) NGZr-redu

5.3.5 Catalytic performance

5.3.5.1 CO_2 hydrogenation results

The catalytic performance of as-prepared NGX-redu catalysts was tested for CO_2 hydrogenation to methanol, and the results are reported in Fig. 40, in terms of CO_2 conversion (a) and methanol selectivity (b) under a temperature range from 200 °C to 300 °C at 3.0 MPa with a space velocity of 373.3 mL $g^{-1}h^{-1}$. It was clearly observed that the CO_2 conversion was greatly enhanced when promoters were incorporated into the original Ni-Ga catalysts. Generally, the overall CO_2 conversion increased as the reaction temperature increased for all catalysts studied. Additionally, as can be seen from Fig. 40 (a), the NGMg-redu exhibited a slightly better CO_2 conversion compared with original Ni_3Ga catalysts, while a sharp increase in CO_2 conversion was observed in the case of NGZn-redu and NGZr-redu under the entire temperature range. Even though the as-prepared Ni-Ga catalysts exhibited a lower CO_2 conversion, NGZr-redu showed a comparable methanol yield to commercial Cu-based catalyst at 300 °C, as can be seen in Fig. 40 (b). However, the highest methanol was observed in NGMg-redu catalysts, reached over 80% even at 300 °C, and the methanol selectivity of as-prepared NGX-redu catalysts surpassed that of Cu-based catalyst (Fig. 40-b).

The by-product, generated during the methanol synthesis reaction, varied greatly based on the nature of the as-prepared NGX-redu catalyst. CH_4 was the main product in the case of NGZn-redu catalyst (Fig. 40-e), and the CH_4 yield considerably exceeded all the catalysts, especially at elevated temperatures, (>250 °C), where the CO_2 methanation reaction was greatly promoted. Also, the CO production was drastically suppressed, and only trace amounts of CO was detected in the entire temperature range. An enhanced CH_4 production was ascribed to the formation of $ZnGa_2O_4$ spinel structure in NGZn-redu catalyst, which was reported to enhance the CO_2 hydrogenation to CH_4[131]. Overall, the CO production was greatly surpassed when promoters were introduced, when compared with Cu-based catalysts and NG-redu catalyst, as can be seen from Fig. 40 (d).

The chemical and thermal stability of NGZr-redu catalysts were investigated by Time-on-Stream (TOS) measurement, as can be seen in Fig. 41. No obvious

decrease in CO_2 conversion was observed over 100 hours, suggesting the catalyst was stable under reaction conditions.

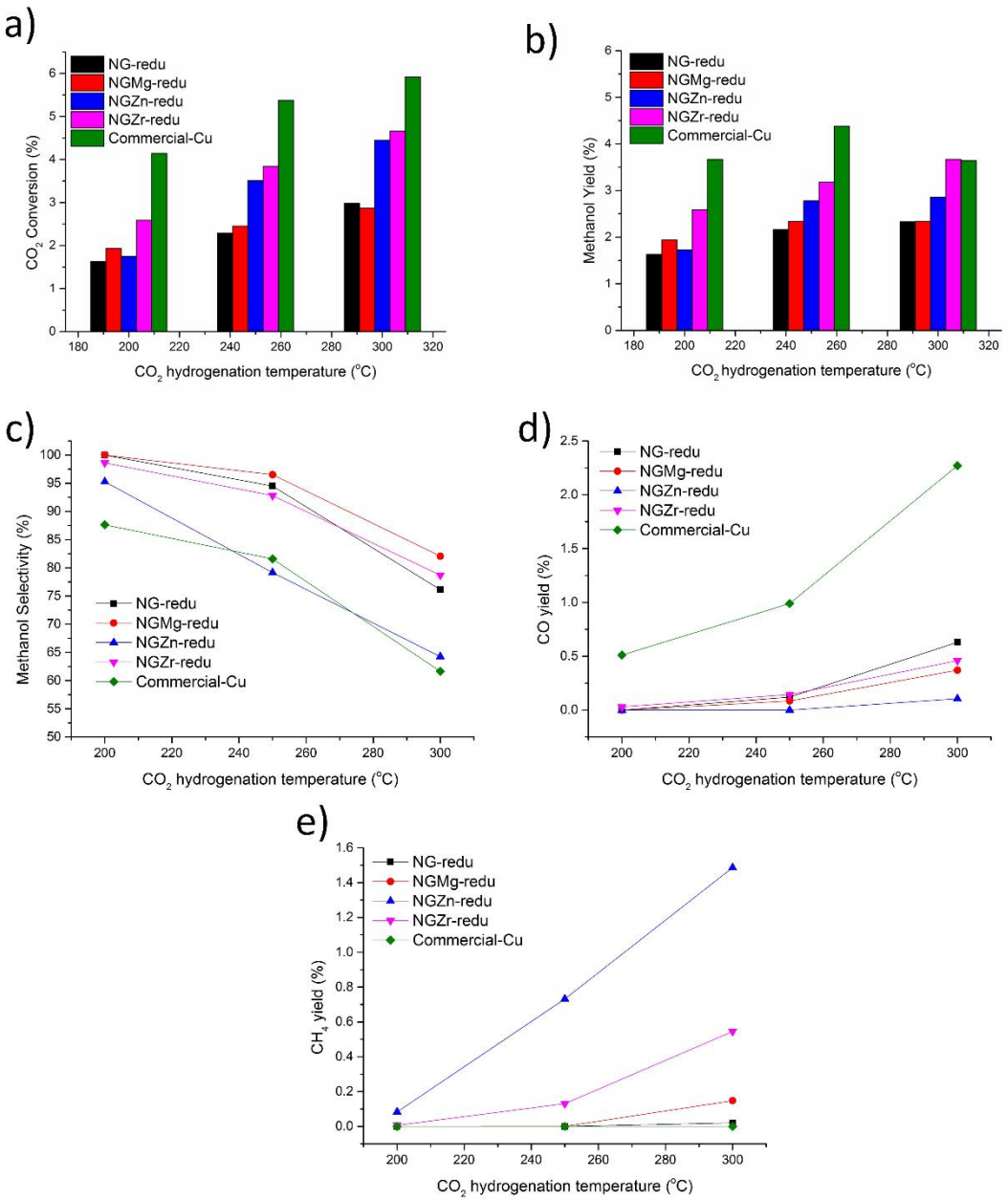

Fig. 40 a) CO_2 conversion, b) methanol yield, c) methanol selectivity, d) CO yield and e) CH4 yield at 3.0 MPa with a space velocity of 373.3 mL $g^{-1}h^{-1}$

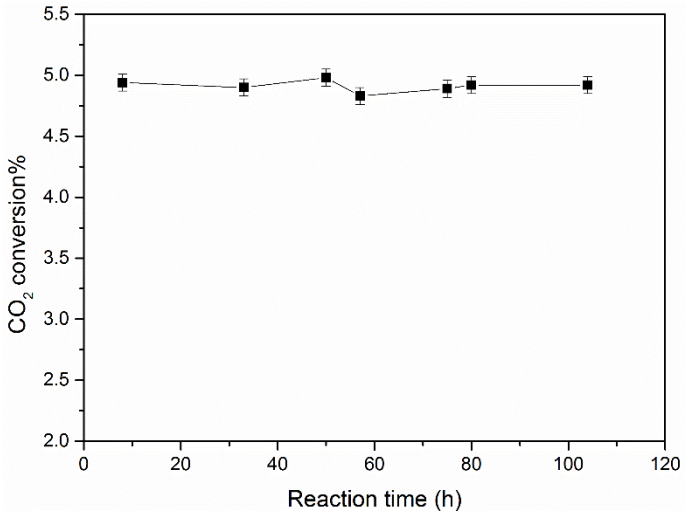

Fig. 41 Time-on-Stream reaction in terms of CO_2 conversion and reaction time for methanol synthesis

5.3.5.2 Catalytic functionality

As discussed earlier in Chapter 2, there were two major reaction pathways for methanol synthesis from CO_2, namely the formate pathway and the rWGS pathway, as shown in Fig. 42. The reaction route is still under debate; however, it was acknowledged that the stability of essential intermediates would determine the direction of the different reaction pathways. For instance, Yang and co-workers[132] suggested that methanol was not generated via rWGS reaction pathway because *HCO is not a stable intermediate and will decompose back to *CO + *H. Also, the slow steps (Rate Determining Steps) determine which pathway the reaction follows, and thus an enhanced binding energy to prevent intermediate dissociation and moderately increase the intermediate stability could alter the reaction route by incorporating additional elements in the catalyst matrix. In this study, promoters, such as Mg, Zn, and Zr were incorporated into the original Ni-Ga catalytic system, these could provide more adsorption and reaction sites on the interface, which would be very difficult to generate on pure metal alloy system[133]. The corresponding intermediate adsorption site would have an impact on the binding energy of key intermediate, thus increase the overall reaction performance and alter the reaction pathway accordingly.

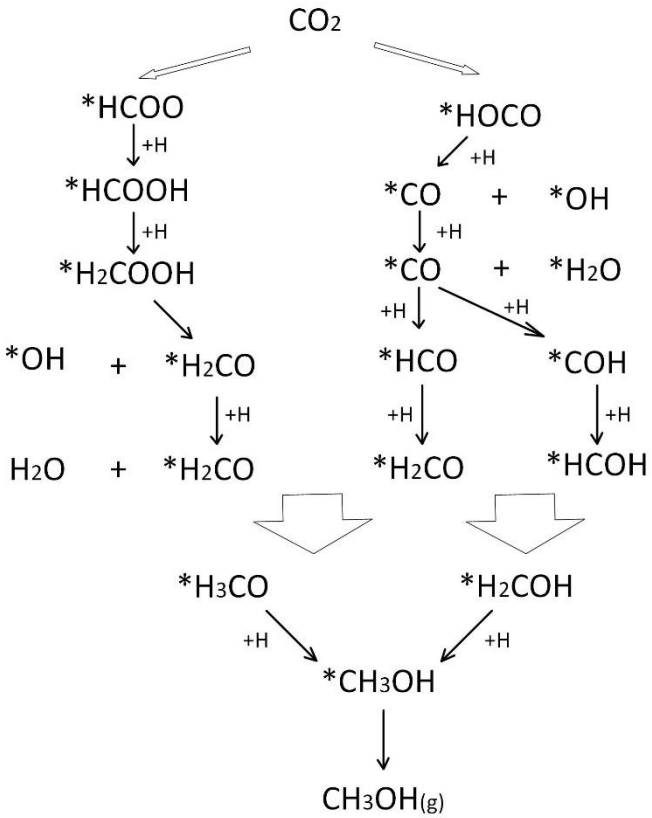

Fig. 42 Reaction pathway for CO_2 hydrogenation to methanol via formate (left route) rWGS pathway (right route)

When Mg and Zr were introduced into the Cu framework, it was reported that the mechanism leaned towards the formate pathway. As was reported in the literature[134, 119], the formate pathway was thermodynamically favoured by Mg-Cu catalytic combination, and CO was considerably surpassed; also, an enhanced CO_2 conversion was reported via ZrO_2-Cu matrix. Specifically, ZrO_2 was able to stabilize the key intermediate generated in the formate pathway, such as *HCOO, *H_2CO and *H_3CO[135]. The results reported in the literature were in accordance with those obtained via Ni-Ga-Mg and Ni-Ga-Zr in this study; and methanol selectivity was highest in the case of Ni-Ga-Mg with a hindered CO production. Furthermore, Ni-Ga-Zr exhibited a greatly improved CO_2 conversion as compared with bulk Ni-Ga catalyst.

The catalytic performance was related to the surface basic sites, measured by CO_2-TPD, which was reported in section 5.3.3. The medium basic sites, namely β and γ basic sites, which adsorb species with atomic hydrogen via a stepwise hydrogenation to form *HCOO, *H_2COO, *H_2COOH and *H_2CO[136]. The generated *H_2CO would be stabilized by a stronger σ basic site a reverse reaction to produce

CO[136] can be prevented. As a result, promoters such as MgO and ZrO_2 with σ basic site would reduce the production of CO. In addition, a higher methanol selectivity was observed in MgO because of a higher alkalinity compared with ZrO_2. However, Ni-Ga-Zr catalysts exhibited a higher CO_2 conversion and methanol yield, because a slightly weak σ basic site would help the intermediate desorption from the active sites and accelerate the hydrogenation step to synthesize methanol.

5.4 Conclusion

In this Chapter, promoters, namely Mg, Zn and Zr, were introduced into Ni-Ga catalytic system via similar HTlc precursors. The formation of Ni-Ga type HTlc precursors was confirmed by PXRD patterns, and the Ni_3Ga instead of Ni_5Ga_3 phase was formed in all as-prepared samples. An obvious decrease in particle size was observed in the Ni-Ga-Zr catalytic matrix with a greatly enhanced specific surface area, while other promoter modified catalysts only exhibited a minor change in catalyst grain size. The Ni-Ga alloy and promoters were uniformly dispersed in the Ni-Ga-X matrix, as revealed by SEM-EDS. An enhanced interaction between Ni-Ga bimetallic catalysts and promoters was observed with an increased reduction temperature in the TPR profile. Addition of ZrO_2 increased the overall reducibility of the catalyst and the reduction peak shifted to lower temperatures. However, all catalysts underwent an incomplete H_2 reduction, revealed from the XPS data analysis. Among the NGX-redu samples studied, the NGZr-redu exhibited the highest ratio of reduced metal to native oxides, which was supported by the TPR results, due to smaller particle size and increased reducibility. The catalytic basic sites were investigated for all the as-prepared samples via CO_2-TPD. Apart from NGZn-redu ($ZnGaO_4$ spinel structure), MgO and ZrO_2 in the Ni-Ga system brought a strong σ basic site at elevated temperature compared with NG-redu catalyst, which contributed to an enhanced methanol selectivity and CO_2 conversion. There was an obvious enhancement in terms of CO_2 conversion and methanol yield for all promoter-modified Ni-Ga catalysts, and CO production was hindered for both NGZr-redu and NGMg-redu, and the NGZr-redu exhibited the highest methanol yield (3.8%), which was comparable with the Cu-based catalyst at 300 °C.

Chapter 6 Ni-Ga-Zr Catalyst modified with high-temperature CO_2 adsorbent for CO_2 hydrogenation to methanol

6.1 Introduction

In the previous chapter, a novel catalyst, Ni-Ga-Zr, was successfully synthesized, and the corresponding catalytic performance, such as methanol yield, was found to be comparable with commercial Cu-based catalysts at 300 °C. However, Ni-Ga-Zr catalyst showed a weak catalytic performance at lower temperatures, such as 200 °C and 250 °C. One way to increase the CO_2 conversion in methanol synthesis was to enhance the reactant concentration around the catalytic active sites. In our case, high-temperature CO_2 adsorbents, such as hydrotalcite, could adsorb CO_2 and water at elevated temperatures such as 200 °C-300 °C, which would be a perfect candidate to promote the methanol synthesis reaction.

Here, we report a Ni-Ga-Zr catalyst modified with a high-temperature CO_2 adsorbent, based on the 'sorption enhanced reaction' concept. Specifically, a high-temperature CO_2 adsorbent was activated and mixed with as-prepared Ni-Ga-Zr catalysts. The structure of the mixed catalyst system was examined by PXRD and SEM-EDS. In addition, the catalytic performance was investigated at different pressures, temperatures, and space velocity. Additionally, the mechanism of the CO_2 adsorbent modified process was also discussed.

6.2 Methodologies

6.2.1 Physically mixed NGZr/MG50 powder

Ni-Ga-Zr catalyst was synthesized and reduced as described in Chapter 5, and it was denoted as NGZr. The high-temperature CO_2 adsorbent, MG50, was activated at 400 °C for 6 hours with a ramp rate of 1 °C/min. The NGZr was mixed thoroughly with MG50, and the weight percentage of NGZr in MG50 varied from 0% to 100%. The obtained mixture was pelletized, crushed to 40-60 mesh. 1 gram of the as-prepared mesh particles was mixed with quartz sand and rapidly transferred to the reactor, under a continuous N_2 flow.

6.2.2 Physically mixed NGZr/MG50 pellets

NGZr and MG50 were synthesized and activated as described in section 6.2.1. The activated MG50 and reduced NGZr was pelletized into particles in 40-60 mesh, separately. The as-obtained particles were mixed with each other subsequently. Similarly, 1 gram of the as-prepared particle was diluted by quartz sand and transferred to the reactor with a continuous N_2 flow.

6.2.3 Activation of Ca-Chabazite and 13X

Control experiments were carried out to investigate if different high temperature CO_2 adsorbents affected the overall catalytic performance. Ca-Chabazite and 13X zeolites were step-activated as follows: The adsorbents were heated at 100 °C for 6 hours, and the temperature was subsequently raised to 400 °C with a heating rate of 1 °C/min and maintained for another 6 hours. The Ca-chabazite was physically mixed with NGZr powder as described in section 6.2.1, followed by palletisation (40-60 mesh) and dilution by quartz sand.

6.3 Results and Discussion

6.3.1 Structure and morphology

The thermal stability of MG50 was investigated by TG measurements, as shown in Fig. 43. The TG pattern exhibited a typical 3-stage weight loss, including physically adsorbed water removal, dihydroxylation and decarbonization, respectively. When MG50 was calcinated at 400 °C, most of the water and CO_2 were removed from the layers with a reversible decomposition of the layered structure. However, it still exhibited the ability to absorb CO_2 and water, hence, activation at 400 °C stimulated the ability of CO_2 and water adsorption, which would be beneficial as a promoter for methanol synthesis. It would not be necessary to consider ‘memory effect’ for MG50 due to high reaction temperature.

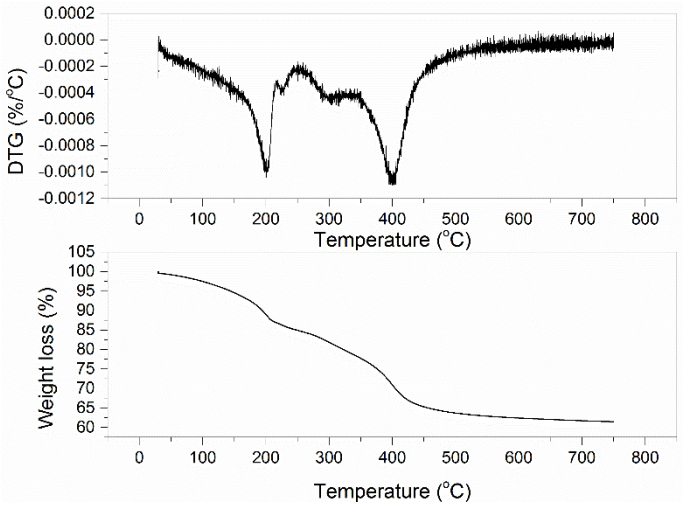

Fig. 43 TG and DTG patterns of MG50

The PXRD patterns of calcinated MG50 and NGZr/MG50 mixture are shown in Fig. 44. The NGZr/MG50 exhibited typical Ni_3Ga and ZrO_2 planes, indicating that the Ni-Ga bimetallic catalyst was not influenced by the introduction of a high-temperature CO_2 adsorbent. The calcinated MG50 possessed 3 “hump”-like broad peaks, with the disappearance of typical (00l) planes indicating layered structure. The decomposition of layers was ascribed to high-temperature calcination, where the typical layered structure was partially destroyed, and the broad peaks represented the amorphous Mg-Al metal oxides.

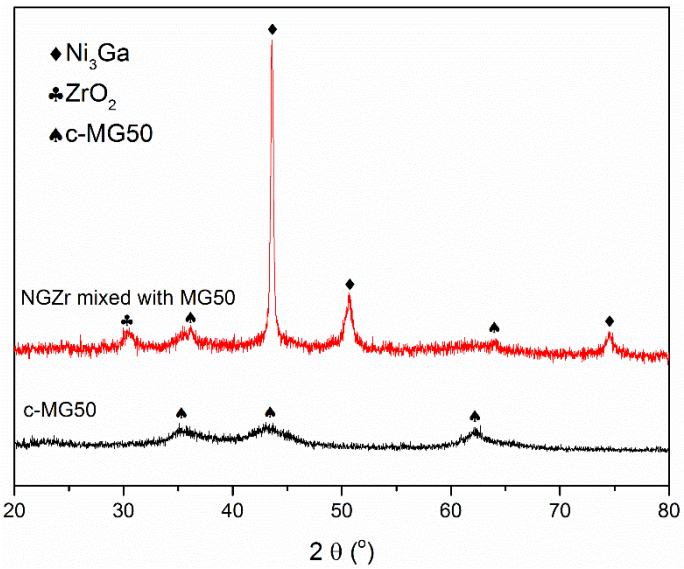

Fig. 44 PXRD patterns of calcinated MG50 and NGZr/MG50 physically mixture

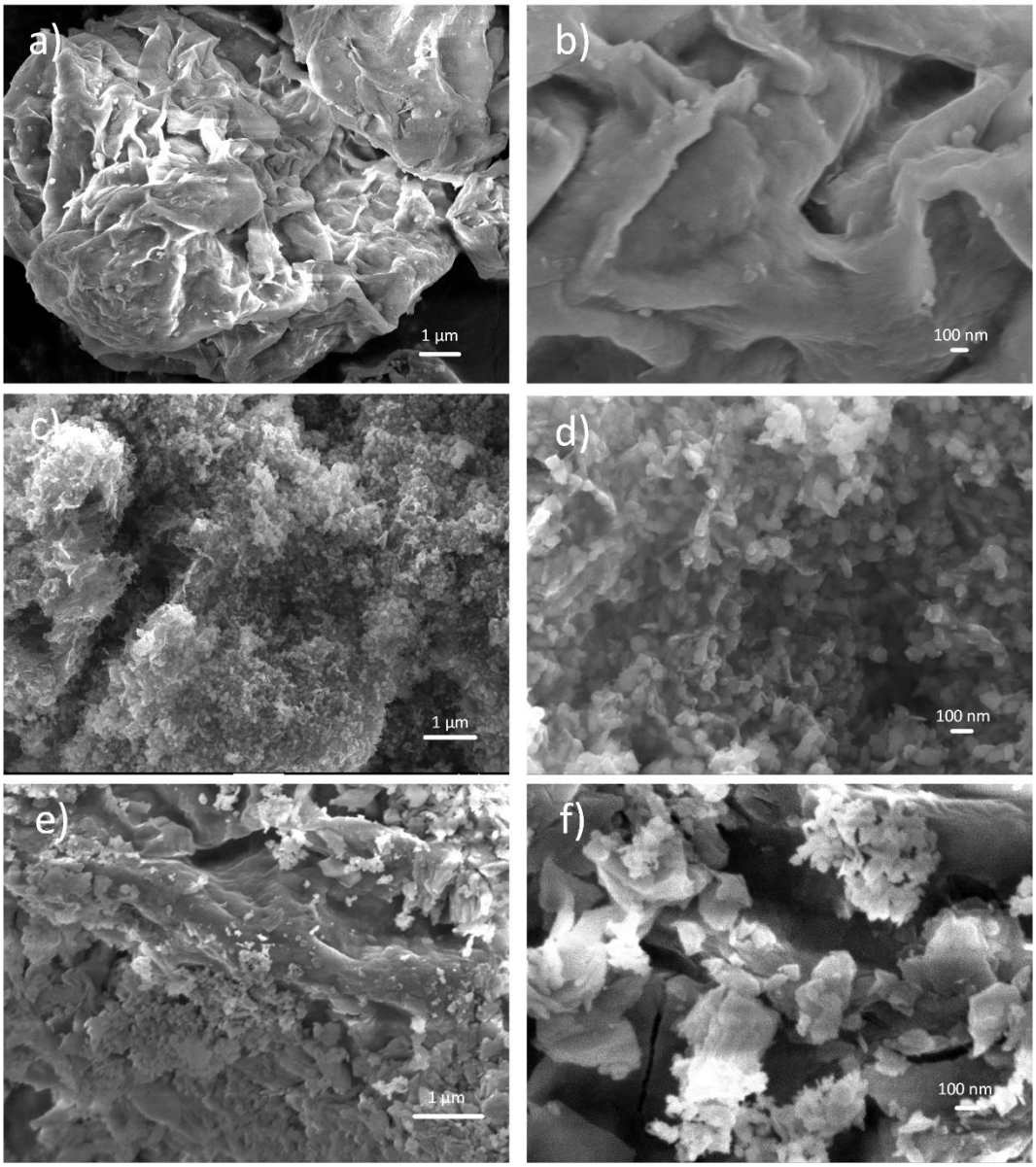

Fig. 45 SEM pictures of a) b) calcinated MG50, c) d) NGZr catalyst, e) f) NGZr/MG50 powder mixture

The SEM images described the morphology of calcinated MG50, NGZr catalysts and their corresponding powder mixture. The calcinated MG50 exhibited a flower-like shape around 8-10 µm (Fig. 45(a)), with a folded layers and irregular channels (Fig. 45(b)), while NGZr (Fig. 45 c-d) catalyst revealed a considerably smaller particle size. As can be seen from Fig. 45 (e), MG50 played as a support for NGZr particles, and the two components were thus well-mixed.

6.3.2 Catalytic properties

6.3.2.1 Primary experiment with MG50 and quartz sand

The promotion effect of MG50 in methanol synthesis was investigated. Thus, an equal amount of calcinated MG50 and quartz sand were mixed with the same amount of reduced NGZr catalyst (50/50), respectively. It could be observed that the CO_2 conversion showed an increasing trend as temperature increased, and the overall CO_2 conversion via MG50 modified NGZr catalyst was almost two times higher than NGZr mixed with quartz sand alone, as shown in Fig. 46. The methanol selectivity was also greatly enhanced, especially at elevated temperatures, for example, the methanol selectivity was increased by 10% at 300 °C. The result illustrated that high-temperature CO_2 adsorbent modified catalyst exhibited an enhanced methanol synthesis performance, with a higher CO_2 conversion and methanol selectivity.

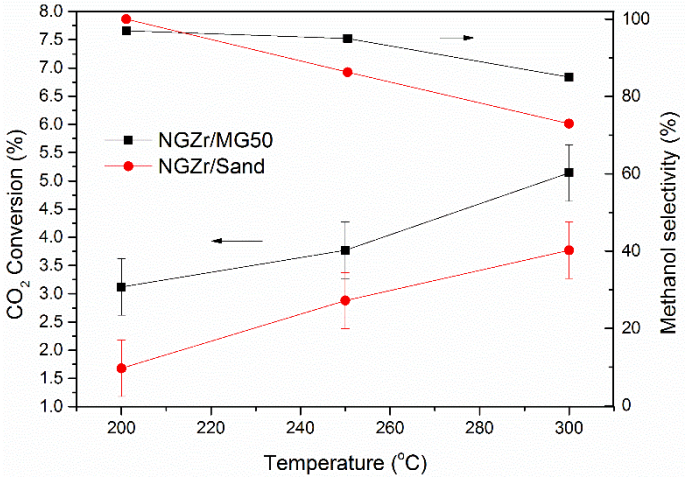

Fig. 46 CO_2 conversion and methanol selectivity via NGZr/MG50 (50/50) and NGZr/sand (50/50), respectively

The CO_2 conversion at different pressures as well as varied reaction temperature was plotted in Fig. 47. Overall high temperature promoted CO_2 conversion, while the catalytic performance was weakened at low reaction temperatures. High temperature activated gaseous molecules, and thus accelerated the overall reaction rate. However, it could be observed that the CO production was also enhanced as temperature increased from 200 °C to 300 °C; since the rWGS reaction was an endothermic reaction and was promoted by higher temperatures. The pressure also greatly affected the results. For example, the average CO_2 conversion under 30 bar was almost two times higher than under 10 bar. The methanol selectivity was greatly enhanced as pressure increased, as can be seen from Fig. 48. The reason was ascribed to the fact that the overall molecule number decreased in the methanol synthesis reaction, which was favoured by high

pressures (Le Chatelier's Principle). The rWGS reaction was not influenced by the pressures because the molecules of reactants equalled to that of products. The rWGS reaction competed with the methanol synthesis reaction under reaction conditions, as a result, the overall CO_2 conversion was highly promoted at elevated pressures due to the greatly enhanced methanol synthesis reaction.

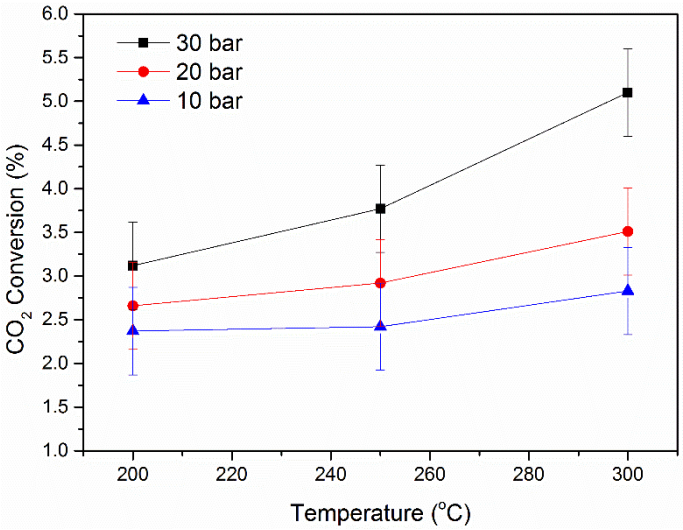

Fig. 47 CO_2 conversion in terms of a temperature range between 200 °C and 300 °C under 10 bar, 20 bar and 30 bar

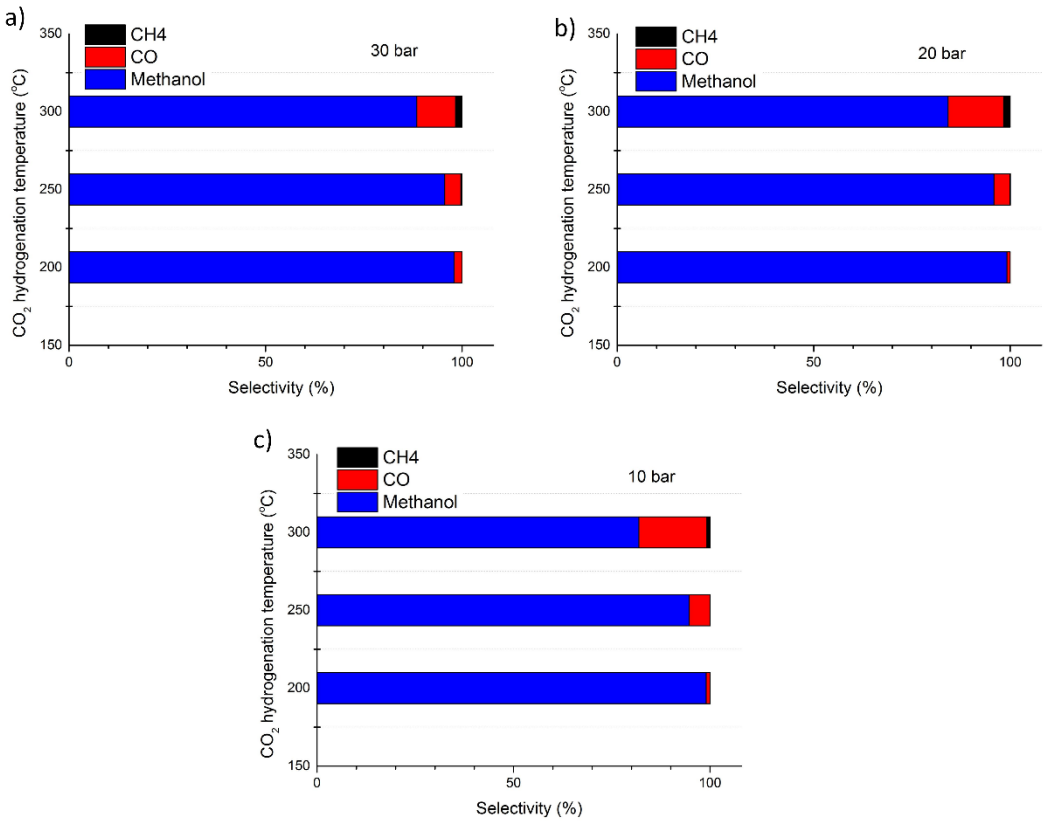

Fig. 48 The selectivity of methanol, CO and CH_4 under 10 bar, 20 bar, 30 bar, respectively

6.3.2.2 Impact of CO_2 adsorbent amount

Different amounts of calcinated MG50 was mixed with NGZr catalyst, as can be seen from Fig. 49, and the catalytic performance was investigated subsequently.

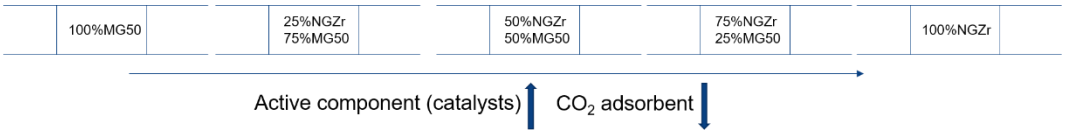

Fig. 49 NGZr reduced catalysts mixed with calcinated MG50 by different ratio

As can be seen from Fig. 50 (a), the overall CO_2 conversion increased as proportion of NGZr catalyst increased in the mixture. An increasing amount of NGZr catalyst provided more active sites, contributing to a higher CO_2 conversion, and pure MG50 hardly exhibited any catalytic performance. However, it was worth mentioning that the CO_2 conversion decreased slightly as MG50 percentage increased in the catalytic system, instead of a rapid drop due to the loss of the catalytic active sites from NGZr samples. To explain it more clearly, the space-time yield (STY) was subsequently calculated, as can be seen in Fig. 50 (b). The highest STY was achieved in 25 wt% NGZr modified by 75 wt% MG50, with 123.5 $g_{meth}{\cdot}g_{cat}^{-1}{\cdot}h^{-1}$ at 300 °C, 30 bar. The results suggested that the catalytic property of a single NGZr active site was greatly enhanced when it was mixed with MG50. Thus, a comparable CO_2 conversion could be achieved with lower catalyst amount when modified by high-temperature CO_2 adsorbent. The methanol selectivity barely changed at low reaction temperature region (eg. 200 °C and 250 °C), however, a mild decrease was observed as the MG50 amount increased at 300 °C. In general, MG50 promoted both rWGS and methanol synthesis, while methanol synthesis was more facilitated at elevated temperatures. As a result, the promotion effect of methanol synthesis surpassed that of rWGS reaction.

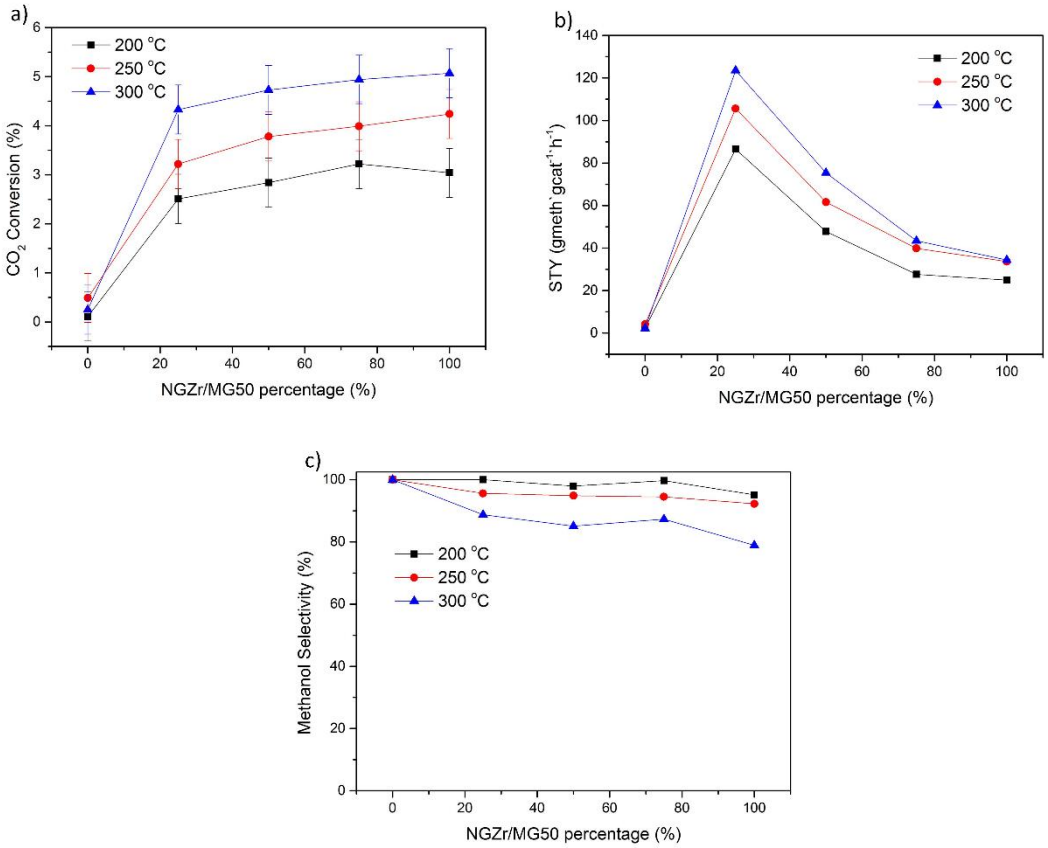

Fig. 50 a) CO_2 conversion, b) Space-time yield (STY), c) Methanol selectivity in terms of different NGZr to MG50 ratio under 200 °C-300 °C, 30 bar

6.3.2.3 Impact of space velocity

The space velocity represents the contact time between catalysts and reactants. Since 25% NGZr/MG50 revealed the highest STY value, it was further investigated in this section and the impact of space velocity on the catalytic performance via 25% NGZr/MG50 was reported in Fig. 51. The increase of space velocity attributed to a shorter contact time between catalysts and gaseous reactants, and thus the overall CO_2 conversion decreased as expected. The methanol selectivity, however, exhibited a gradual increase from 80% to 90% from 1800 mL g^{-1} h^{-1} to 3600 mL g^{-1} h^{-1}, and the by-product CO decreased accordingly. The methanol and water could not be continuously removed from the active sites under low space velocity (mass transfer limitation), and the methanol synthesis reaction was thus restricted, contributing to a low methanol selectivity. However, the CO_2 conversion and methanol selectivity remained roughly unchanged at higher space velocity in the

range 3000 mL $g^{-1}h^{-1}$ to 3600 mL $g^{-1}h^{-1}$, suggesting that moderate space velocity strongly promoted methanol synthesis.

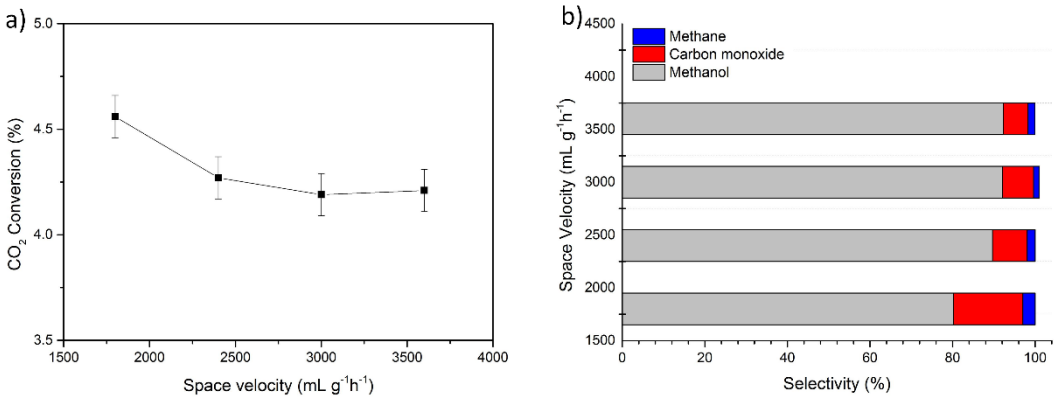

Fig. 51 a) CO_2 conversion and b) methane, carbon monoxide and methanol selectivity via 25% NGZr/MG50 in terms of space velocity at 300 °C

6.3.2.4 Impact of different high-temperature CO_2 adsorbents

To investigate the impact of different high-temperature CO_2 adsorbent on the overall catalytic properties, the CO_2 adsorption ability of 13X, Ca-Chabazite and MG50 in a temperature range of 200 °C to 300 °C was measured, respectively. As can be seen from Fig. 52, the CO_2 adsorption amount in 13X and Ca-chabazite was almost linear, while MG50 exhibited an arc-like shape in terms of pressure. The result was attributed to different CO_2 adsorption modes for measured materials. 13X and Ca-chabazite zeolite both possess a great number of micropores constructed from Si and Al as well as Na^+ and Ca^{2+} as charge balancing cations in the framework. CO_2, a highly polar molecule, was adsorbed via physisorption, resulting in a linear relationship between CO_2 adsorption amount and partial pressures. However, the Van-der-Waals force between CO_2 molecules and zeolites was weakened at elevated temperatures (Fig. 52-a,b). Hence, zeolites such as 13X and Ca-chabazite are a potential candidate for CO_2 adsorption under room and moderate temperatures. It was clearly observed that, for example, the CO_2 adsorption amount of Ca-chabazite (Fig. 52 (b)) considerably reduced from 0.91 mmol/g to 0.23 mmol/g as temperature decreased from 300 °C to 200 °C, and similar results were observed in that of 13X. On the contrary, CO_2 was adsorbed by a different mechanism in case of MG50. CO_2 was adsorbed on the strong basic sites via chemisorption on MG50, resulting in higher adsorption capacity which subsequently showed a mild increase at elevated pressure. Considering that the

CO_2 adsorption amount of Ca-chabazite was higher than that of 13X, the NGZr catalysts were subsequently mixed with Ca-chabazite, and the catalytic performance was compared with NGZr/MG50 catalytic system.

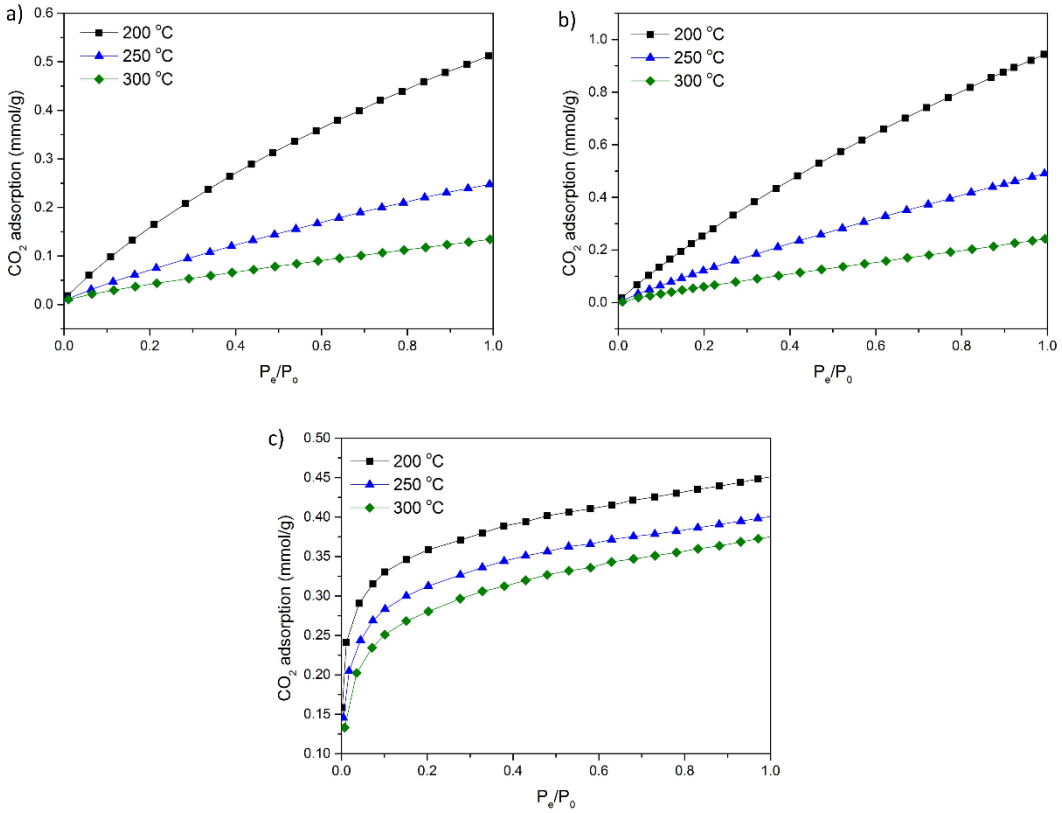

Fig. 52 CO_2 adsorption of a) 13X, b) Ca-Chabazite, c) MG50 under 200 °C, 250 °C and 300 °C

The CO_2 conversion of 25% NGZr/MG50 and 25% NGZr/Ca-chabazite is shown in Fig. 53. It could be observed that at low temperature such as 200 °C, the catalytic performance was comparable, while the CO_2 conversion decreased as reaction temperature increased, and the overall CO_2 conversion of NGZr/Ca-chabazite decreased almost to half of that via NGZr/MG50 catalyst at 300 °C. The promotion effect of MG50 is due to its medium CO_2 adsorption ability, and it can also desorb CO_2 between the reaction temperature range (150 °C- 350 °C)[137]. The CO_2 conversion decrease at elevated temperature could be ascribed to two main reasons. Firstly, the CO_2 adsorption ability of Ca-chabazite at high temperature was considerably lowered due to a weak Van-der-Waals forces of attraction between CO_2 and Ca^{2+}. In addition, the zeolite experienced dealumination at elevated

temperature probably, due to generation of water, resulting in a partial collapse in the zeolite framework, resulting in further decrease in CO_2 adsorption capacity. The Al:Si ratio of Ca-Chabazite zeolite before and after the methanol synthesis reaction was determined by SEM-EDS mapping. The Al:Si ratio decreased from 0.44 to 0.26, which proved that the zeolite framework was partially decomposed with water vapor at elevated temperature[138]. Consequently, the enhancement from CO_2 adsorbent to the overall catalytic system was greatly reduced.

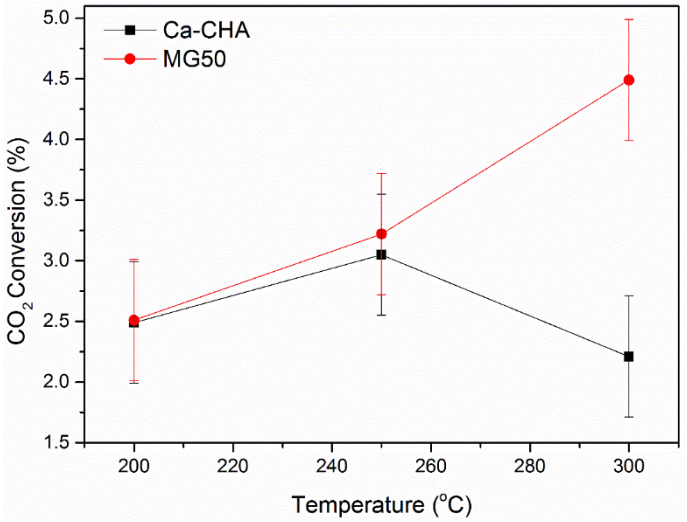

Fig. 53 CO_2 conversion of NGZr/MG50 and NGZr/Ca-Chabazite catalysts under 200 °C-300 °C at 30 bar

6.3.2.5 Impact of packing mode between MG50 and NGZr catalyst

To investigate the catalytic performance in terms of the packing mode, the NGZr catalysts and MG50 was mixed in the form of pellets and powder, respectively, as shown in Fig. 54. The corresponding CO_2 conversion was reported in Fig. 55. The CO_2 conversion of NGZr/MG50 powder far surpassed that via NGZr/MG50 pellet, and the latter exhibited a slightly higher CO_2 conversion compared with commercial Cu-based catalysts. By mixing NGZr and MG50 with pellets, the distance between catalyst particle and high temperature CO_2 adsorbent was increased, while the NGZr/MG50 powder provided a more intimate contact between catalyst and powder. The shorter distance contributed to a higher CO_2 concentration adjacent to Ni-Ga bimetallic active sites, thus enhancing the corresponding CO_2 conversion, which was almost two times higher than bulk Ni-Ga catalysts (NGZr/quartz sand). The catalytic properties from NGZr/MG50 pellet, however, barely exhibited any

promotion effect due to a considerably longer distance between the CO_2 adsorbent and the catalyst particles.

Summarily, the catalytic performance of the NGZr catalyst was promoted by the introduction of MG50. The MG50 adsorbed CO_2 under the reaction condition, and thus the CO_2 concentration near Ni-Ga active sites was increased, contributing to an enhanced methanol formation rate. The scheme of CO_2 adsorption enhanced CO_2 hydrogenation to methanol was shown in Fig. 56. The MG50 can adsorb CO_2 due to its surface basicity or adsorption properties, and thus increase the CO_2 concentration around Ni-Ga-Zr catalysts, contributing to an enhanced CO_2 hydrogenation to produce methanol.

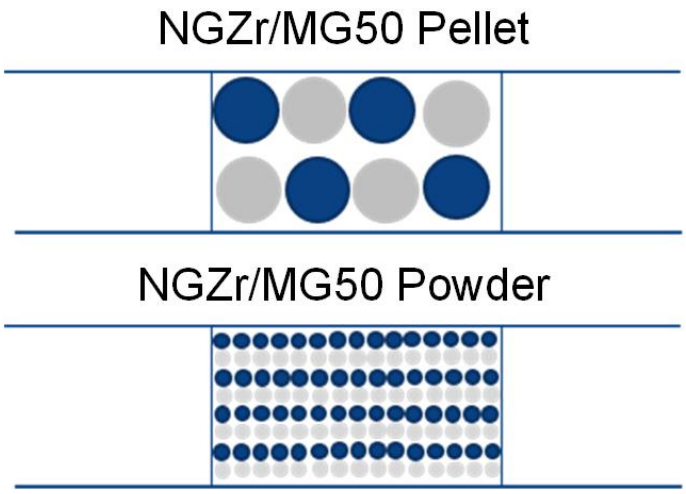

Fig. 54 Different packing mode for methanol synthesis reaction

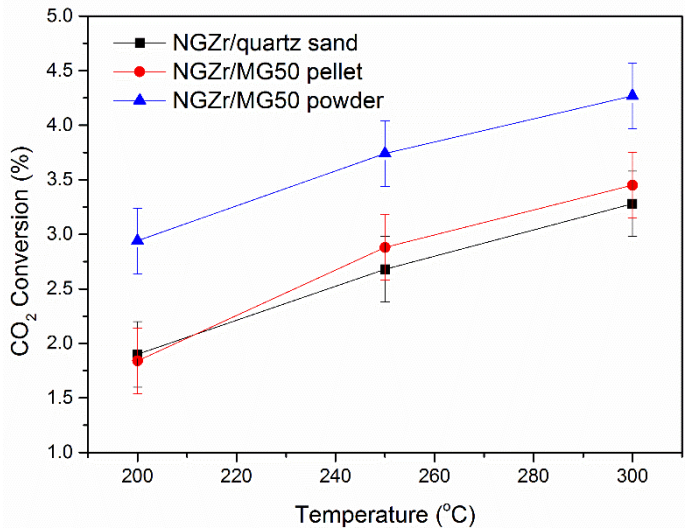

Fig. 55 CO_2 conversion of 25% NGZr/quartz sand, 25% NGZr/MG50 pellet and 25% NGZr/MG50 powder

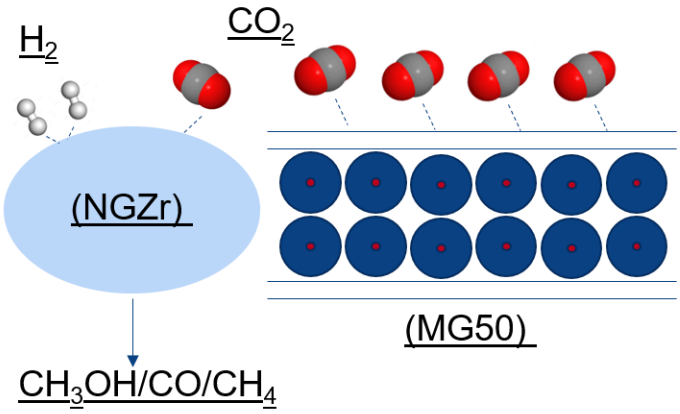

Fig. 56 Scheme of CO_2 adsorption enhanced CO_2 hydrogenation to methanol via NGZr and MG50 hybrid catalyst

6.3.3 Conclusion

In this chapter, MG50 was introduced in the Ni-Ga-Zr catalyst system which was synthesized via a HTlc precursor method discussed in the last chapter. The MG50 was activated at 400 °C prior to use and was directly mixed with reduced NGZr catalyst. The as-prepared sample was characterized by PXRD patterns, which showed that Ni_3Ga was not influenced by the introduction of MG50. The reflections of MG50 in PXRD patterns exhibited three broad (hump-like) peaks, indicating an amorphous metal oxide structure, due to an irreversible structure change due to 400 °C activation. The morphologies were investigated by SEM, and the results indicated that the NGZr catalysts were well-mixed with MG50. The CO_2 reduction performance was subsequently studied on the mixed catalyst system. The CO_2 conversion was greatly enhanced, almost two times higher compared with NGZr mixed with quartz sand. The results showed that the catalytic properties were promoted by the introduction of 50% MG50 as a high-temperature CO_2 adsorbent. The MG50 amount in the catalytic system was investigated subsequently. The highest space-time yield was observed in the 25%NGZr/MG50 mixture, with 123.5 $g_{meth} \cdot g_{cat}^{-1} \cdot h^{-1}$ at 300 °C. This interesting result suggested that catalytic properties per active site were greatly improved by MG50. A lower space velocity was also found to increase overall CO_2 conversion due to a shorter interaction time between gaseous reactant and active sites, however, the methanol selectivity decreased simultaneously. In addition, the type of high-temperature adsorbent influenced overall catalytic properties. The NGZr/Ca-chabazite mixed catalyst exhibited a poor

catalytic performance, with almost half of the CO_2 conversion compared with NGZr/MG50 catalysts at 300 °C, 30 bar. The decreased CO_2 conversion was attributed to the partial structure decomposition of Ca-chabazite due to dealumination in presence of moisture, and a lower CO_2 adsorption amount due to a weakened Van-der-Waal force at high temperature. Furthermore, a short distance between NGZr active sites and MG50 was observed to greatly enhance the CO_2 conversion, and thus the powder mixture was suggested to be the most appropriate packing mode for NGZr catalysts and MG50 catalytic system in methanol synthesis from CO_2.

Chapter 7 The study on a novel Ni-Ga-Zr catalyst for CO_2 hydrogenation to methanol

7.1 Introduction

In previous chapters, a novel Ni-Ga-Zr catalyst was successfully synthesized, and the catalytic performance, such as CO_2 conversion, methanol yield and selectivity, was found to be comparable with commercial Cu-based catalysts, at 300 °C, 30 bar. In Chapter 6, a further modification was carried out, by physically mixing a commercialized high-temperature CO_2 adsorbent, MG50, with Ni-Ga-Zr catalyst. The space-time yield of methanol was greatly improved, and the CO_2 conversion of the mixed catalytic system was two times higher than that of the same amount of individual catalyst. However, more efforts could be directed to enhance the Ni-Ga-Zr catalysts, to further increase the overall CO_2 conversion.

In this study, the Zr amount was optimized in Ni-Ga-Zr catalyst, by preparing a series of Ni-Ga-Zr HTlc structures and further reducing them under H_2/Ar at 700 °C. The as-prepared Ni-Ga-Zr catalysts were investigated by PXRD and TEM-Mapping, to study the structural information, elemental analysis and morphology characterization. The reducibility of precursors was studied by TPR measurement. Thermal stability of reduced Ni-Ga-Zr catalysts was examined by TGA measurement. The catalytic properties were evaluated in a micro-reactor, for CO_2 hydrogenation to methanol reaction.

7.2 Methodologies

7.2.1 Catalyst preparation

A series of HTlc precursors consisting of nickel, gallium, zirconium was synthesized by a urea hydrothermal method. $Ni(NO_3)_2.6H_2O$ (Sigma Aldrich), $Ga(NO_3)_3.9H_2O$ (Changsha Easchem Co., Limited), and $ZrO(NO_3)_2.6H_2O$ (Sigma Aldrich) were dissolved in 100 ml distilled water. The urea was added into the solution with vigorous stirring. The chemicals were used without further purification. The well-mixed solution was transferred to a hydrothermal autoclave (Parr, model 4843), heated at 110 °C for 4 hours with a stirring speed of 127 rpm. The precipitate was naturally cooled down to room temperature, separated by centrifugation, and washed with de-ionized water for three to four times, and dried at 100 °C overnight.

The Ni:Ga:Zr molar ratio in the mixed solution was listed in Table 12, and the HTlc precursor was denoted by the Zr content, namely, NGZr10-HTlc, NGZr15-HTlc, NGZr20-HTlc and NGZr25-HTlc, and NGZr5 in Chapter 5 was used as reference material.

Table 12 Nickel, Gallium and Zirconium molar ratio in as-prepared HTlc precursor

	Nickel	Gallium	Zirconium
NGZr5-HTlc	61.75	33.25	5.00
NGZr10-HTlc	58.50	31.50	10.00
NGZr15-HTlc	55.25	29.75	15.00
NGZr20-HTlc	52.00	28.00	20.00
NGZr25-HTlc	48.75	26.25	25.00

The precursors were collected, crushed and sieved into 40-60 mesh particles, and reduced by 5% H_2/Ar mixed gas with a flowrate of 40 mL/min, kept under 700 °C for 6 hours. The corresponding reduced catalysts with different Zr content were denoted as NGZr(x)-r, where x represented the Zr content.

7.3 Results and discussion

7.3.1 Structural and morphology study on Ni-Ga-Zr catalysts

The PXRD patterns of NGZr-r catalysts are shown in Fig. 57. As can be seen from the figure, the typical reflections of planes in the Ni_3Ga crystal structure could be clearly observed, with 2θ values of 43.6°, 50.8° and 74.8°, representing (111), (200) and (220) planes[139]. The presence of these peaks suggested that the Ni-Ga bimetallic phase was not changed as the Zr content increased. However, clear reflections of ZrO_2 were observed in addition to Ni_3Ga in the cases of NGZr15-r, NGZr20-r and NGZr25-r, suggesting that ZrO_2 was increasingly crystallized with an increasing amount of Zr in the catalyst synthesis mixture. Additionally, the Ni_3Ga crystal structure was also influenced by a higher Zr content. For example, the (220) plane, originally located at 75°, shifted to a higher angle in NGZr15-r, NGZr20-r and NGZr25-r samples. The slight change was possibly ascribed to lattice distortion. In Bragg's law, $n\lambda=2d\sin(\theta)$, where λ represents the X-ray wavelength, d indicates the lattice distance of specific crystal planes, and θ is the reflection angles. When peaks shifted to a higher angle, the corresponding lattice distance was decreased**.** The

reason could be either crystal plane contracted due to micro stress, or the atom in the crystal structure was replaced by other elements with a different diameter[140]. As can be seen from Fig. 57, the (220) plane in Ni_3Ga structure shifted to a higher angle, while other planes hardly exhibited any change, indicating that the (220) plane possibly contracted as the peak intensities corresponding to ZrO_2 increased, with an increase in the amount of Zr added into the catalytic system.

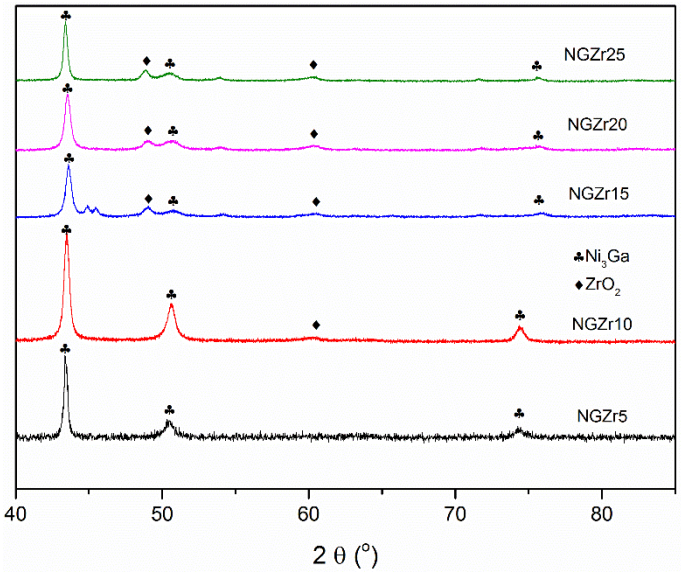

Fig. 57 PXRD patterns of as-prepared Ni-Ga-Zr catalysts

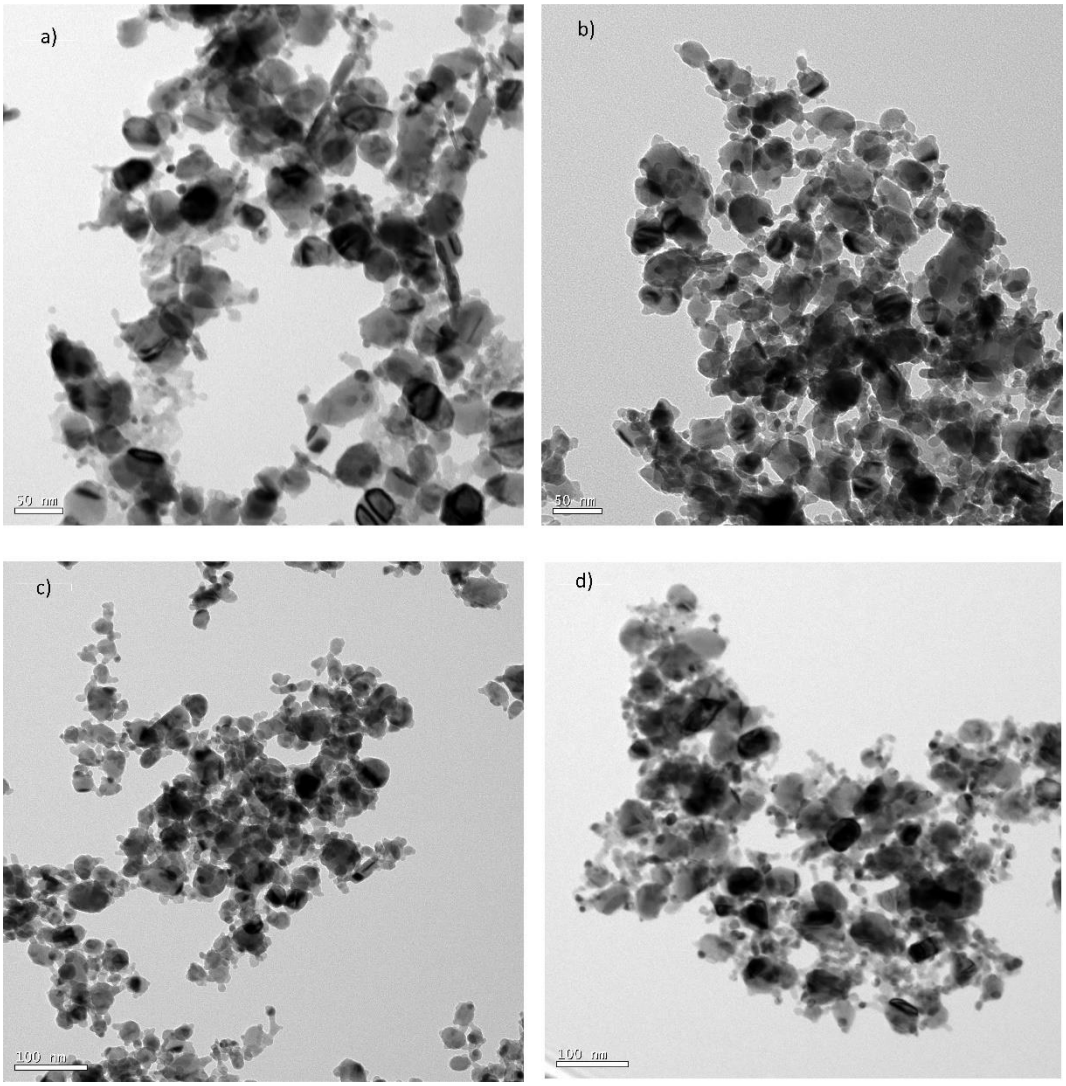

Fig. 58 TEM images of a) NGZr10-r, b) NGZr15-r, c) NGZr20-r and d) NGZr25-r

The morphologies of reduced Ni-Ga-Zr catalysts were investigated by TEM. As can be seen in Fig. 58, the average particle size of all reduced catalysts was quite similar, around 30-50 nm, and no obvious decrease was observed when compared with the NGZr5-r catalyst, as was discussed in Section 5.3.1.5. The elemental distribution of as-prepared Ni-Ga-Zr catalysts is shown in Fig. 59. Ni-Ga aggregated as a core while Zr was surrounded and isolated the agglomeration of Ni-Ga alloy as described earlier in chapter 5. However, as Zr content increased from 5% to 25%, the ZrO_2 no longer showed a spacer effect, instead, it formed ZrO_2 nanoclusters between Ni-Ga particles (Fig 59 b-d).

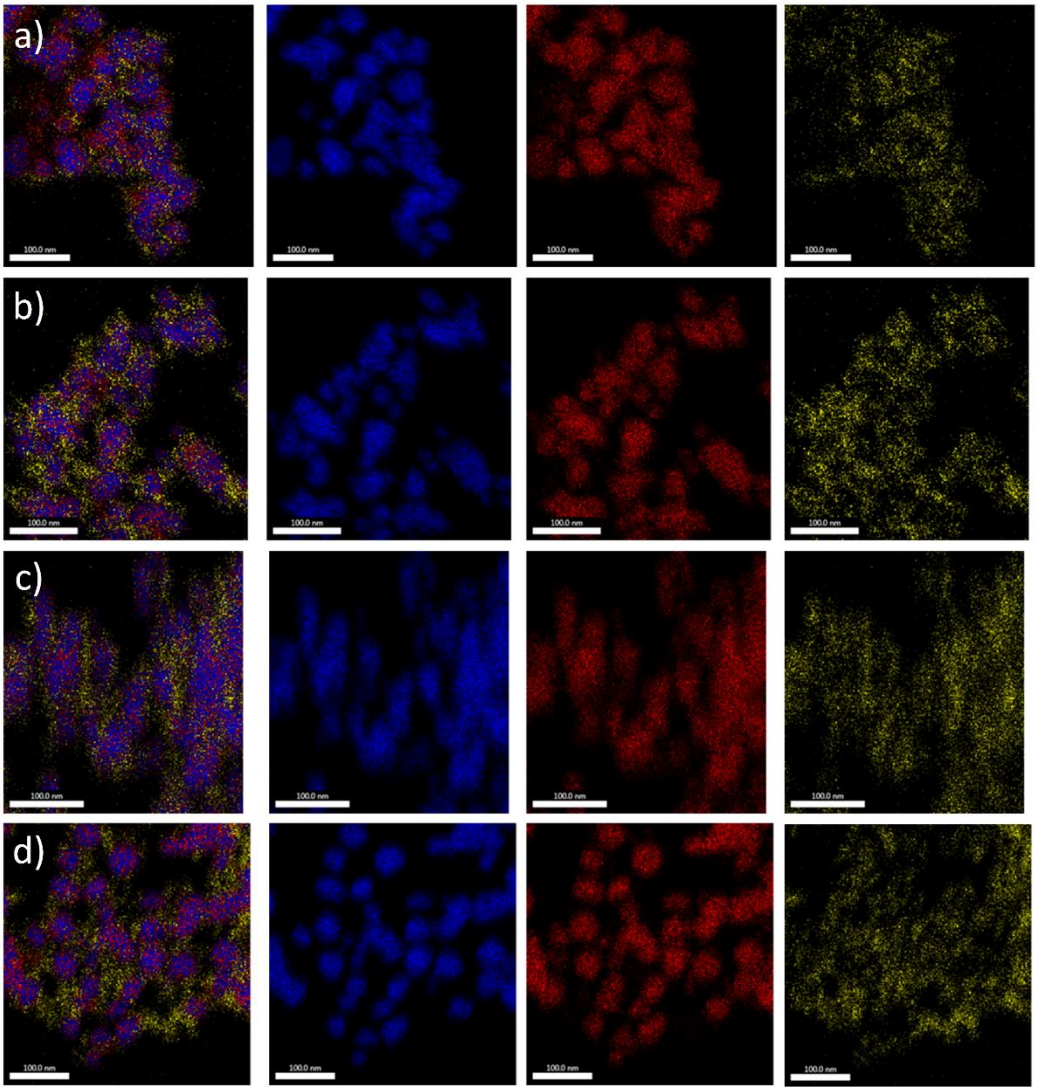

Fig. 59 TEM-mapping of a) NGZr10-r, b) NGZr15-r, c) NGZr20-r and d) NGZr25-r, where nickel atoms are blue, gallium atoms are red, and zirconium atoms are yellow

7.3.2 Reducibility of Ni-Ga-Zr catalysts

The reducibility of the as-prepared materials was investigated by TPR measurement. All samples were pre-treated at 300 °C under Helium atmosphere, to eliminate the influence of adsorbed H_2O and CO_2. As can be seen from Fig. 60, NGZr5 -HTlc showed difficulty during reduction (pretreatment), with all reduction peaks shifting to a higher temperature when compared with NGZr-HTlc investigated in Section 5.3.2. A similar result was reported in other literature[111] regarding the reduction of Ni-Ga nano-particles, and the change in reduction temperature was attributed to particle sintering at elevated calcination temperatures. When Zr content increased from 5% to 15%, the overall reduction peaks shifted to a lower

temperature since ZrO_2 facilitated electron transfer, and thus promoted the H_2 reduction. However, the reduction temperature was not further lowered as Zr content increased from 15% to 25%. The result suggested that ZrO_2 was saturated when Zr content reached 15%, and Ni-Ga alloy and ZrO_2 interaction with each other ceased when more Zr was introduced in HTlc framework. In addition, the Ni_1 disappeared in TPR profiles of NGZr15,20 and 25-HTlc samples. As discussed before, Ni_1 represented the reduction of isolated NiO in the HTlc precursor. An increasing amount of ZrO_2 in HTlc precursor contributed to more interactions between Ni-Zr, resulting in a sharp decrease amount of bulk NiO.

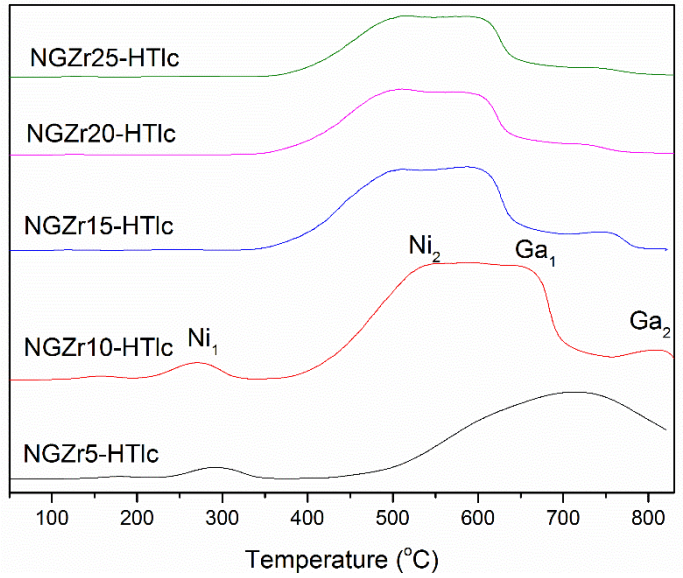

Fig. 60 TPR profiles for a series of Ni-Ga-Zr catalysts

7.3.3 Thermal stability of Ni-Ga-Zr catalysts

The NGZr15-r catalyst was investigated by TG measurement with a continuous CO_2 flow, to test the thermal and chemical stability of the as-prepared catalyst. As can be seen from Fig. 61, a mild weight loss was observed below 200 °C, which was due to the desorption of water, and the weight remained constant as temperature increased to 500 °C. However, an obvious weight increase was observed above 500 °C, suggesting that CO_2 was adsorbed on the catalyst's surface. The CO_2 subsequently reacted with ZrO_2 and formed carbonate species as temperature increased above 500 °C[141]. As a result, the catalysts were stable under 500 °C, and

it was chemically and thermally stable under reaction conditions studied, (200 °C-300 °C).

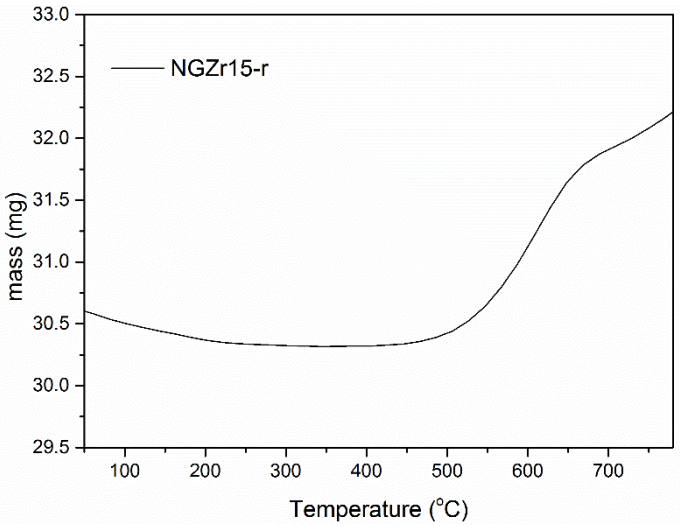

Fig. 61 TG profiles of NGZr15-r catalyst under CO_2 gas flow

7.3.4 Catalytic properties

The catalytic performance of as-prepared NGZrx-r catalysts and commercial Cu-based catalysts were evaluated for the methanol synthesis reaction in the temperature range between 200 °C and 300 °C, at 30 bar. As can be seen from Fig. 62, the CO_2 conversion exhibited an increasing trend as the Zr content increased to 15%, however, overall CO_2 conversion endured a slight decrease when Zr content was further increased from 15% to 25%. The interactions between Ni-Ga alloy and ZrO_2 were enhanced when Zr was incorporated into the framework with a moderate percentage (below 15%). Nevertheless, with an excess amount of Zr in the Ni-Ga catalytic system, no further promotion effect from ZrO_2 was observed, instead, the main Ni-Ga active sites for methanol synthesis decreased accordingly, resulting in a continuous loss in catalytic properties. It could also be found that the commercial Cu-based catalysts showed highest CO_2 conversion under all temperatures, but the methanol selectivity was the lowest as compared with Zr-modified Ni-Ga based catalysts (Fig. 63). The calculated methanol yield was reported in Fig. 64. The methanol yield of as-prepared NGZrx-r series exhibited a mild change at 200 °C when compared with its CO_2 conversion due to almost 100% methanol selectivity. In contrast, the methanol yield in the case of commercial Cu-based catalysts exhibited a sharp decrease because an enhanced rWGS reaction

competed with methanol synthesis simultaneously. As reaction temperature increased, the methanol yield experienced a slight change in NGZrx-r catalysts, and the highest methanol yield (3.42%) was observed in NGZr15-r at 300 °C and 30 bar. It was worth mentioning that the methanol yield from NGZr15-r surpassed that of commercial Cu-based catalysts over the entire temperature range.

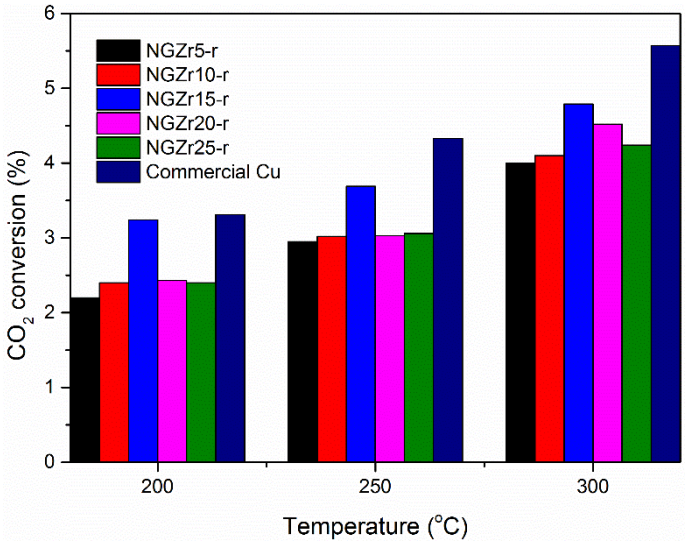

Fig. 62 CO_2 conversion of a series of NGZrx-r catalysts and Commercial Cu-based catalysts under the temperature range of 200 °C to 300 °C, 30 bar

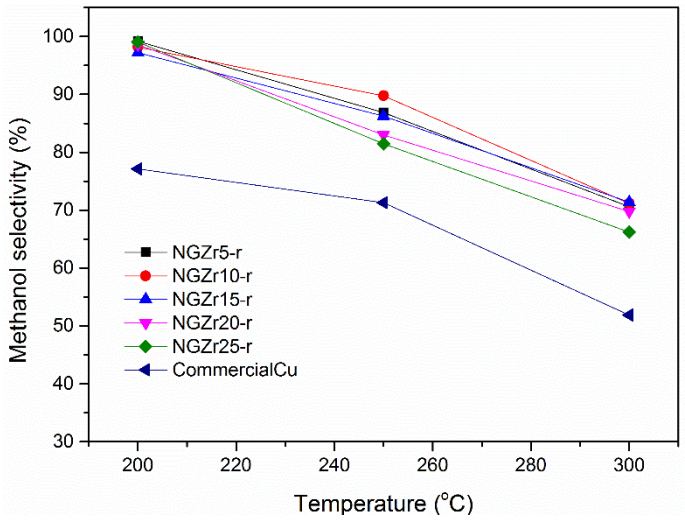

Fig. 63 Methanol selectivity of a series of NGZrx-r catalysts and Commercial Cu-based catalysts under the temperature range of 200 °C to 300 °C, 30 bar

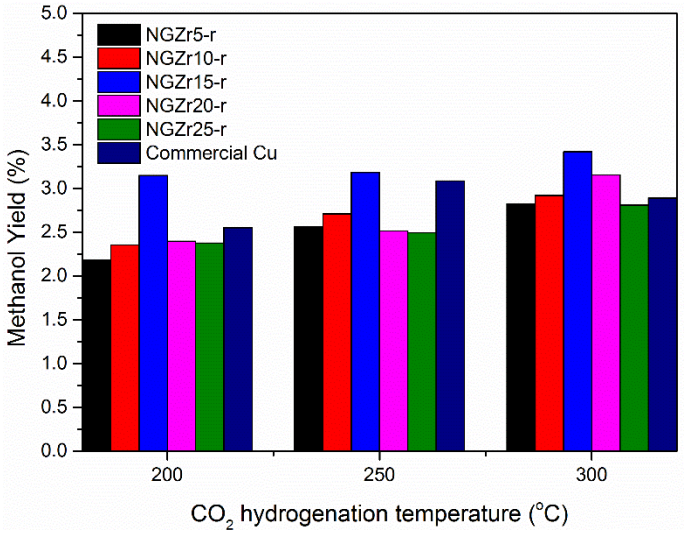

Fig. 64 Methanol yield of a series of NGZrx-r catalysts and Commercial Cu-based catalysts under the temperature range of 200 °C to 300 °C, 30 bar

7.4 Conclusion

In this chapter, a series of Ni-Ga-Zr catalysts were synthesized via HTlc precursors. The PXRD results suggested that Ni_3Ga was formed as a major Ni-Ga bimetallic phase. ZrO_2 peak intensity increased with an increase Zr content, from 15% to 25% Zr in the overall catalytic system, and an excess amount of Zr resulted in a contraction of (220) plane in Ni_3Ga crystal structure. The morphology information was obtained from TEM images, and it could be observed that the ZrO_2 agglomerated and formed nanoclusters between Ni-Ga particles, instead of surrounding it. The reducibility of the as-prepared parent HTlc precursors was tested by TPR. The reduction temperature of Ni-Ga-Zr catalysts shifted to lower temperature as Zr content increased to 15%, which was attributed to enhanced interaction between Ni-Ga and ZrO_2. However, no obvious improvement was observed as Zr content increased above 15%. The stability was investigated by TGA under a continuous CO_2 gas flow, and the result revealed that the Ni-Ga-Zr catalysts reacted with CO_2 and formed carbonates as the temperature was raised to over 500 °C, however, the catalysts were stable under reaction temperature range, which was between 200 °C and 300 °C. The catalytic performance was evaluated for methanol synthesis, and Ni-Ga-Zr catalyst with 15% Zr content exhibited the highest methanol yield, which was higher than commercial Cu-based catalyst over the entire reaction temperature range.

Chapter 8 Summary and future work

8.1 Summary

Even though the conclusion of each chapter has been reported before, a combined summary is shown here to illustrate the overall context of this research.

As discussed at the start of this thesis, a Ni_5Ga_3 bimetallic catalyst was reported by others to achieve high methanol selectivity and reasonable CO_2 conversion compared with other Ni-Ga bimetallic phases, such as NiGa and Ni_3Ga, and commercial Cu-based catalysts. However, that work showed that it was difficult to prepare highly pure Ni_5Ga_3, which limited the applicability of these catalysts. Therefore, a reproducible and relatively easier method to synthesize Ni_5Ga_3 was in great demand and provided the motivation for this PhD work.

At the beginning of this study, and reported in Chapter 4, a Ni-Ga type HTlc precursor was synthesized, to prepare highly pure Ni_5Ga_3 catalysts. The major findings were:

4-(1) The HTlc structure was greatly influenced by urea hydrothermal temperature. The HTlc particle size expanded in both horizontal [110] and vertical [003] directions as the temperature of urea hydrolysis increased from 90 °C to 150 °C.

4-(2) Ni_5Ga_3 crystal structure depended on its original parent HTlc precursor. An enlarged HTlc precursor grain size contributes to a larger Ni_5Ga_3 particle size, and a well-defined and more stable Ni-Ga HTlc precursor results in formation of a stable Ni_5Ga_3 structure with an expanded cell volume.

4-(3) HTlc precursor was highly selective for Ni_5Ga_3 synthesis. Ni_5Ga_3 could be easily obtained with a wide range of Ni:Ga ratio from HTlc precursor, while Ni_3Ga appeared to be the main phase as Ni:Ga ratio was varied in the traditional impregnation method.

4-(4) Sample 110 °C-Ni_5Ga_3 presented high methanol selectivity (100%) with an overall CO_2 conversion of 3.2%, and a turnover frequency of 0.27 s^{-1} in CO_2 hydrogenation to methanol. And the catalytic stability was confirmed by 160 hours endurance test with a constant CO_2 conversion.

Despite the high purity of Ni_5Ga_3, the catalytic performance could be further enhanced by reducing the particle size and increasing the promotion effect by metal oxides. Thus, additives, such as Mg, Zn and Zr, were incorporated in Ni-Ga HTlc precursor (Ni-Ga-X) using a similar synthesis procedure described in Chapter 5. The conclusions are summarized as below:

5-(1) Ni_3Ga, instead of Ni_5Ga_3, was the dominant Ni-Ga phase as promoters incorporated in parent HTlc structure. The instability of HTlc precursor due to additional elements and shortened hydrothermal reaction time contributed to the synthesis of Ni_3Ga.

5-(2) Each promoter presented as different forms in Ni-Ga catalytic system. Mg was not completely precipitated into Ni-Ga-Mg HTlc precursor due to a higher precipitation pH; $ZnGa_2O_4$ was formed in reduced Ni-Ga-Zn catalysts; while Zr presented as amorphous ZrO_2 in Zr modified Ni-Ga catalysts.

5-(3) ZrO_2 was crucial to prepare highly reactive Ni-Ga catalysts. Incorporating Zr in Ni-Ga catalysts considerably reduced the average particle sizes. The Ni_3Ga was isolated and separated by surrounding Zr as an apron in fringe. In addition, the ZrO_2 facilitated the reduction of Ni_3Ga catalysts with an enhanced electron transfer. Furthermore, a strong basic site was introduced to the overall catalytic matrix, which would facilitate the methanol synthesis.

5-(4) Ni-Ga-Zr (NGZr) catalyst exhibited the highest CO_2 conversion (4.6%) and methanol yield (3.8%). A stability test was carried out (TOS), and the CO_2 conversion remained constant for 100 hours' test.

The reactivity was enhanced by ZrO_2 as promoters in Ni_3Ga catalytic matrix. An idea was developed subsequently, based on the concept of "sorption enhanced reaction". Specifically, the NGZr catalyst was modified by a high-temperature CO_2 adsorbent in Chapter 6. Some conclusions were drawn as summarized below:

6-(1) The CO_2 conversion was almost two times higher over 50% MG50 mixed with 50% NGZr catalysts than 50% quartz sand mixed with 50% NGZr catalyst.

6-(2) The amount of MG50 greatly influenced the methanol space-time yield (STY_{MeOH}). The highest space-time yield was observed in 25%NGZr/MG50 mixture, with 123.5 $g_{meth}{\cdot}g_{cat}^{-1}{\cdot}h^{-1}$ at 300 °C.

6-(3) Other CO_2 adsorbent, such as Ca-chabazite, was found to be detrimental to the catalytic performance. The high-temperature dealumination of Ca-chabazite zeolite in the presence of water vapor and weakened Van der Vaal forces between zeolite and CO_2 at elevated temperatures, leading to a lower CO_2 conversion.

6-(4) The packing mode considerably influenced CO_2 conversion. The NGZr and MG50 were mixed in powder and pellet forms, respectively, and the former exhibited two times higher CO_2 promotion, while the later barely exhibited any promotion effect when compared with Cu-based catalysts. A short distance between active sites and CO_2 adsorbent was crucial for reactivity enhancement.

Despite the improvement in STY_{MeOH}, the methanol yield was still lower than commercial Cu-based catalysts under moderate temperature such as 200 °C and 250 °C. As a result, the Ni-Ga-Zr catalytic matrix was subsequently modified by optimizing the Zr content in Chapter 7. The conclusions are:

7-(1) t-ZrO_2 was highly crystallized with a higher Zr content (over 15%) and agglomerated as nanoclusters between Ni-Ga particles; while Zr tended to assemble around the Ni-Ga particles below Zr percentage (5%-15%), with higher interactions between Ni-Ga and ZrO_2.

7-(2) The average particle size was not further reduced as Zr content increased; however, the reducibility was enhanced at low Zr content (below 15%).

7-(3) The methanol yield of Ni-Ga-Zr(15%) surpassed that of Cu-based catalysts under the entire reaction condition.

8.2 Future work

In this study, Ni-Ga based catalysts were investigated in terms of structural information, theoretical analysis, and catalytic properties for the methanol synthesis reaction. Ni_5Ga_3 and Ni_3Ga are promising catalysts for methanol synthesis, specifically, Ni_3Ga has higher methanol yield compared with commercial Cu-based catalysts and Ni_5Ga_3 prepared from HTlc precursor. Despite improvement for the catalytic system, some studies remain to be further investigated in the future. These include:

(1) Decreasing particle size of Ni_5Ga_3 prepared from HTlc precursors: It can be seen from Chapter 4, that the lower CO_2 conversion was attributed to a large Ni_5Ga_3 grain size. The Ni_5Ga_3 particle agglomeration was due to high-temperature H_2 reduction. As a result, particle sizes of Ni_5Ga_3 could potentially be restricted by changing high-temperature reduction to lower temperature liquid reduction by alternate reducing agents. By this approach, Ni_5Ga_3 particles could possibly be well-separated in the liquid phase and avoid severe agglomeration.

(2) Investigation of other promoters for the Ni-Ga catalyst matrix: It was found that ZrO_2-decorated Ni-Ga catalysts exhibited a considerable increase in CO_2 conversion and methanol yield. As a result, other metal oxide promoters, such as Indium oxide and Titanium oxide, could possibly facilitate the methanol synthesis reaction rate.

(3) Further enhancement of Ni-Ga catalytic performance: The Ni-Ga-Zr (15%) catalyst was observed to exceed commercial Cu-based catalysts in terms of methanol yield and methanol selectivity, however, the price of Ni-Ga based catalysts surpassed that of Cu-based catalyst. As a result, further promoting the Ni-Ga-Zr catalytic system, by changing the preparation method, is in great demand to compensate the price margin for potential future industry application.

Bibliography

(1) Gielen, D.; Boshell, F.; Saygin, D.; Bazilian, M. D.; Wagner, N.; Gorini, R. The Role of Renewable Energy in the Global Energy Transformation. *Energy Strateg. Rev.* **2019**, *24* (January), 38–50.

(2) Chen, K.; Fang, H.; Wu, S.; Liu, X.; Zheng, J.; Zhou, S.; Duan, X.; Zhuang, Y.; Chi Edman Tsang, S.; Yuan, Y. CO2 Hydrogenation to Methanol over Cu Catalysts Supported on La-Modified SBA-15: The Crucial Role of Cu–LaOx Interfaces. *Appl. Catal. B Environ.* **2019**, *251* (March), 119–129.

(3) Centi, G.; Perathoner, S. Opportunities and Prospects in the Chemical Recycling of Carbon Dioxide to Fuels. *Catal. Today* **2009**, *148* (3–4), 191–205.

(4) Álvarez, A.; Bansode, A.; Urakawa, A.; Bavykina, A. V.; Wezendonk, T. A.; Makkee, M.; Gascon, J.; Kapteijn, F. Challenges in the Greener Production of Formates/Formic Acid, Methanol, and DME by Heterogeneously Catalyzed CO2 Hydrogenation Processes. *Chem. Rev.* **2017**, *117* (14), 9804–9838.

(5) Li, Y.; Zhang, Q.; Chai, R.; Zhao, G.; Liu, Y.; Lu, Y. Pyrolysis of Heavy Oil in the Presence of Supercritical Water: The Reaction Kinetics in Different Phases. *AICHE J.* **2015**, *61* (3), 857–866.

(6) Frontera, P.; Macario, A.; Ferraro, M.; Antonucci, P. L. Supported Catalysts for CO2 Methanation: A Review. *Catalysts* **2017**, *7* (2), 1–28.

(7) Daroughegi, R.; Meshkani, F.; Rezaei, M. Enhanced Activity of CO2 Methanation over Mesoporous Nanocrystalline Ni–Al2O3 Catalysts Prepared by Ultrasound-Assisted Co-Precipitation Method. *Int. J. Hydrogen Energy* **2017**, *42* (22), 15115–15125.

(8) Muroyama, H.; Tsuda, Y.; Asakoshi, T.; Masitah, H.; Okanishi, T.; Matsui, T.; Eguchi, K. Carbon Dioxide Methanation over Ni Catalysts Supported on Various Metal Oxides. *J. Catal.* **2016**, *343* (April), 178–184.

(9) Rahmani, S.; Rezaei, M.; Meshkani, F. Preparation of Highly Active Nickel Catalysts Supported on Mesoporous Nanocrystalline γ-Al2O3 for CO2 Methanation. *J. Ind. Eng. Chem.* **2014**, *20* (4), 1346–1352.

(10) Zhou, G.; Liu, H.; Xing, Y.; Xu, S.; Xie, H.; Xiong, K. CO2 Hydrogenation to Methane over Mesoporous Co/SiO2 Catalysts: Effect of Structure. *J. CO2 Util.* **2018**, *26* (March), 221–229.

(11) Zhou, G.; Wu, T.; Xie, H.; Zheng, X. Effects of Structure on the Carbon Dioxide Methanation Performance of Co-Based Catalysts. *Int. J. Hydrogen Energy* **2013**, *38* (24), 10012–10018.

(12) Wang, X.; Shi, H.; Kwak, J. H.; Szanyi, J. Mechanism of CO2 Hydrogenation on Pd/Al2O3 Catalysts: Kinetics and Transient DRIFTS-MS Studies. *ACS Catal.* **2015**, *5* (11), 6337–6349.

(13) Panagiotopoulou, P. Hydrogenation of CO2 over Supported Noble Metal Catalysts. *Appl. Catal. A Gen.* **2017**, *542* (March), 63–70.

(14) Wang, S.; Pan, Q.; Peng, J.; Wang, S. In Situ FTIR Spectroscopic Study of the CO2 Methanation Mechanism on Ni/Ce0.5Zr0.5O2. *Catal. Sci. Technol.* **2014**, *4* (2), 502–509.

(15) Preti, D.; Resta, C.; Squarcialupi, S.; Fachinetti, G. Carbon Dioxide Hydrogenation to Formic Acid by Using a Heterogeneous Gold Catalyst. *Angew. Chemie - Int. Ed.* **2011**, *50* (52), 12551–12554.

(16) Lv, X.; Lu, G.; Wang, Z. Q.; Xu, Z. N.; Guo, G. C. Computational Evidence for Lewis Base-Promoted CO2 Hydrogenation to Formic Acid on Gold Surfaces. *ACS Catal.* **2017**, *7* (7), 4519–4526.

(17) Tsai, J. C.; Nicholas, K. M. Rhodium-Catalyzed Hydrogenation of Carbon Dioxide to Formic Acid. *J. Am. Chem. Soc.* **1992**, *114* (13), 5117–5124.

(18) Rohr, M.; Günther, M.; Jutz, F.; Grunwaldt, J. D.; Emerich, H.; Beek, W. Van; Baiker, A. Evaluation of Strategies for the Immobilization of Bidentate Ruthenium-Phosphine Complexes Used for the Reductive Amination of Carbon Dioxide. *Appl. Catal. A Gen.* **2005**, *296* (2), 238–250.

(19) Jessop, P. G.; Hsiao, Y.; Ikariya, T.; Noyori, R. Homogeneous Catalysis in Supercritical Fluids: Hydrogenation of Supercritical Carbon Dioxide to Formic Acid, Alkyl Formates, and Formamides. *J. Am. Chem. Soc.* **1996**, *118* (2), 344–355.

(20) Dubois, J.-L.; Sayama, K.; Arakawa, H. Conversion of CO 2 to Dimethylether and Methanol over Hybrid Catalysts . *Chemistry Letters*. 1992, pp 1115–1118.

(21) Arakawa, H.; Dubois, J. L.; Sayama, K. Selective Conversion of CO2 to Methanol by Catalytic Hydrogenation over Promoted Copper Catalyst. *Energy Convers. Manag.* **1992**, *33* (5–8), 521–528.

(22) Jun, K. W.; Shen, W. J.; Rama Rao, K. S.; Lee, K. W. Residual Sodium Effect on the Catalytic Activity of Cu/ZnO/Al2O3 in Methanol Synthesis from CO2 Hydrogenation. *Appl. Catal. A Gen.* **1998**, *174* (1–2), 231–238.

(23) Ma, Y.; Sun, Q.; Wu, D.; Fan, W. H.; Zhang, Y. L.; Deng, J. F. A Practical Approach for the Preparation of High Activity Cu/ZnO/ZrO2 Catalyst for Methanol Synthesis from CO2 Hydrogenation. *Appl. Catal. A Gen.* **1998**, *171* (1), 45–55.

(24) Ma, Y.; Sun, Q.; Wu, D.; Fan, W. H.; Deng, J. F. A Gel-Oxalate Co-Precipitation Process for Preparation of Cu/ZnO/Al2O3 Ultrafine Catalyst for Methanol Synthesis from CO2+H2: (II) Effect of Various Calcination Conditions. *Appl. Catal. A Gen.* **1999**, *177* (2), 177–184.

(25) Guo, X.; Mao, D.; Lu, G.; Wang, S.; Wu, G. CO2 Hydrogenation to Methanol over Cu/ZnO/ZrO2 Catalysts Prepared via a Route of Solid-State Reaction. *Catal. Commun.* **2011**, *12* (12), 1095–1098.

(26) Zhuang, H. D.; Bai, S. F.; Liu, X. M.; Yan, Z. F. Structure and Performance of Cu/ZrO2 Catalyst for the Synthesis of Methanol from CO2 Hydrogenation. *Ranliao Huaxue Xuebao/Journal Fuel Chem. Technol.* **2010**, *38* (4), 462–467.

(27) Lei, H.; Hou, Z.; Xie, J. Hydrogenation of CO2 to CH3OH over CuO/ZnO/Al2O3 Catalysts Prepared via a Solvent-Free Routine. *Fuel* **2016**, *164*, 191–198.

(28) Guo, X.; Mao, D.; Lu, G.; Wang, S.; Wu, G. Glycine-Nitrate Combustion Synthesis of CuO-ZnO-ZrO2 Catalysts for Methanol Synthesis from CO2 Hydrogenation. *J. Catal.* **2010**, *271* (2), 178–185.

(29) Behrens, M.; Kasatkin, I.; Kühl, S.; Weinberg, G. Phase-Pure Cu,Zn,Al Hydrotalcite-like Materials as Precursors for Copper Rich Cu/ZnO/Al2O3 Catalysts. *Chem. Mater.* **2010**, *22* (2), 386–397.

(30) Gao, P.; Li, F.; Zhan, H.; Zhao, N.; Xiao, F.; Wei, W.; Zhong, L.; Wang, H.; Sun, Y. Influence of Zr on the Performance of Cu/Zn/Al/Zr Catalysts via Hydrotalcite-like Precursors for CO2 Hydrogenation to Methanol. *J. Catal.* **2013**, *298*, 51–60.

(31) Xiao, S.; Zhang, Y.; Gao, P.; Zhong, L.; Li, X.; Zhang, Z.; Wang, H.; Wei, W.; Sun, Y. Highly Efficient Cu-Based Catalysts via Hydrotalcite-like Precursors for CO2 Hydrogenation to Methanol. *Catal. Today* **2017**, *281* (December), 327–336.

(32) Lee, J.; Farha, O. K.; Roberts, J.; Scheidt, K. A.; Nguyen, S. T.; Hupp, J. T. Metal-Organic Framework Materials as Catalysts. *Chem. Soc. Rev.* **2009**, *38* (5), 1450–1459.

(33) Rungtaweevoranit, B.; Baek, J.; Araujo, J. R.; Archanjo, B. S.; Choi, K. M.; Yaghi, O. M.; Somorjai, G. A. Copper Nanocrystals Encapsulated in Zr-Based Metal-Organic Frameworks for Highly Selective CO2 Hydrogenation to Methanol. *Nano Lett.* **2016**, *16* (12), 7645–7649.

(34) Zhao, F.; Fan, L.; Xu, K.; Hua, D.; Zhan, G.; Zhou, S. F. Hierarchical Sheet-like Cu/Zn/Al Nanocatalysts Derived from LDH/MOF Composites for CO2 Hydrogenation to Methanol. *J. CO2 Util.* **2019**, *33* (March), 222–232.

(35) Kung, H. H. Deactivation of Methanol Synthesis Catalysts - a Review. *Catal. Today* **1992**, *11* (4), 443–453.

(36) Twigg, M. V.; Spencer, M. S. Deactivation of Supported Copper Metal Catalysts for Hydrogenation Reactions. *Appl. Catal. A Gen.* **2001**, *212* (1–2), 161–174.

(37) Behrens, M.; Furche, A.; Kasatkin, I.; Trunschke, A.; Busser, W.; Muhler, M.; Kniep, B.; Fischer, R.; Schlögl, R. The Potential of Microstructural Optimization in Metal/Oxide Catalysts: Higher Intrinsic Activity of Copper by Partial Embedding of Copper Nanoparticles. *ChemCatChem* **2010**, *2* (7), 816–818.

(38) Liao, F.; Huang, Y.; Ge, J.; Zheng, W.; Tedsree, K.; Collier, P.; Hong, X.; Tsang, S. C. Morphology-Dependent Interactions of ZnO with Cu Nanoparticles at the Materials' Interface in Selective Hydrogenation of CO2 to CH 3OH. *Angew. Chemie - Int. Ed.* **2011**, *50* (9), 2162–2165.

(39) Martin, O.; Mondelli, C.; Cervellino, A.; Ferri, D.; Curulla-Ferré, D.; Pérez-Ramírez, J. Operando Synchrotron X-Ray Powder Diffraction and

Modulated-Excitation Infrared Spectroscopy Elucidate the CO2Promotion on a Commercial Methanol Synthesis Catalyst. *Angew. Chemie - Int. Ed.* **2016**, *55* (37), 11031–11036.

(40) Behrens, M.; Studt, F.; Kasatkin, I.; Kühl, S.; Hävecker, M.; Abild-Pedersen, F.; Zander, S.; Girgsdies, F.; Kurr, P.; Kniep, B. L.; et al. The Active Site of Methanol Synthesis over Cu/ZnO/Al2O 3 Industrial Catalysts. *Science (80-.).* **2012**, *336* (6083), 893–897.

(41) Grunwaldt, J. D.; Molenbroek, A. M.; Topsøe, N. Y.; Topsøe, H.; Clausen, B. S. In Situ Investigations of Structural Changes in Cu/ZnO Catalysts. *J. Catal.* **2000**, *194* (2), 452–460.

(42) Nakamura, J.; Fujitani, T.; Kuld, S.; Helveg, S.; Chorkendorff, I.; Sehested, J. Comment on “Active Sites for CO2 Hydrogenation to Methanol on Cu/ZnO Catalysts.” *Science (80-.).* **2017**, *357* (6354), 1296–1299.

(43) Kuld, S.; Thorhauge, M.; Falsig, H.; Elkjær, C. F.; Helveg, S.; Chorkendorff, I.; Sehested, J. Quantifying the Promotion of Cu Catalysts by ZnO for Methanol Synthesis. *Science (80-.).* **2016**, *352* (6288), 969–974.

(44) Palomino, R. M.; Ramírez, P. J.; Liu, Z.; Hamlyn, R.; Waluyo, I.; Mahapatra, M.; Orozco, I.; Hunt, A.; Simonovis, J. P.; Senanayake, S. D.; et al. Hydrogenation of CO2 on ZnO/Cu(100) and ZnO/Cu(111) Catalysts: Role of Copper Structure and Metal-Oxide Interface in Methanol Synthesis. *J. Phys. Chem. B* **2018**, *122* (2), 794–800.

(45) Schilke, T. C.; Fisher, I. A.; Bell, A. T. In Situ Infrared Study of Methanol Synthesis from CO2/H2 on Titania and Zirconia Promoted Cu/SiO2. *J. Catal.* **1999**, *184* (1), 144–156.

(46) Arena, F.; Barbera, K.; Italiano, G.; Bonura, G.; Spadaro, L.; Frusteri, F. Synthesis, Characterization and Activity Pattern of Cu-ZnO/ZrO2 Catalysts in the Hydrogenation of Carbon Dioxide to Methanol. *J. Catal.* **2007**, *249* (2), 185–194.

(47) Guo, X.; Mao, D.; Lu, G.; Wang, S.; Wu, G. The Influence of La Doping on the Catalytic Behavior of Cu/ZrO2 for Methanol Synthesis from CO2 Hydrogenation. *J. Mol. Catal. A Chem.* **2011**, *345* (1–2), 60–68.

(48) Rhodes, M. D.; Bell, A. T. The Effects of Zirconia Morphology on Methanol Synthesis from CO and H 2 over Cu/ZrO2 Catalysts: Part I. Steady-State Studies. *J. Catal.* **2005**, *233* (1), 198–209.

(49) Samson, K.; Sliwa, M.; Socha, R. P.; Góra-Marek, K.; Mucha, D.; Rutkowska-Zbik, D.; Paul, J. F.; Ruggiero-Mikoajczyk, M.; Grabowski, R.; Soczyński, J. Influence of ZrO2 Structure and Copper Electronic State on Activity of Cu/ZrO2 Catalysts in Methanol Synthesis from CO2. *ACS Catal.* **2014**, *4* (10), 3730–3741.

(50) Bonura, G.; Arena, F.; Mezzatesta, G.; Cannilla, C.; Spadaro, L.; Frusteri, F. Role of the Ceria Promoter and Carrier on the Functionality of Cu-Based Catalysts in the CO2-to-Methanol Hydrogenation Reaction. *Catal. Today* **2011**, *171* (1), 251–256.

(51) Senanayake, S. D.; Ramírez, P. J.; Waluyo, I.; Kundu, S.; Mudiyanselage, K.; Liu, Z.; Liu, Z.; Axnanda, S.; Stacchiola, D. J.; Evans, J.; et al. Hydrogenation of CO2 to Methanol on CeOx/Cu(111) and ZnO/Cu(111) Catalysts: Role of the Metal-Oxide Interface and Importance of Ce3+ Sites. *J. Phys. Chem. C* **2016**, *120* (3), 1778–1784.

(52) Graciani, J.; Mudiyanselage, K.; Xu, F.; Baber, A. E.; Evans, J.; Senanayake, S. D.; Stacchiola, D. J.; Liu, P.; Hrbek, J.; Fernández Sanz, J.; et al. Highly Active Copper-Ceria and Copper-Ceria-Titania Catalysts for Methanol Synthesis from CO2. *Science (80-.).* **2014**, *345* (6196), 546–550.

(53) Ouyang, B.; Tan, W.; Liu, B. Morphology Effect of Nanostructure Ceria on the Cu/CeO2 Catalysts for Synthesis of Methanol from CO2 Hydrogenation. *Catal. Commun.* **2017**, *95*, 36–39.

(54) Fujitani, T. Methanol Synthesis from CO2 and H2 over Cu/ZnO/Ga2O3 Catalyst. *Chem. Lett.* **1993**, 1079–1080.

(55) Sanguineti, P. B.; Baltanás, M. A.; Bonivardi, A. L. Copper-Gallia Interaction in Cu-Ga2O3-ZrO2 Catalysts for Methanol Production from Carbon Oxide(s) Hydrogenation. *Appl. Catal. A Gen.* **2015**, *504*, 476–481.

(56) Collins, S. E.; Baltanás, M. A.; Bonivardi, A. L. Infrared Spectroscopic Study of the Carbon Dioxide Adsorption on the Surface of Ga2O3 Polymorphs. *J. Phys. Chem. B* **2006**, *110* (11), 5498–5507.

(57) Wang, J.; Ji, G.; Liu, Y.; Gondal, M. A.; Chang, X. Cu2O/TiO2 Heterostructure Nanotube Arrays Prepared by an Electrodeposition Method Exhibiting Enhanced Photocatalytic Activity for CO2 Reduction to Methanol. *Catal. Commun.* **2014**, *46*, 17–21.

(58) Nomura, N. Titania Supported Copper Catalysts for Methanol Synthesis from Carbon Dioxide. *React. Kinet. Catal. Lett.* **1998**, *63* (1), 9–13.

(59) Xiao, J.; Mao, D.; Guo, X.; Yu, J. Methanol Synthesis from CO2 Hydrogenation over CuO-ZnO-TiO2 Catalysts: The Influence of TiO2 Content. *Energy Technol.* **2015**, *3* (1), 32–39.

(60) Xiao, J.; Mao, D.; Guo, X.; Yu, J. Effect of TiO 2 , ZrO 2 , and TiO 2 -ZrO 2 on the Performance of CuO-ZnO Catalyst for CO 2 Hydrogenation to Methanol. *Appl. Surf. Sci.* **2015**, *338*, 146–153.

(61) Bando, K. K.; Sayama, K.; Kusama, H.; Okabe, K.; Arakawa, H. In-Situ FT-IR Study on CO2 Hydrogenation over Cu Catalysts Supported on SiO2, Al2O3, and TiO2. *Appl. Catal. A Gen.* **1997**, *165* (1–2), 391–409.

(62) Collins, S. E.; Chiavassa, D. L.; Bonivardi, A. L.; Baltanás, M. A. Hydrogen Spillover in Ga2O3-Pd/SiO2 Catalysts for Methanol Synthesis from CO2/H2. *Catal. Letters* **2005**, *103* (1–2), 83–88.

(63) Qu, J.; Zhou, X.; Xu, F.; Gong, X. Q.; Tsang, S. C. E. Shape Effect of Pd-Promoted Ga2O3 Nanocatalysts for Methanol Synthesis by CO2 Hydrogenation. *J. Phys. Chem. C* **2014**, *118* (42), 24452–24466.

(64) Song, J.; Liu, S.; Yang, C.; Wang, G.; Tian, H.; Zhao, Z. jian; Mu, R.; Gong, J. The Role of Al Doping in Pd/ZnO Catalyst for CO2 Hydrogenation to

Methanol. *Appl. Catal. B Environ.* **2020**, *263* (October 2019), 118367.

(65) Wu, D.; Deng, K.; Hu, B.; Lu, Q.; Liu, G.; Hong, X. Plasmon-Assisted Photothermal Catalysis of Low-Pressure CO 2 Hydrogenation to Methanol over Pd/ZnO Catalyst. *ChemCatChem* **2019**, *11* (6), 1598–1601.

(66) Rui, N.; Wang, Z.; Sun, K.; Ye, J.; Ge, Q.; Liu, C. jun. CO2 Hydrogenation to Methanol over Pd/In2O3: Effects of Pd and Oxygen Vacancy. *Appl. Catal. B Environ.* **2017**, *218*, 488–497.

(67) Wu, C.; Zhang, P.; Zhang, Z.; Zhang, L.; Yang, G.; Han, B. Efficient Hydrogenation of CO2 to Methanol over Supported Subnanometer Gold Catalysts at Low Temperature. *ChemCatChem* **2017**, *9* (19), 3691–3696.

(68) Yang, X.; Kattel, S.; Senanayake, S. D.; Boscoboinik, J. A.; Nie, X.; Graciani, J.; Rodriguez, J. A.; Liu, P.; Stacchiola, D. J.; Chen, J. G. Low Pressure CO2 Hydrogenation to Methanol over Gold Nanoparticles Activated on a CeOx/TiO2 Interface. *J. Am. Chem. Soc.* **2015**, *137* (32), 10104–10107.

(69) Studt, F.; Sharafutdinov, I.; Abild-Pedersen, F.; Elkjær, C. F.; Hummelshøj, J. S.; Dahl, S.; Chorkendorff, I.; Nørskov, J. K. Discovery of a Ni-Ga Catalyst for Carbon Dioxide Reduction to Methanol. *Nat. Chem.* **2014**, *6* (4), 320–324.

(70) Gallo, A.; Snider, J. L.; Sokaras, D.; Nordlund, D.; Kroll, T.; Ogasawara, H.; Kovarik, L.; Duyar, M. S.; Jaramillo, T. F. Ni5Ga3 Catalysts for CO2 Reduction to Methanol: Exploring the Role of Ga Surface Oxidation/Reduction on Catalytic Activity. *Appl. Catal. B Environ.* **2020**, *267* (February 2019), 118369.

(71) Ahmad, K.; Upadhyayula, S. Conversion of the Greenhouse Gas CO2 to Methanol over Supported Intermetallic Ga-Ni Catalysts at Atmospheric Pressure: Thermodynamic Modeling and Experimental Study. *Sustain. Energy Fuels* **2019**, *3* (9), 2509–2520.

(72) Chen, P.; Zhao, G.; Liu, Y.; Lu, Y. Monolithic Ni5Ga3/SiO2/Al2O3/Al-Fiber Catalyst for CO2 Hydrogenation to Methanol at Ambient Pressure. *Appl. Catal. A Gen.* **2018**, *562* (March), 234–240.

(73) Duyar, M. S.; Gallo, A.; Snider, J. L.; Jaramillo, T. F. Low-Pressure Methanol Synthesis from CO2 over Metal-Promoted Ni-Ga Intermetallic Catalysts. *J. CO2 Util.* **2020**, *39* (February), 101151.

(74) Jiang, X.; Koizumi, N.; Guo, X.; Song, C. Bimetallic Pd-Cu Catalysts for Selective CO2 Hydrogenation to Methanol. *Appl. Catal. B Environ.* **2015**, *170–171*, 173–185.

(75) Jiang, X.; Nie, X.; Wang, X.; Wang, H.; Koizumi, N.; Chen, Y.; Guo, X.; Song, C. Origin of Pd-Cu Bimetallic Effect for Synergetic Promotion of Methanol Formation from CO2 Hydrogenation. *J. Catal.* **2019**, *369*, 21–32.

(76) Liu, L.; Fan, F.; Jiang, Z.; Gao, X.; Wei, J.; Fang, T. Mechanistic Study of Pd-Cu Bimetallic Catalysts for Methanol Synthesis from CO2 Hydrogenation. *J. Phys. Chem. C* **2017**, *121* (47), 26287–26299.

(77) Snider, J. L.; Streibel, V.; Hubert, M. A.; Choksi, T. S.; Valle, E.; Upham, D. C.; Schumann, J.; Duyar, M. S.; Gallo, A.; Abild-Pedersen, F.; et al. Revealing the Synergy between Oxide and Alloy Phases on the Performance of Bimetallic In-Pd Catalysts for CO2 Hydrogenation to Methanol. *ACS Catal.* **2019**, *9* (4), 3399–3412.

(78) Ojelade, O. A.; Zaman, S. F.; Daous, M. A.; Al-Zahrani, A. A.; Malik, A. S.; Driss, H.; Shterk, G.; Gascon, J. Optimizing Pd:Zn Molar Ratio in PdZn/CeO2 for CO2 Hydrogenation to Methanol. *Appl. Catal. A Gen.* **2019**, *584* (July).

(79) Collins, S. E.; Delgado, J. J.; Mira, C.; Calvino, J. J.; Bernal, S.; Chiavassa, D. L.; Baltanás, M. A.; Bonivardi, A. L. The Role of Pd-Ga Bimetallic Particles in the Bifunctional Mechanism of Selective Methanol Synthesis via CO2 Hydrogenation on a Pd/Ga 2O3 Catalyst. *J. Catal.* **2012**, *292*, 90–98.

(80) Fiordaliso, E. M.; Sharafutdinov, I.; Carvalho, H. W. P.; Grunwaldt, J. D.; Hansen, T. W.; Chorkendorff, I.; Wagner, J. B.; Damsgaard, C. D. Intermetallic GaPd2 Nanoparticles on SiO2 for Low-Pressure CO2 Hydrogenation to Methanol: Catalytic Performance and in Situ Characterization. *ACS Catal.* **2015**, *5* (10), 5827–5836.

(81) García-Trenco, A.; Regoutz, A.; White, E. R.; Payne, D. J.; Shaffer, M. S. P.; Williams, C. K. PdIn Intermetallic Nanoparticles for the Hydrogenation of CO2 to Methanol. *Appl. Catal. B Environ.* **2018**, *220*, 9–18.

(82) Koh, M. K.; Khavarian, M.; Chai, S. P.; Mohamed, A. R. The Morphological Impact of Siliceous Porous Carriers on Copper-Catalysts for Selective Direct CO2 Hydrogenation to Methanol. *Int. J. Hydrogen Energy* **2018**, *43* (19), 9334–9342.

(83) Koizumi, N.; Jiang, X.; Kugai, J.; Song, C. Effects of Mesoporous Silica Supports and Alkaline Promoters on Activity of Pd Catalysts in CO 2 Hydrogenation for Methanol Synthesis. *Catal. Today* **2012**, *194* (1), 16–24.

(84) Wang, Z. Q.; Xu, Z. N.; Peng, S. Y.; Zhang, M. J.; Lu, G.; Chen, Q. S.; Chen, Y.; Guo, G. C. High-Performance and Long-Lived Cu/SiO2 Nanocatalyst for CO2 Hydrogenation. *ACS Catal.* **2015**, *5* (7), 4255–4259.

(85) Tasfy, S. F. H.; Zabidi, N. A. M.; Shaharun, M. S.; Subbarao, D. The Role of Support Morphology on the Performance of Cu/ZnO-Catalyst for Hydrogenation of CO 2 to Methanol. *AIP Conf. Proc.* **2015**, *1669* (July 2015).

(86) Sakata, Y.; Uddin, M. A.; Muto, A.; Imaoka, M. Carbon-Supported Well-Dispersed Cu-ZnO Catalysts Prepared from Sawdust Impregnated with [Cu(NO3)2, Zn(NO3)2] Solution: Catalytic Activity in CO2 Hydrogenation to Methanol. *Microporous Mater.* **1997**, *9* (3–4), 183–187.

(87) Liang, X. L.; Dong, X.; Lin, G. D.; Zhang, H. Bin. Carbon Nanotube-Supported Pd-ZnO Catalyst for Hydrogenation of CO2 to Methanol. *Appl. Catal. B Environ.* **2009**, *88* (3–4), 315–322.

(88) Dong, X.; Zhang, H.-B.; Lin, G.-D.; Yuan, Y.-Z.; Tsai, K. R. Highly Active CNT-Promoted Cu–ZnO–Al 2 O 3 Catalyst for Methanol Synthesis from H 2

/CO/CO 2. *Catal. Letters* **2003**, *85* (February).

(89) Zhang, Q.; Zuo, Y. Z.; Han, M. H.; Wang, J. F.; Jin, Y.; Wei, F. Long Carbon Nanotubes Intercrossed Cu/Zn/Al/Zr Catalyst for CO/CO2 Hydrogenation to Methanol/Dimethyl Ether. *Catal. Today* **2010**, *150* (1–2), 55–60.

(90) Sun, Y.; Chen, L.; Bao, Y.; Wang, G.; Zhang, Y.; Fu, M.; Wu, J.; Ye, D. Roles of Nitrogen Species on Nitrogen-Doped CNTs Supported Cu-ZrO2 System for Carbon Dioxide Hydrogenation to Methanol. *Catal. Today* **2018**, *307* (September 2016), 212–223.

(91) Deerattrakul, V.; Dittanet, P.; Sawangphruk, M.; Kongkachuichay, P. CO2 Hydrogenation to Methanol Using Cu-Zn Catalyst Supported on Reduced Graphene Oxide Nanosheets. *J. CO2 Util.* **2016**, *16*, 104–113.

(92) Witoon, T.; Numpilai, T.; Phongamwong, T.; Donphai, W.; Boonyuen, C.; Warakulwit, C.; Chareonpanich, M.; Limtrakul, J. Enhanced Activity, Selectivity and Stability of a CuO-ZnO-ZrO2 Catalyst by Adding Graphene Oxide for CO2 Hydrogenation to Methanol. *Chem. Eng. J.* **2018**, *334* (November 2017), 1781–1791.

(93) León, M.; Díaz, E.; Bennici, S.; Vega, A.; Ordóñez, S.; Auroux, A. Adsorption of CO2 on Hydrotalcite-Derived Mixed Oxides: Sorption Mechanisms and Consequences for Adsorption Irreversibility. *Ind. Eng. Chem. Res.* **2010**, *49* (8), 3663–3671.

(94) Fang, X.; Men, Y.; Wu, F.; Zhao, Q.; Singh, R.; Xiao, P.; Du, T.; Webley, P. A. Improved Methanol Yield and Selectivity from CO2 Hydrogenation Using a Novel Cu-ZnO-ZrO2 Catalyst Supported on Mg-Al Layered Double Hydroxide (LDH). *J. CO2 Util.* **2019**, *29* (November 2018), 57–64.

(95) Yang, Y.; White, M. G.; Liu, P. Theoretical Study of Methanol Synthesis from CO 2 Hydrogenation on Metal-Doped Cu(111) Surfaces. *J. Phys. Chem. C* **2012**, *116* (1), 248–256.

(96) Hong, Q. J.; Liu, Z. P. Mechanism of CO2 Hydrogenation over Cu/ZrO2(2$\bar{1}$2) Interface from First-Principles Kinetics Monte Carlo Simulations. *Surf. Sci.* **2010**, *604* (21–22), 1869–1876.

(97) Larmier, K.; Liao, W. C.; Tada, S.; Lam, E.; Verel, R.; Bansode, A.; Urakawa, A.; Comas-Vives, A.; Copéret, C. CO2-to-Methanol Hydrogenation on Zirconia-Supported Copper Nanoparticles: Reaction Intermediates and the Role of the Metal–Support Interface. *Angew. Chemie - Int. Ed.* **2017**, *56* (9), 2318–2323.

(98) Kourtelesis, M.; Kousi, K.; Kondarides, D. I. Co2 Hydrogenation to Methanol over LA2O3-Promoted CUO/ZNO/AL2O3 Catalysts: A Kinetic and Mechanistic Study. *Catalysts* **2020**, *10* (2).

(99) Atakan, A.; Erdtman, E.; Mäkie, P.; Ojamäe, L.; Odén, M. Time Evolution of the CO2 Hydrogenation to Fuels over Cu-Zr-SBA-15 Catalysts. *J. Catal.* **2018**, *362*, 55–64.

(100) Tang, Q.; Shen, Z.; Russell, C. K.; Fan, M. Thermodynamic and Kinetic Study on Carbon Dioxide Hydrogenation to Methanol over a Ga3Ni5(111)

Surface: The Effects of Step Edge. *J. Phys. Chem. C* **2018**, *122* (1), 315–330.

(101) Tang, Q.; Shen, Z.; Huang, L.; He, T.; Adidharma, H.; Russell, A. G.; Fan, M. Synthesis of Methanol from CO2 Hydrogenation Promoted by Dissociative Adsorption of Hydrogen on a Ga3Ni5(221) Surface. *Phys. Chem. Chem. Phys.* **2017**, *19* (28), 18539–18555.

(102) Zhao, Y. F.; Yang, Y.; Mims, C.; Peden, C. H. F.; Li, J.; Mei, D. Insight into Methanol Synthesis from CO2 Hydrogenation on Cu(1 1 1): Complex Reaction Network and the Effects of H2O. *J. Catal.* **2011**, *281* (2), 199–211.

(103) Tao, X.; Wang, J.; Li, Z.; Ye, Q. Theoretical Study on the Reaction Mechanism of CO2 Hydrogenation to Methanol. *Comput. Theor. Chem.* **2013**, *1023*, 59–64.

(104) Balzar, D. Voigt-Function Model in Diffraction Line-Broadening Analysis. *Microstruct. Anal. from Diffr.* **1999**, 44.

(105) Ravel, B.; Newville, M. ATHENA , ARTEMIS , HEPHAESTUS : Data Analysis for X-Ray Absorption Spectroscopy Using IFEFFIT B . Ravel and M . Newville ATHENA , ARTEMIS , HEPHAESTUS : Data Analysis for X-Ray Absorption Spectroscopy Using IFEFFIT. **2005**, 537–541.

(106) Galvão, T. L. P.; Neves, C. S.; Caetano, A. P. F.; Maia, F.; Mata, D.; Malheiro, E.; Ferreira, M. J.; Bastos, A. C.; Salak, A. N.; Gomes, J. R. B.; et al. Control of Crystallite and Particle Size in the Synthesis of Layered Double Hydroxides: Macromolecular Insights and a Complementary Modeling Tool. *J. Colloid Interface Sci.* **2016**, *468*, 86–94.

(107) Fahami, A.; Beall, G. W. Mechanosynthesis and Characterization of Hydrotalcite like Mg-Al-SO4-LDH. *Mater. Lett.* **2016**, *165*, 192–195.

(108) Adachi-Pagano, M.; Forano, C.; Besse, J.-P. Synthesis of Al-Rich Hydrotalcite-like Compounds by Using the Urea Hydrolysis Reaction?Control of Size and Morphology. *J. Mater. Chem.* **2003**, *13* (8), 1988.

(109) Kannan, S.; Narayanan, A.; Swamy, C. S. Effect of Composition on the Physicochemical Properties of Nickel Aluminium Hydrotalcites. *J. Mater. Sci.* **1996**, *31* (9), 2353–2360.

(110) Cheng, L. S.; Ralph T, Y. Improved Horvath-Kawazoe Equations Including Spherical Pore Models for Calculating Micropore Size Distribution. *Chem. Eng. Sci.* **1994**, *49* (16), 2599–2609.

(111) Sharafutdinov, I. Investigations into Low Pressure Methanol Synthesis . **2013**.

(112) Sharafutdinov, I.; Elkjær, C. F.; De Carvalho, H. W. P.; Gardini, D.; Chiarello, G. L.; Damsgaard, C. D.; Wagner, J. B.; Grunwaldt, J. D.; Dahl, S.; Chorkendorff, I. Intermetallic Compounds of Ni and Ga as Catalysts for the Synthesis of Methanol. *J. Catal.* **2014**, *320* (1), 77–88.

(113) Dalba, G.; Fornasini, P. EXAFS Debye - Waller Factor and Thermal Vibrations of Crystals. *J. Synchrotron Radiat.* **1997**, *4* (4), 243–255.

(114) Shen, W. J.; Ichihashi, Y.; Okumura, M.; Matsumura, Y. Methanol Synthesis from Carbon Monoxide and Hydrogen Catalyzed over Pd/CeCO2prepared by the Deposition-Precipitation Method. *Catal. Letters* **2000**, *64* (1), 23–25.

(115) Nitoslawski, S. A.; Galle, N. J.; Den, C. K. Van; Steenberg, J. W. N. Ni5Ga3 Catalysts for CO2 Reduction to Methanol: Exploring the Role of Ga Surface Oxidation/Reduction on Catalytic Activity. *Sustain. Cities Soc.* **2019**, 101770.

(116) Bonura, G.; Cordaro, M.; Cannilla, C.; Arena, F.; Frusteri, F. The Changing Nature of the Active Site of Cu-Zn-Zr Catalysts for the CO2 Hydrogenation Reaction to Methanol. *Appl. Catal. B Environ.* **2014**, *152–153*, 152–161.

(117) Zhang, L.; Chen, L.; Xia, S.; Wang, C.; Sun, F. Entropy Generation Minimization for Reverse Water Gas Shift (RWGS) Reactors. *Entropy* **2018**, *20* (6).

(118) Fornero, E. L.; Sanguineti, P. B.; Chiavassa, D. L.; Bonivardi, A. L.; Baltanás, M. A. Performance of Ternary Cu – Ga 2 O 3 – ZrO 2 Catalysts in the Synthesis of Methanol Using CO 2 -Rich Gas Mixtures. *Catal. Today* **2013**, *213*, 163–170.

(119) Witoon, T.; Chalorngtham, J.; Dumrongbunditkul, P.; Chareonpanich, M.; Limtrakul, J. CO2 Hydrogenation to Methanol over Cu/ZrO2 Catalysts: Effects of Zirconia Phases. *Chem. Eng. J.* **2016**, *293*, 327–336.

(120) Le Valant, A.; Comminges, C.; Tisseraud, C.; Canaff, C.; Pinard, L.; Pouilloux, Y. The Cu-ZnO Synergy in Methanol Synthesis from CO<inf>2</Inf>, Part 1: Origin of Active Site Explained by Experimental Studies and a Sphere Contact Quantification Model on Cu + ZnO Mechanical Mixtures. *J. Catal.* **2015**, *324*, 41–49.

(121) Cai, W.; De La Piscina, P. R.; Toyir, J.; Homs, N. CO<inf>2</Inf> Hydrogenation to Methanol over CuZnGa Catalysts Prepared Using Microwave-Assisted Methods. *Catal. Today* **2015**, *242* (Part A), 193–199.

(122) Wang, J. B.; Lee, H. K.; Huang, T. J. Synergistic Catalysis of Carbon Dioxide Hydrogenation into Methanol by Yttria-Doped Ceria/γ-Alumina-Supported Copper Oxide Catalysts: Effect of Support and Dopant. *Catal. Letters* **2002**, *83* (1–2), 79–86.

(123) Zhan, H.; Li, F.; Gao, P.; Zhao, N.; Xiao, F.; Wei, W.; Zhong, L.; Sun, Y. Methanol Synthesis from CO2 Hydrogenation over La-M-Cu-Zn-O (M = Y, Ce, Mg, Zr) Catalysts Derived from Perovskite-Type Precursors. *J. Power Sources* **2014**, *251*, 113–121.

(124) Hu, M.; Yang, W.; Liu, S.; Zhu, W.; Li, Y.; Hu, B.; Chen, Z.; Shen, R.; Cheong, W. C.; Wang, Y.; et al. Topological Self-Template Directed Synthesis of Multi-Shelled Intermetallic Ni 3 Ga Hollow Microspheres for the Selective Hydrogenation of Alkyne. *Chem. Sci.* **2019**, *10* (2), 614–619.

(125) Semerjian, L.; Ayoub, G. M. High-PH – Magnesium Coagulation – Flocculation in Wastewater Treatment. **2003**, *7*, 389–403.

(126) Balintova, M.; Petrilakova, A. Study of PH Influence on Selective

Precipitation of Heavy Metals from Acid Mine Drainage. *Chem. Eng. Trans.* **2011**, *25* (January 2011), 345–350.

(127) Guo, G. Y.; Chen, Y. L.; Ying, W. J. Thermal, Spectroscopic and X-Ray Diffractional Analyses of Zirconium Hydroxides Precipitated at Low PH Values. *Mater. Chem. Phys.* **2004**, *84* (2–3), 308–314.

(128) Zheng, Y.; Zhao, N.; Chen, J. Enhanced Direct Deoxygenation of Anisole to Benzene on SiO 2 -Supported Ni-Ga Alloy and Intermetallic Compound. *Appl. Catal. B Environ.* **2019**, *250* (March), 280–291.

(129) Grabowska, H.; Mita, W.; Trawczyński, J.; Wrzyszcz, J.; Zawadzki, M. A Method for Obtaining Thymol by Gas Phase Catalytic Alkylation of M-Cresol over Zinc Aluminate Spinel. *Appl. Catal. A Gen.* **2001**, *220* (1–2), 207–213.

(130) Babu, N. S.; Lingaiah, N.; Pasha, N.; Kumar, J. V.; Prasad, P. S. S. Influence of Particle Size and Nature of Pd Species on the Hydrodechlorination of Chloroaromatics: Studies on Pd/TiO2 Catalysts in Chlorobenzene Conversion. *Catal. Today* **2009**, *141* (1–2), 120–124.

(131) Yan, S. C.; Ouyang, S. X.; Gao, J.; Yang, M.; Feng, J. Y.; Fan, X. X.; Wan, L. J.; Li, Z. S.; Ye, J. H.; Zhou, Y.; et al. A Room-Temperature Reactive-Template Route to Mesoporous Znga 2o4 with Improved Photocatalytic Activity in Reduction of Co2. *Angew. Chemie - Int. Ed.* **2010**, *49* (36), 6400–6404.

(132) Yang, Y.; Evans, J.; Rodriguez, J. A.; White, M. G.; Liu, P. Fundamental Studies of Methanol Synthesis from CO2 Hydrogenation on Cu(111), Cu Clusters, and Cu/ZnO(0001). *Phys. Chem. Chem. Phys.* **2010**, *12* (33), 9909–9917.

(133) Material, S. O.; York, N.; Nw, A. No Title. **2014**, *546*.

(134) Santiago-Rodríguez, Y.; Barreto-Rodríguez, E.; Curet-Arana, M. C. Quantum Mechanical Study of CO2 and CO Hydrogenation on Cu(111) Surfaces Doped with Ga, Mg, and Ti. *J. Mol. Catal. A Chem.* **2016**, *423*, 319–332.

(135) Zhang, M.; Dou, M.; Yu, Y. Theoretical Study of the Promotional Effect of ZrO 2 on In 2 O 3 Catalyzed Methanol Synthesis from CO 2 Hydrogenation. *Appl. Surf. Sci.* **2018**, *433*, 780–789.

(136) Gao, P.; Li, F.; Zhao, N.; Xiao, F.; Wei, W.; Zhong, L.; Sun, Y. Influence of Modifier (Mn, La, Ce, Zr and Y) on the Performance of Cu/Zn/Al Catalysts via Hydrotalcite-like Precursors for CO2hydrogenation to Methanol. *Appl. Catal. A Gen.* **2013**, *468*, 442–452.

(137) Soares, J. L.; Moreira, R. F. P. M.; José, H. J.; Grande, C. A.; Rodrigues, A. E. Hydrotalcite Materials for Carbon Dioxide Adsorption at High Temperatures: Characterization and Diffusivity Measurements. *Sep. Sci. Technol.* **2004**, *39* (9), 1989–2010.

(138) Silaghi, M. C.; Chizallet, C.; Raybaud, P. Challenges on Molecular Aspects of Dealumination and Desilication of Zeolites. *Microporous Mesoporous Mater.* **2014**, *191*, 82–96.

(139) Hu, M.; Yang, W.; Liu, S.; Zhu, W.; Li, Y.; Hu, B.; Chen, Z.; Shen, R.; Cheong, W. C.; Wang, Y.; et al. Topological Self-Template Directed Synthesis of Multi-Shelled Intermetallic Ni3Ga Hollow Microspheres for the Selective Hydrogenation of Alkyne. *Chem. Sci.* **2019**, *10* (2), 614–619.

(140) Bennis, M.; Heuson, E.; Roussel, P.; Dumeignil, F.; Paul, S. Characterization of Heterogeneous Catalysts By. **2018**, *41*, 40912–40920.

(141) Pokrovski, K.; Jung, K. T.; Bell, A. T. Investigation of CO and CO2 Adsorption on Tetragonal and Monoclinic Zirconia. *Langmuir* **2001**, *17* (14), 4297–4303.

List of Abbreviations

BET	Brunauer-Emmett-Teller
DFT	Density-Functional Theory
EXAFS	Extended X-ray Absorption Fine Structure
HIM	Helium Ion Microscopy
HRTEM	High Resolution Transmission Electron Microscopy
HTlc	Hydrotalcite-like compounds
ICP	Inductively Coupled Plasma
PXRD	Powder X-ray Diffraction
rWGS	Reverse Water Gas Shift
SEM	Scanning Electron Microscopy
TGA	Thermogravimetric Analysis
TPD	Temperature-programmed Desorption
TPR	Temperature-Programmed Reduction
XANES	X-ray Absorption Near Edge Structure
XAS	X-ray Absorption Spectroscopy
XPS	X-ray Photoelectron Spectroscopy